UC Berkeley

UC Berkeley Electronic Theses and Dissertations

Title

Pulsed Laser-induced Light Coupling and Phase Transformation of Silicon Nanostructures

Permalink

https://escholarship.org/uc/item/36f3b6nf

Author

Wang, Letian

Publication Date

2019

Peer reviewed|Thesis/dissertation

Pulsed Laser-induced Light Coupling and Phase Transformation of Silicon
Nanostructures

By

Letian Wang

A dissertation submitted in partial satisfaction of the

requirements for the degree of

Doctor of Philosophy

in

Engineering-Mechanical Engineering

in the

Graduate Division

of the

University of California, Berkeley

Committee in charge:

Professor Costas P. Grigoropoulos, Chair
Professor Chris Dames
Professor Jie Yao

Fall 2019

Abstract

Pulsed Laser-induced Light Coupling and Phase Transformation of Silicon
Nanostructures
by

Letian Wang

Doctor of Philosophy in Engineering-Mechanical Engineering

University of California, Berkeley

Professor Costas P. Grigoropoulos, Chair

Silicon nanostructures serve as the backbone of modern electronics and photonics. Particularly, silicon nanoresonator became an increasingly important building block for the advanced photonics applications, including sensing, wavefront engineering and integrated photonics. Its crystallinity engineering is critical for enabling the manufacturability as well as fueling the continuous innovation on the device functionalities. Meanwhile, the scalable patterning of such nanostructures could offer cost-effective and highly controllable manufacturing routes beyond the conventional complementary metal-oxide-semiconductor (CMOS) fabrication. Owing to the controllable energy delivery and capability to interact with nanostructures, pulsed laser processing could significantly shed light on the above challenges and opportunities.

The pulsed laser processing of semiconductor material has been intensely investigated in the last century providing insights into fundamental light-material interaction. In early this century, thin-film laser processing became the main research topic as the complex coupling of heat transfer and phase transformation has enabled the technical innovation towards thin-film transistors in the display industry. However, when the lateral dimensions of the semiconductor material further shrunk down to the order of 100nm, the governing laws of the multiphysics interaction had to incite a significant paradigm shift in the study of the optical coupling, heat transfer and phase transformations.

This dissertation focus on understanding new coupling mechanism of pulsed laser interaction with silicon nanostructures, and exploiting them for scalable patterning and crystal engineering of the functional resonator arrays. Based on the unique near-field enhanced optical absorption, we first demonstrate the optically directed assembly of silicon nanoresonators. Spherical silicon nanoresonators can be fabricated with programmable numbers and combinations. Based on the ultrafast quenching rate and high adhesion work of silicon, we then demonstrate the deformation-free reversible phase transformation of silicon resonators that enables the active modulation of visible wavelength metasurfaces. Our *in situ* reflection probing of a single silicon nanodisk coupled with comprehensive simulations helps to reveal the mechanism behind the amorphization. We believe the experimental probing results lends support to the hypotheses silicon relaxation time scale on the silicon glass transformation. Lastly,

1

through femtosecond laser irradiation, we observed the ultrafast field enhanced selective material removal within nanodisks. The detailed dynamics of the field enhancement, carrier excitation, non-thermal melting and subsequent cold ablation are studied *ex-situ* and *in-situ*. The mechanism can be used for scalable manufacturing of bowtie sensing structures and laser printing optical metasurfaces.

To my wife Shaoying Zhang, and our parents

Table of contents

List of figures

List of tables

List of acronyms

Acronym	Description
a-Si	Amorphous silicon
ADE	Alternative directional explicit
AIST	AgInSbTe compound
ANN	Artificial neural networks
c-Si	Crystalline silicon
CMOS	Complementary Metal Oxide Semiconductor (or its fabrication process)
CNT	Classical nucleation theories
dSFMT	double precision SIMD oriented Fast Mersenne Twister for Random Number Generation
EBL	Electron beam lithography
ED	Electric dipole
EM	Electromagnetic
FDM	Finite difference method
FDTD	Finite difference time domain
FEM	Finite element method
fs	Femtosecond
G	Gibbs free energy
GST	GeSbTe compound
HDL	High density liquid
I	Intensity
k	Imaginary part of complex refractive index
l-Si	Liquid silicon
LDA	Low density amorphous
LDL	Low density liquid
LiMA	Laser-induced modulated assembly
LPCVD	Low pressure chemical vapor deposition
MD	Magnetic dipole
MEMS	Micro-electro-mechanical-system
MQ	Magnetic quadrupole
n	Real part of complex refractive index
NAND	Not AND type of memory
ns	Nanosecond
NUV	Near ultraviolet
PCM	Phase change memory

P_{Het}	Probability of heterogeneous nucleation
P_{Hom}	Probability of homogeneous nucleation
PML	Perfect matched layer
ps	Picosecond
RCWA	Rigorous coupled wave analysis
RIE	Reactive ion etching
SHG	Second harmonic generation
SPR	Surface plasmon resonance
SRR	Split-ring resonator
TFSF	Total field scatter field
TFT	Thin film transistor

Acknowledgments

I have dedicated the dissertation to my wife for her company during my entire Ph.D. journey. We met just before I left Tsinghua for graduate study. For the past five years, she flew to the U.S. to visit me, then applied and studied at UCSD, later she worked at the bay area and finally said "Yes" to be my life-long companion. She attached her best five years with me and unconditionally supported my pursuit of a Ph.D.. Research can come across failures and frustrations, she is always the first one that I can express my feelings and also the first one that gives me the strength to fight back.

I cannot thank my parents enough as they shaped me into a confident, collaborative and capable person. My father taught me how to think logically and stay focused on learning. My mother taught me how to care about others and be collaborative. Due to the visa issue, we are separated for more than three years, yet their weekly check-in continues to deliver their trust on my path and their care on my health and happiness. Their unconditional support from childhood to my Ph.D. encourage me to pursue my goal steadily. Lastly, I want to pay a special tribute to my passed away grandfather, who is the first engineer in our family. He's become my role model through his entire life experience: he came from poor, changed his life by going to school, earned recognition as an outstanding telecommunication engineer. His non-attainable support on science education in my childhood nurtured my early interest in science and engineering, and finally led me into the path of pursuing a Ph.D. in Mechanical Engineering.

1 Introduction

1.1 Pulsed laser processing of nanostructures

The term "pulsed laser" refers to laser emitting pulses durations shorter than 1μs and consists of nanoseconds, picoseconds and femtoseconds. Pulsed laser processing offers a transient energy delivery with controllable power, duration and location. Based on the duration, it will have a configurable thermal effect on the material subject to irradiation. The unique features of pulsed laser have been exploited for the manufacturing of the Thin Film Transistor(TFT)[1] of displays. TFTs are fabricated on top of glasses, which requires the deposition of amorphous silicon and subsequent thermal processing to improve the crystallinity. Pulsed laser processing offers a unique advantage by providing fast heating and controlled crystallization with minimum thermal effect on the substrate.

With the development of the semiconductor industry and various nanotechnology, the semiconductor devices have now reached dimensions much smaller than wavelengths of light. Applying pulsed laser processing to semiconductor nanostructure could provide possibilities to engineer its geometry and the crystallinities. We will introduce below in details how it can be used for scalable manufacturing and active device control.

1.1.1 Semiconductor manufacturing and nanomanufacturing
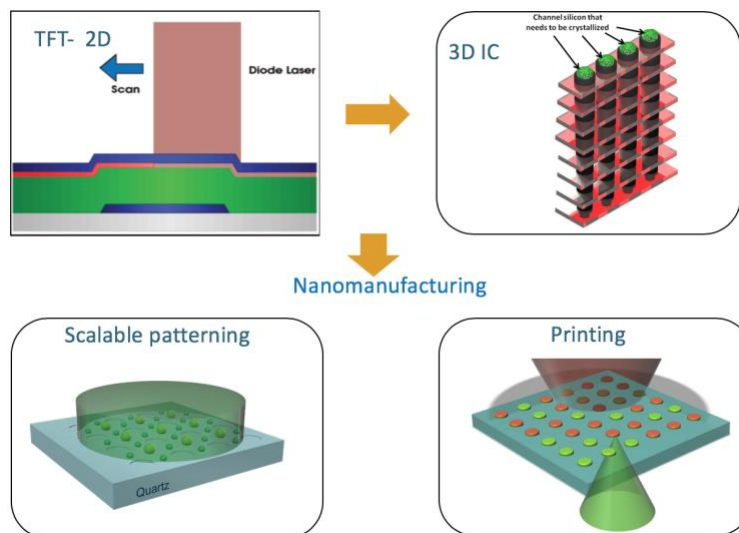
Figure 1.1 Pulsed laser processing for semiconductor manufacturing and nanomanufacturing

Pulsed laser processing can help solve the heterogeneous integration challenge in semiconductor manufacturing. With the development of cloud computing and artificial intelligence, the requirement of bringing logic and memory units closer becomes a pressing issue. Among various solutions, the development of 3D Integrated Circuits(IC)[2] has attracted great attention. A critical challenging for 3D IC integration is the stacking of high mobility crystalline Si/Ge layers on top of amorphous dielectric layers. Pulsed laser

1

crystallization shows the potential to improve the crystallinity of deposited amorphous material on oxide substrates, providing an alternative route for 3D IC integration. Recent progress has reported using pulsed laser annealing to improve the channel crystallinity in 3D NAND[3] Flash memory. Beyond improving crystallinity, it is further desired to bring laser recrystallization to its extreme capacity, generating single crystals from amorphous precursors.

Nanomanufacturing involves producing nanostructures in high precision and low cost. Surface patterned periodic nanostructures are important building blocks to novel electronics[4] and spintronics[5], chemical catalysts[6], plasmonic and photonic devices [7–9] as well as memory devices[10–12]. All of the above applications require fabricating arrays in high fidelity and low cost. Since high fidelity is usually associated with high-cost, e-beam lithography and spontaneous self-assembly represent two extremes. Pattern-guided laser[13–15] and thermal[16,17] dewetting, as well as liquid-assembly [18,19] can produce periodic metallic and dielectric nanostructures with a reasonable combination of fidelity and low cost. Due to its non-contact and scalable nature, laser light field patterning stands out as a promising and attractive option among various tuning methods.[20–22]

Besides high fidelity scalable patterning, recent advancements in structural color,[23–26] optical data storage[12,27,28] and active nanophotonic devices[29–31] highlight the need for customized fabrication and tuning of the nano building-blocks and their arrangement. With the high spatial resolution and controllable energy delivery, the transfer type printing of nanoresonators has been proposed[32]. Active and reversible tuning has also been reported[33] based on standing wave and optical tweezing. On-demand patterning of nanostructures on 2D patterns with nanometer tunability could revolutionize the production of customized devices, just like "3D printing" to the manufacturing.

1.1.2 Phase change devices

Phase change materials (PCM) present crystallinity dependent optical or electrical properties, which has been utilized for storage devices for a decade. A big group of phase change materials is GeSbTe(GST), part of the chalcogenide glasses family. The refractive index change of GST has been applied a decade ago in the optical storage systems including CD, DVD, and blue rays(Fig. 1.2A). Recent advancements in nanophotonics including metasurfaces and integrated photonics have vitalized the development of active modulation. Phase change materials like VO_2 provides volatile programmable photonic properties in IR [34]. For non-volatile applications, chalcogenide glasses, such as AgInSbTe(AIST) and GeSbTe (GST) have been commercially applied to optical storage and electronic memory. Due to their high spatial resolution[29], high speed[35] and switchable photonic properties in IR [36], advanced photonic applications are demonstrated, including optoelectronic display[37], active wavefront control[29,38], on-chip memory[39], and computation[40,41](Fig. 1.2B-D).
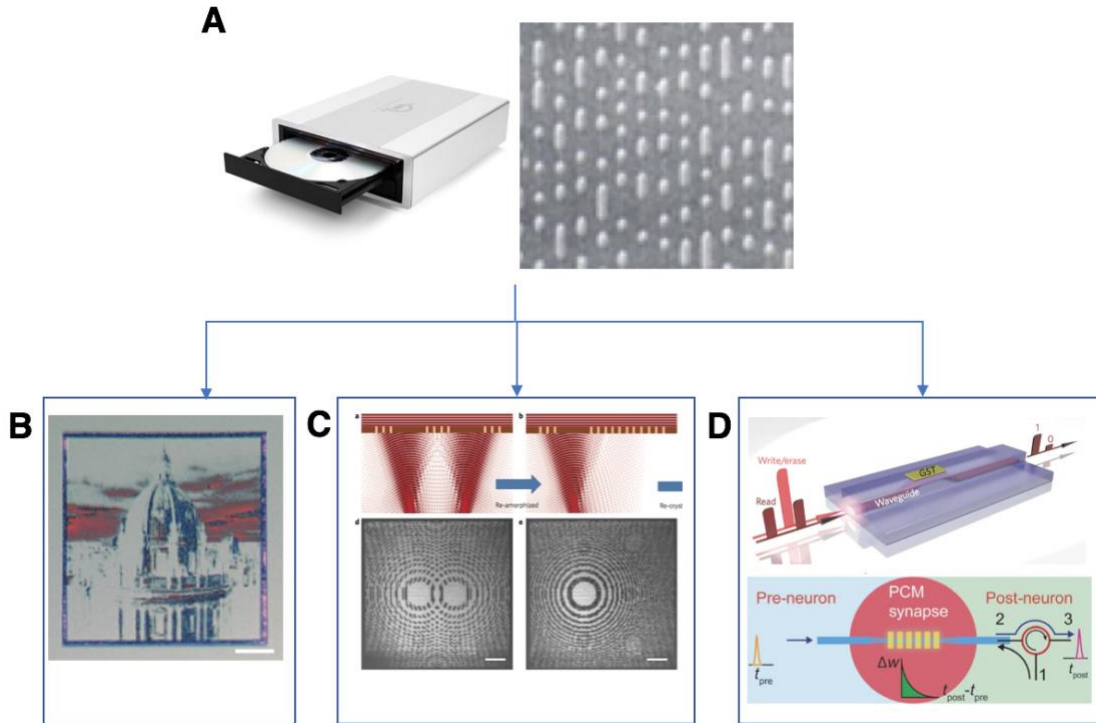
Figure 1.2 Phase change devices in photonic and electronic applications. (**A**) the optical rewritable storage. (**B**) The optoelectronic display based on thin-film GST[37]. (**C**) The optical wavefront control based on thin-film GST[29]. (**D**) The photonic memory and perceptron based on the integrated GST element[39,41].

However, many PCM elements (Ag, S, and V etc) are not allowed in the CMOS fab and even GST is only permitted in some pilot memory foundries[42,43], which limits the large scale manufacturing of active photonic devices. Furthermore, compound PCMs require maintaining stoichiometry throughout the whole domain for consistent properties which has been a big concern for memory industries[42]. Therefore monatomic phase change materials have been proposed [44]. Lastly, while many phase-change switching devices are demonstrated, PCMs incorporated in such devices are either in blanket film format or nanostructures capped with other materials. Film structure holds limited spatial precision and does not access the vast parameter space from geometry dependent nanoresonators. For device performance as well as fabrication cost, it will be worthy to develop reversible phase transformation on isolated geometries. However, such transformations on GST have been unsuccessful[45] and no demonstration on other materials has been reported either. The main obstacle is the melt-mediated deformation and dewetting of the structure, that prevents repeated operation. This issue becomes significant when the modulation is light-driven. Hence, obtaining a CMOS compatible, chemically stable and deformation free phase change material is of great value for expanding the current capabilities of the available PCMs.

Most importantly, while various phase change material have been demonstrated for application in IR[30], terahertz[46], microwave[47] and phononic systems[48], the territory of visible wavelength has not been explored fully. The main challenge is that the chalcogenide glass family presents a low refractive index and high loss in the visible

wavelength, especially for the crystalline phase[39]. Material innovation brought up Sb$_2$S$_3$[49] with higher refractive index and lower absorption in visible wavelengths, which is still considerable and hard to be CMOS compatible. Another proposal is to stack GST with silicon structure to create hybrid resonator[50], which is complex, costy and also vulnerable to chemical diffusion. It is therefore of great interest to explore the possible alternative phase change materials for the visible wavelengths.

1.2 Opportunities from pulsed laser processing on nanostructures

1.2.1 Pulse duration-dependent light-material interaction

Nanosecond pulsed laser processing of thin-film involves the coupling of heat transfer, phase transformation and even mass transport[51] effect. Such coupling has been widely studied in the laser annealing and dewetting of thin films. As they are all processes with time scale longer than 1ns, the details of carriers are not involved(Fig. 1.3), The same pulse-duration dependent multiphysics coupling can also be encountered and investigated for the nanosecond laser interaction with nanostructures.

When the laser pulse duration is shorter than the nanosecond, the transient dynamics of carrier excitation and relaxation will fall into the same time scale as the pulse duration (see Fig. 1.3). Therefore more complicated light material interaction becomes possible given when the laser pulse energy and pulse duration varies. The variation will ultimately result in different material processing effects. From this aspect, by utilizing a sub-nanosecond pulsed laser, we could explicitly explore and exploit the carrier dynamics effect on the nanoscale light-matter interaction. The details of the opportunities will be introduced in section 5.1.
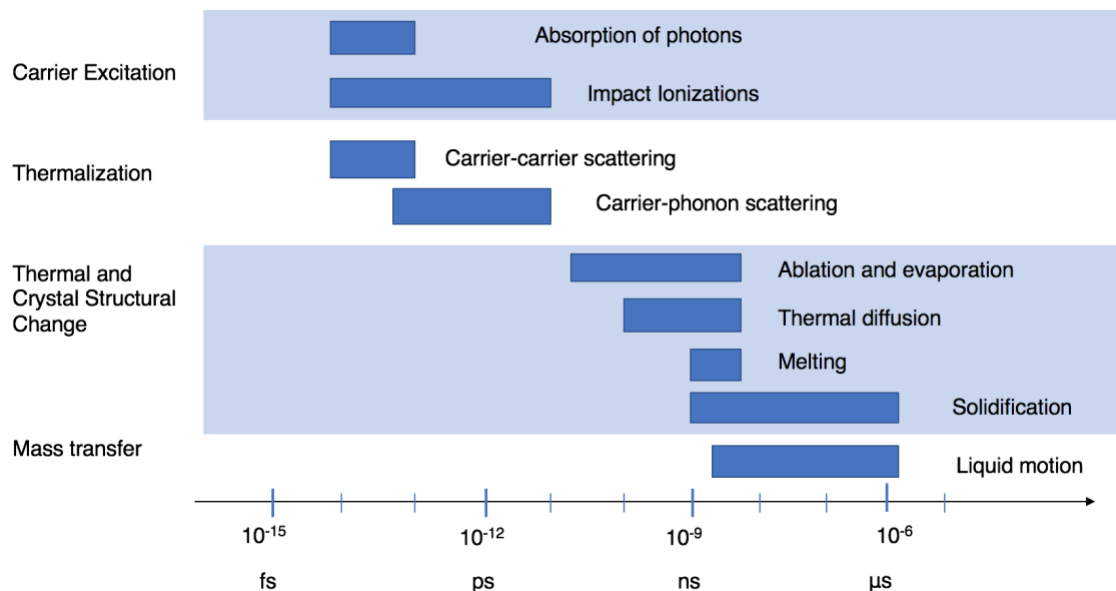
Figure 1.3 Timescales of various carrier and lattice interaction in laser-excited solids.

The figure is modified after the references[52,53] and a new time scale from ref[51] has been added.

1.2.2 Light interaction with silicon nanoresonators

Due to the well-studied properties and wide applications, both bulk and thin-film silicon has been intensively investigated with laser irradiation of femtosecond to nanoseconds. Sophisticated models have been developed to describe the carrier excitation, relaxation, thermal transport as well as structural transformation[54,55]. However, there are limited studies on the laser processing of nanostructures primarily due to the fabrication and probing challenges posed by the miniaturized sizes. Under the reduced dimension, several unique multiphysics coupling phenomena exist during laser processing. The process goes through optical field coupling, heat transfer, melting, interfacial effects and lastly solidification. Two main effects are listed below and the rest of the effects are described in section.2.1-2.3.

The optical properties of silicon nanostructures provide new effects in the light coupling and detectable optical characteristics during processing. Si features a high refractive index and relatively low loss in the visible wavelength, especially the near-ultraviolet (NUV) range[56]. As a result, Si nanostructures present strong electrical and magnetic multipolar Mie resonance[57] and various non-linear properties[58] within the visible frequencies. It provides strong resonance effects during pulsed laser coupling with the structure, which will subsequently affect the carrier excitation and thermal absorption. Furthermore, such resonances are geometry dependent, which provides drastically different optical signals upon geometry deformation. Lastly, its refractive indices offer good contrast between crystalline and amorphous phases, which also give distinct optical resonances in the nanoscale domain.

Compared to the thin film cases, the nanostructures dissipates heat more efficiently to its 3D surroundings rather than just the 1D vertical direction. Consequently, the fast quenching rate will lead to a phase transformation regime towards glass transition or more precisely, amorphization. Taking advantage of this trend, we may realize the reversible phase transformation of silicon nanodomain. On the other hand, since the dimension becomes smaller, it is then possible that only one or several nucleation events happen in the domain. Hence the stochastic nature of nucleation will be amplified compared to the conventional thin-film crystallization, thereby offering an experimental platform to study the pulse duration and laser energy's effect on the nucleation and subsequent crystallization.

Last but not least, silicon presents attractive features as a new phase change material for active photonics. High refractive indices, ease of fabrication and some nonlinear functionalities are the key advantages of silicon as the material for nanophotonics. Both crystalline and amorphous resonators have been used in many metasurfaces and integrated photonics devices[56,57,59,60]. Optical modulated crystallinity control may provide completely new opportunities for silicon-based nanophotonic devices[57]. For example, turning on and off edge states[61] and Fano resonances[62], modifying complex demultiplexer functions[63], and offering multilevel turnability to

hybrid metamaterials[50]. Furthermore, silicon can keep uniform chemical decomposition upon reversible optical modulation.

1.3 Structure of the dissertation

The dissertation focuses on exploring and understanding the phenomena of pulsed laser processing of silicon nanostructures in terms of optical coupling, phase transformation and geometry modifications, and apply them for manufacturing and active modulation of nanophotonics structures.

Chapter 1 provide the background and the motivation of this dissertation. In Chapter 2, it first describes the fundamentals of optical, thermal and phase transformation theories associated with the laser processing of nanostructures. Then the comprehensive simulation, experimental fabrication and characterization methods used in this dissertation are also introduced.

In Chapter 3, we will focus on the optical modulated nanoparticle assembly exploiting the near-field absorption and energy-dependent liquid instability to fabricate silicon nanoparticle arrays. Precise modulations of the fabricated nanoparticle array are demonstrated based on polarization, pulse energy and the number of pulses.

In Chapter 4, we establish the reversible crystallization and amorphization of silicon nanostructure and its application in active photonics. Through single nanostructure transient probing and the comprehensive simulation, we provide new knowledge of the mechanisms behind the phase transformations. We also discuss the dewetting suppression effect that enables the preservation of the photonic signatures. Lastly, we highlight its applications in the active photonics and provide a discussion on future works.

In Chapter 5, we show the results on the femtosecond pulsed laser-induced selective material removal within the nanoresonator. Preliminary explanations and on-going researches are discussed. Potential applications in enhanced fluorescence sensing and printable optical metasurfaces are presented.

2 Fundamental theories and experimental techniques

2.1 Optical theories

2.1.1 The complex refractive indices of silicon

The complex refractive index is the square root of the relative permittivity and permeability. Its real and imaginary parts are termed as refractive index n and extinction coefficient κ, respectively.

$$\underline{n} = \sqrt{\varepsilon_r \mu_r} \tag{2.1}$$
$$\underline{n} = n + ik \tag{2.2}$$

Most naturally occurring materials are non-magnetic at optical frequencies, which gives that μ_r is very close to 1, therefore n can be approximated to $\sqrt{\varepsilon_r}$. In this particular case, the complex relative permittivity ε_r, with real and imaginary parts ε_r and $\widetilde{\varepsilon_r}$, and the complex refractive index $\underline{n}$, with real and imaginary parts n and κ follow the relation:

$$\varepsilon_r = n^2 - k^2 \tag{2.3}$$
$$\widetilde{\varepsilon_r} = 2nk \tag{2.4}$$

The real part of the refractive index, n characterizes the refractive power of the medium. The optical extinction coefficient k defines the loss of electromagnetic (EM) field in the medium. They jointly affect the resonance effect mentioned in the next section.
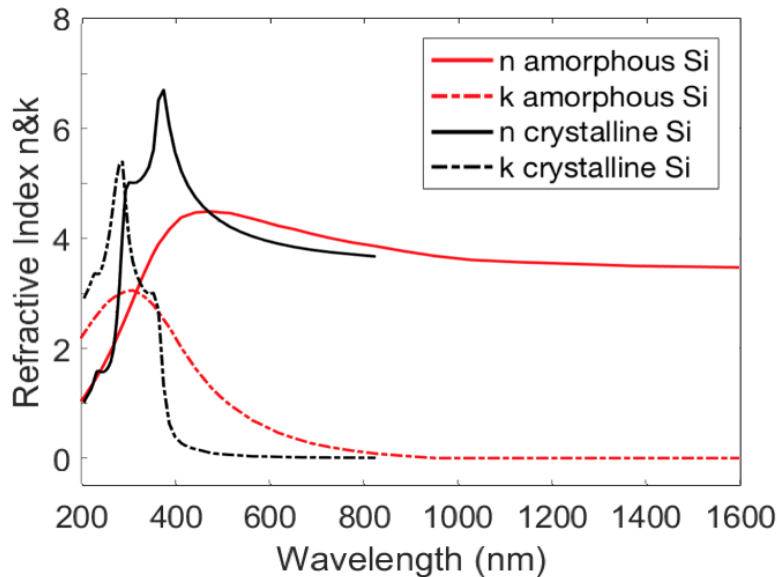
Figure 2.1 Complex Refractive Indexes for Crystalline and Amorphous Silicon

We plot in Fig. 2.1 the components of the complex refractive index of crystalline and amorphous silicon. The amorphous phase of silicon differs from the crystalline in the loss of the peak in the n at 400nm, and the increase of k in 400-600nm. Different from

crystalline silicon, amorphous silicon forms a continuous random network without long-range order. Furthermore, some atoms have a dangling bond due to the disordered nature. Physically, these dangling bonds represent defects in the continuous random network and add localized defect states in the band diagram, which is causing the difference in the complex refractive indices. As a consequence, the amorphous silicon's optical properties are found to be highly related to the processing conditions[64]. However, limited by the dimensionality of our nanoresonators, there are no direct methods to measure the refractive indexes. The refractive index applied in the simulation is from Low-Pressure Chemical Vapor Deposition(LPCVD), which is related to the deposition condition[65].

Silicon features a bandgap of 1.1 eV, therefore any light wavelength below 1.12um can be in principle absorbed. The analysis showed that the absorption at the bandgap edge shows a squared relation to the excess photon energy: $a=(hv-E_g)_2$, where v denotes the frequency [64] and E_g denotes the bandgap energy. While absorption losses become notable for shorter wavelengths, their increase is still moderate due to the indirect nature of the electronic bandgap[57]. Compared to mostly PCMs, silicon's absorption in visible range is still considerably small.

2.1.2 Optical resonance and silicon Mie resonators

Resonance describes the phenomena where amplification occurs when the frequency of a periodically applied force is in harmonic proportion to a natural frequency of the acted upon system[66]. When the optical field is reflected multiple times between two parallel mirrors(Fig. 2.2A), frequency-dependent optical enhancement is found(Fig. 2.2 B). Specifically, when light passing through two parallel semi-transparent mirrors, there will be multiple reflections at two mirror's surface. When the reflected optical field is in phase with the incoming optical field, constructive interference is formed. At resonance frequencies, the field amplitude inside an optical resonator reaches a maximum value due to the constructive interference. Similar to the thin film interferences, the optical field exiting the resonator, either reflection or transmission, will be greatly affected by the resonance frequency. The parallel mirror type of optical resonator is very common, which is called Fabry–Pérot interferometer, also an optical cavity[67]. In addition, there are also guided-mode resonance as well as the surface plasmon resonance(SPR).
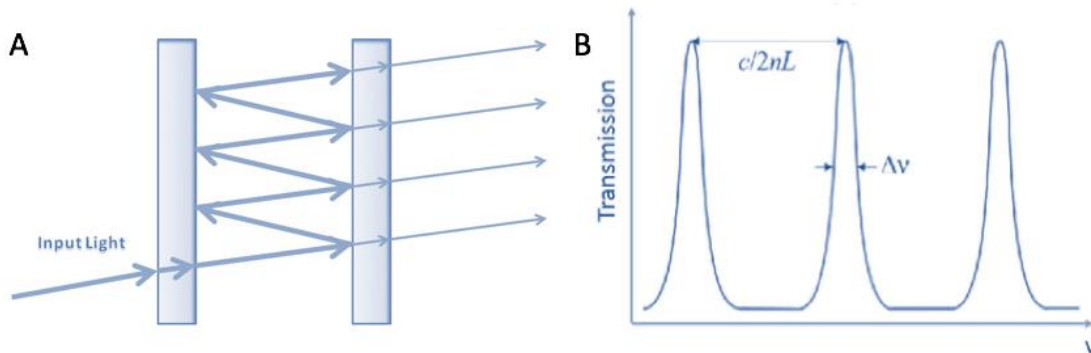
Figure 2.2 The working principle of Fabry–Pérot interferometer. (**A**) the schematics of two parallel mirrors and standing waves formed due to repeated reflection and

interference. (**B**) The resonance peaks of the transmission against different incident wavelengths.

High refractive index nanoparticles can effectively trap light and form cavities. One type of particular interest is Mie resonance, whose frequency-dependent resonance can be solved by the Mie scattering theories. Mie theories described the scattering effect of a plane wave on a homogeneous sphere based on the Mie solution to the Maxwell equation. The previous studies on Mie resonances emphasize on the scatters in the atmosphere, chemistry and biology.

The magnetic resonance in dielectric nanoparticles at visible wavelengths has triggered a research interest renaissance to dielectric resonators. The most common example of magnetic dipole radiation is an electromagnetic wave produced by an excited metal split-ring resonator (SRR). The possibility of obtaining magnetic responses in optical frequencies enables non-unity and even negative magnetic permeability. Related applications are in negative refraction, cloaking or superlensing[57]. The SRR principle fails to extend to visible wavelength due to the fabrication limitation as well as the intrinsic loss. Based on its high refractive index and low loss nature, silicon nanostructure effectively present magnetic resonance in the visible wavelength. In 2012, Kuznetsov *et al.*[68] carried out the first experimental demonstration of the magnetic dipole in silicon nanoparticles. Such magnetic resonance can be used as the building blocks of magnetic metamaterials. Remarkably, for the refractive indices above a certain value, there is a well-established hierarchy of magnetic and electric resonances[68].

Additionally, the surface plasmonic resonance(SPR) exists between metal and dielectric surface, which makes it best suited for sensing the interfacial property change including biological substances. The Mie resonance inside silicon is fully internal, thus leading to a significant internal field intensity and phase delay with low losses, which is not easily attainable from metallic counterparts. Such internal field concentration leads to magnified non-linear effects from silicon[69–71]. This overall concept drove the recent progress in the dielectric based photonics.

Based on the resonance effect, the optical field will present a space-variant electrical and magnetic field inside the nanostructure. Detailed simulation can be carried out in Finite Difference Time Domain(FDTD) and we provide a characteristic field plot for electric dipole and magnetic dipole resonances from a silicon nanoparticle on top of the silica substrate (Figure 2.3). The electric dipole(ED) and magnetic dipole(MD) are determined through the comparison of the field plots with those from standard dipole moments. The rigorous way of determining the multipolar resonance required the multipolar decomposition techniques mentioned in references[72]. Especially for the higher-order quadrupoles, the existence of anapole moments[73] in silicon resonators complicates the analysis.

	E field contour	E field vector	H field contour	H field vector
470nm ED				
590nm MD				
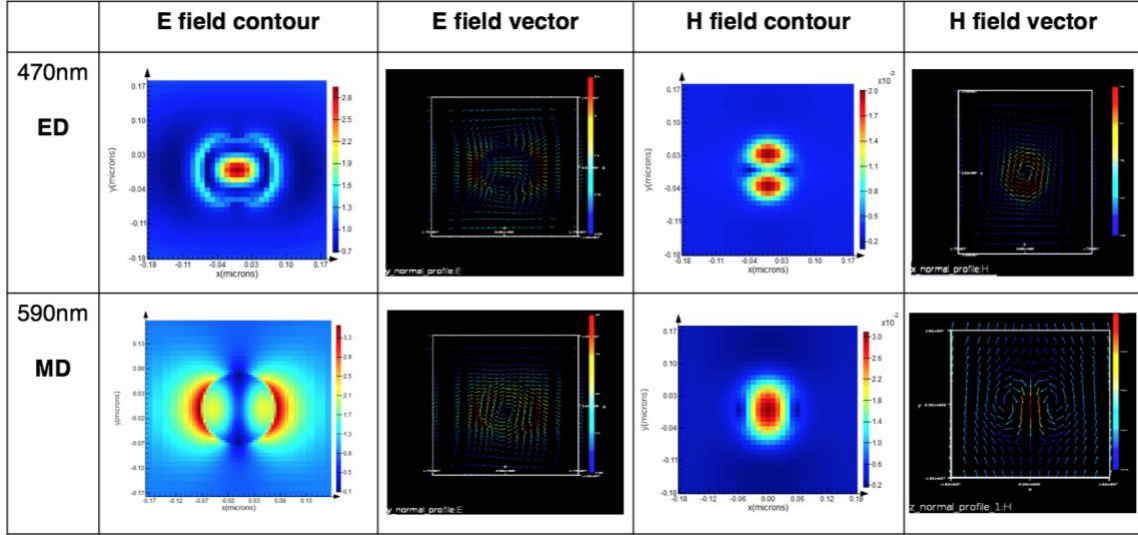
Figure 2.3 Electric and magnetic dipole in a 140nm in-diameter silicon nanoparticle on silica substrates

2.1.3. Pancharatnam-Berry phase based metasurfaces

Gradient metasurfaces are flat optical elements capable of manipulating light by generating local, space-variant optical phase from the incident electromagnetic waves[59]. These surfaces usually employ nanostructures as the meta-atom to generate local phases. The Pancharatnam-Berry phase is one of the methods for generating the geometrically distributed phases in metasurfaces. The control of the phases for transmitted (or reflected) light with opposite helicity can be realized by only the orientation angle of the nanoresonator[56].

The manipulation of polarized light can be described using the Jones calculus. Polarized light can be presented as Jones vector and a linear optical element can be defined as Jones matrix. Therefore the correlation between incident and outgoing light can be described as below[74], where the J stands for the Jones matrix. In the equation, the 2θ entails the additional 2θ phase shift introduced by the rotation of the scatter.

$$E_t^{R/L} = J * E_i^{R/L} = \frac{t_0 + t_e}{2} E^{R/L} + \frac{t_0 - t_e}{2} e^{im2\theta} E^{L/R} \tag{2.5}$$

i/r: incident/reflected light;
R/L: right-hand/left-hand circular polarization
t_0 and t_e: transmission coefficients for Ex and Ey, can be reflection too
m=-1/1 for right/left -hand polarized incident light
Computational optics can be used calculated phase distribution over a plane based on the intended optical functionalities or holograms[34,56] in the far-field. With the above correlation of the geometry and the phase delay, we can calculate the geometry pattern distribution for the lithography required afterward.

2.2 Heat Transfer

For nanostructures receiving laser irradiation, the laser first heats the structure based on carrier excitation resulting from the optical coupling. Heat then transports within the nanostructure. Lastly, the heat dissipates across the interfaces to the surrounding environment while there are additional phase transformation and geometry changes happening within the nanostructure.

2.2.1 Laser heating

Laser heating of solid materials is defined by a sequence of processes, including the electromagnetic wave coupling of the material, carrier excitation and the relaxation to the thermal carriers. For the time scale above 10 ns, thermal equilibrium is obtained between the excited carriers and the thermal carriers[53], which in our case are phonons. In this dissertation, we consider heating is fully relaxed in Chap. 3 and 4 and non-equilibrium in Chap. 5. For Chap. 3 and 4, the absorbed laser irradiation will be recognized and modeled as heat source terms inside the simulated domain.

Laser heating of bulk material (silicon wafer) follows the Beer-lambert Law, where the absorption can be calculated based on the exponential decay of the incident intensity. Eqn. 2.5-2.6 described the law based on plane wave incident on a bulk wafer, where z is the depth inside the wafer and α is the absorption coefficient of the light.

$$I_z(t) = I_0(t)e^{-\alpha z} \tag{2.6}$$
$$I_{abs}(t) = \alpha I_z(t) = \alpha I_0(t)e^{-\alpha z} \tag{2.7}$$

For laser heating of thin films (silicon film on oxide), the optical thin film interference model is required to estimate the total absorption as well as the absorption profile. Depending on the extinction coefficient, some extreme cases can be simplified. If the extinction coefficient is small compared to the substrate, then the absorption lies mostly on the substrate and we can model the heating with the beer-lambert law. If the extinction coefficient is so high that light cannot penetrate through, like most metals, then absorption is mostly within the thin film. Then the heating will be modeled within the thin film layer, which in most cases Beer-Lambert law also holds. In our study, silicon thin film is sitting on a silica substrate, whose absorption is negligible compared to silicon. Therefore, we consider silicon thin film will be the absorbing layer.

For laser heating of the nanostructures, comprehensive FDTD simulation should be carried out to obtain the 3D absorption profile. 3D heat transfer model is required to account for the absorption as well as the heat dissipation. The FDTD simulation method is described in section Appendix A1 and be used to explain the results in Chap. 3. However, for studies on solidifications (Chap. 4), the detailed heating process is not critical compared to the cooling. Hence for comprehensive simulation in Chap 4, heating is modeled as either following Beer-Lambert law or homogeneously.

2.2.2 Heat transport in nanoscale solids

For the heat dissipation processes, heat conduction dominates compared to the radiation and convection. The detailed comparison of the order of magnitude is given below in Table 2.1. Here the conduction is calculated based on the cooling rate in silicon oxide, which is the main substrate studied in this dissertation. The dimension d for the conduction is estimated as the thermal diffusion length as $L = \sqrt{\alpha t}$. The diffusivity α can be read from Table. 2.2 and the time t is selected to be 50 ns, where the maximum undercooling exist (see details in Chap. 4.4). As can be seen from Table 2.1, the conduction is at least 4 orders of magnitude larger than the convection and radiation.

Table 2.1 Comparison of the different heat transfer mechanism

Mechanism	T/T$_0$(K)	Parameter	Equation	Value
Conductive heat transfer	1498/298	k=1.5 Wm/K d=150E-9 m	k(T-T$_0$)/d	1.2E10
Convective heat transfer	1498/298	h=0.5~1000 W/(m$_2$K)	h(T- T$_0$)	<1.2E6
Radiative heat transfer	1498/298	σ =5.67E-8 W/(m$_2$K$_4$)	σ(T$_4$-T$_{04}$)	2.8E5

Before solidification, the quenching is affected by the conduction of liquid silicon, thermal interface resistance between liquid silicon and oxide substrate and the oxide conduction. After solidification happens, we need to additionally analyze the condition in solid silicon as well as its thermal interface resistance with silica substrate.

For both liquid and solid silicon, the magnitude of the thermal interface resistance is negligible compared to the resistance from the substrate. The magnitude of the thermal interface resistance between solid silicon and oxide is found to be in the order of $0.9 \times 10^{-9} \ Km^2/W$ at the strong coupling limit[75]. There is no available data describing the thermal interface resistance between the liquid silicon and silica interface, which is considered similar to that from solid silicon. The substrate's thermal resistance can be estimated as *L/k*, where L is the dimension of the thermal conduction. The resistance is then estimated to be $1 \times 10^{-7} \ Km^2/W$. As the interface resistance is 2 orders of magnitude smaller than the substrate resistance, the quenching will not be limited by the interfacial resistance and the temperature variation will lie mostly on the substrates.

Table 2.2 The thermophysical properties of materials at 300 K and atmosphere presssure

Materials	k (W/mK)	ρ (kg/m$_3$)	C$_P$ (J/kgK)	α (m$_2$/s)	Melting Point(K)
Poly-silicon	6	2329	710	7.86E-05	1685
Amorphous Si	1.5	2285	710	9.25E-07	1485
Liquid silicon	430	2540	971	1.7E-4	-

Silicon oxide	1.5	2700	1000	5.56E-07	-
Silicon nitride	15	3184	720	6.54E-06	-
GST	1.4	6400	212	1.11E-6	900

As for the thermal conductivities in the solid and liquid phases, we consider the Fourier law still holds for the polycrystalline and amorphous silicon nanostructures with sizes around 100nm size. Ballistic transport happens when the mean free path of the carrier is much longer than the dimensions of the medium wherein carriers travel. For the thermal conduction in silicon nanostructures, the carrier system is phonons. From Matthiessen's rule, the mean free path is the harmonic mean of the various scattering mechanisms' characteristic length. In our study, the silicon nanostructures are either polycrystalline or amorphous, where the grain boundary scattering becomes the major scattering contributor. Hence its mean free path is limited by the size of the grains, which is smaller than the dimension of the nanostructures. Ballistic transport is therefore not considered in our analysis and thermal conductivities from 64 nm grained nanocrystal silicon have been used for the simulation[76,77]. However, for studies involving single crystal nanostructures, ballistic transport is possible but hard to model as the heat coupling is volumetric based on the resonance effects. This effect remains to be explored by further studies. Liquid silicon thermal conduction is diffusive hence experimentally measured conductivity is utilized in in our model. Temperature-dependent thermal conductivities are applied to the amorphous and polycrystalline silicon as well as the silica.

2.3 Phase transformation theories

The first-order phase transformation between liquid and solid silicon is studied in this section. First-order phase transitions exhibit a discontinuity in the first derivative of the free energy with respect to a certain thermodynamic variable[78]. Or in a modern definition, first-order phase transformation involves latent heat. Second-order phase transitions are continuous in the first derivative but exhibit discontinuity in a second derivative of the free energy.[78]This category includes the ferromagnetic phase transition in materials. In this dissertation, thermodynamics analysis is carried out in the isothermal and isobaric system, when quasi-steady-state assumption is made based on the quench rate we observed in Chap 3 and 4. Therefore the Gibbs free energy is used for analyzing the nucleation. In our experiments, the Gibbs free energy change is introduced by the temperature. The temperature difference from the equilibrium melting temperature is termed as supercooling or superheating.

2.3.1 Different phases of silicon

The temperature-pressure phase diagram of silicon has been studied extensively. It is known that the diamond structure of silicon (Si-I) under the atmosphere pressure undergoes a well-characterized first-order transition upon pressurization to the β-Sn structure phase (Si-II) and both phases melt as temperature increases. In this dissertation,

diamond structured silicon will be studied and termed as crystalline silicon(c-Si). The polycrystalline silicon is a combination of crystalline silicon grains with different crystallographic orientation connected with each other. It still falls into the category of crystalline silicon but with different thermal, electrical and mechanical behavior inherited from the grains boundaries,

Amorphous silicon is an allotrope of silicon which can stably exist. The amorphous silicon (a-Si) contains similar tetrahedral coordination in the short-range, given that the long-range order is missing and a significant amount of dangling bonds exist (Fig. 2.4). In lower pressure, the amorphous phase is low density , and thus is called low density amorphous (LDA). At higher pressures, amorphous silicon changes from semiconducting to metallic and becomes more coordinated, leading to high-density amorphous phase (HDA)[79].
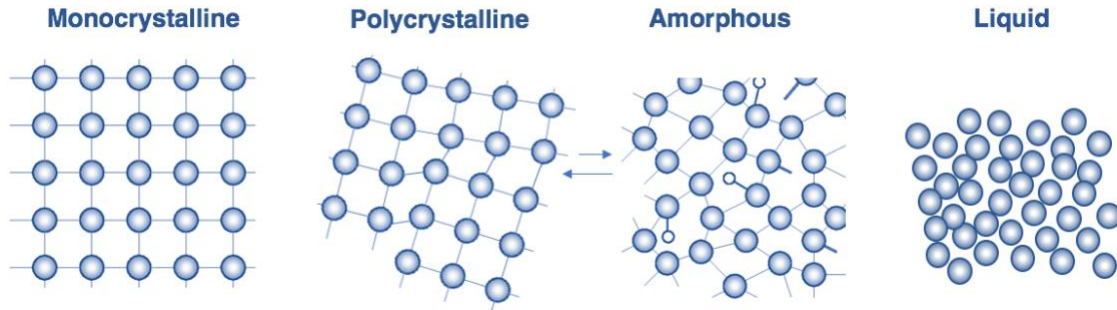
Figure 2.4 Schematics of different crystalline phases in silicon material

Liquid silicon (l-Si) is metallic at high temperature, with some evidence showing that it possesses a small population of covalent bonds[80]. The coordination number $N_c = 7.3$[81] is higher than that in c-Si(Fig. 2.4). As a result, l-Si has a higher density than c-Si, a property that silicon shares with water[82]. The high-density liquid is therefore termed HDL. It has long been postulated a low-density liquid phase exists transiently during the phase transformation of liquid to amorphous or crystalline. The details of these transitions are not expanded in the current section.

In this dissertation, the phase transformation study will mainly focus on the transformation between amorphous and polycrystalline silicon. While there are pressure-based methods to achieve this transformation, we are more interested in the temperature based ones, which is through laser heating in the current experiment. Practically, the liquid state is usually involved for the order-disorder transformation through temperature variation. Therefore in this dissertation, we will focus on the phase transformation of the liquid state, crystalline silicon and amorphous silicon.

Crystallization describes the phase transformation from the liquid silicon to crystalline silicon, which is the most well-understood transformation that of interest. The transformation between liquid silicon to amorphous silicon is however not well understood. We will use the framework of crystalline to build our simulation model and explain some of the observed experimental results in both crystallization and amorphization. Subsequently, insights are also obtained on the liquid to amorphous phase transformation.

2.3.2 Classical nucleation theories

The kinetic aspect of the phase transformation becomes critical to the central goal of manipulating the phase transformation in nanoscale. Nucleation and crystal growth are two major topics for studying crystallization kinetics. A series of models[83] are formed to describe the rate of forming the crystalline nuclei and driving the interface velocity between the crystalline phase and the liquid phase. We will first cover the nucleation theories in this section and crystal growth will be covered in section 2.3.4.

Free energy change is the first step to understand the kinetics of nucleation. The free energy reduces when the liquid silicon phase transformed into the crystalline phase under supercooling. However, the nucleation, i.e. creation of a new phase inside the liquid phase causes additional free energy to increase due to the increased surface energy. Based on this competition, a nucleation size-dependent free-energy change chart can be drawn (Fig. 2.5). The formation of nuclei is a statistical thermal fluctuation event for a given total number of molecules/atoms. The same statistical fluctuation controls the growth and dissociation of the nuclei. As can be seen in the plot of Fig. 2.5A, only those nuclei reached the critical radius r_c can keep growing as the increase of the nuclei's radius drives down the total free energy. Those smaller than the critical radius will dissociate into the original phase.
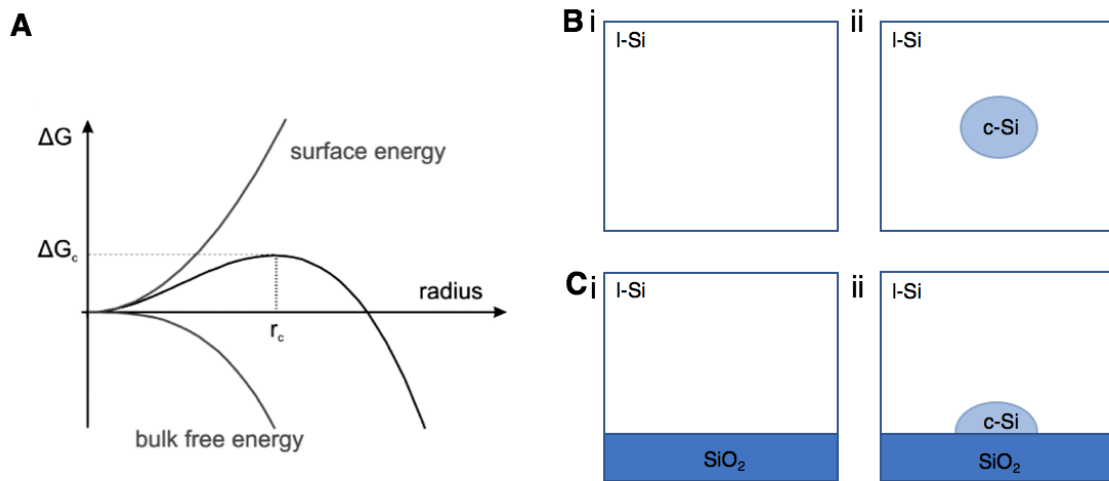
Figure 2.5. Free energy change of a nucleation event. (**A**) Schematics of nucleation radius vs. the free energy reduction. r_c here stands for the critical nucleation radius. (**B-C**) Schematics of homogeneous and heterogeneous nucleation mechanisms. (B) before(i) and after(ii) homogenous nucleation. (C) before (i) and after(ii) heterogeneous nucleation.

Homogeneous and heterogeneous nucleation present different free-energy change. As can be seen from the schematics in Fig. 2.5B, for the homogenous nucleation, the creation of a new phase increases the free energy by the area of the nuclei's surface. The free energy change for homogeneous nucleation can be obtained as follows, where the T_m

stands for the melting temperature, and Lc is the latent heat, γ_l is the surface tension of the liquid phase.

$$\Delta G_{hom,c}(T) = \frac{16\pi\gamma_l^3 T_m^2}{3\rho^2 L_C^2 (T - T_m)^2} \tag{2.8}$$

For heterogeneous nucleation, the free energy change has a correction factor. The nucleation additionally creates an interface between the new phase and the substrate(Fig. 2.5B). The correction factor is listed below, where the θ is the contact angle.

$$fc(\theta) = \frac{1}{4}(\cos^3(\theta) - 3\cos(\theta) + 2) \tag{2.9}$$

which gives

$$\Delta G_{het,c}(T) = \Delta G_{hom,c}(T)\, fc(\theta) \tag{2.10}$$

Various modeling work has been developed to establish Classical Nucleation Theories(CNT) since the initial formulation by Volmer and Weber[84]. CNT treats the nucleation rate by establishing a series of reactions between single molecules and the existing cluster. Both transient and steady-state treatment has been proposed to offer the solution of the CNT depending on whether the nucleation is at the equilibriums of atomic reactions[85].

As we will reveal later, the cooling rate for the crystallization studies in this dissertation still falls into the category of quasi-steady-state nucleation with negligible effects from non-thermal nucleation[86,87]. The same nucleation model is applied to explain the melt duration as well as the solidification time for the amorphization. While we believe this model can readily explain the experimental data, the nucleation model may not predict an accurate number of nuclei at the ultrafast time scale.

Based on the simplified models[85], we obtained the following equations for the nucleation rates in steady states. In the simulator described below, the N_{het} and N_{hom} coefficients in front of the exponential term are obtained as 10^{27} (m[2].sec)[-1] and 10^{39} (m[3].sec)[-1] from Ref.[88].

$$Nr_{hom}(T) = N_{hom}\exp\left(-\frac{\Delta G_{hom,c}(T)}{Tk_B}\right) \tag{2.11}$$

$$Nr_{het}(T) = N_{het}\exp\left(-\frac{\Delta G_{het,c}(T)}{Tk_B}\right) \tag{2.12}$$

2.3.3 Monte Carlo simulation of the nucleation

CNT does not lead directly to the stochastic description of the nucleation process. In the temporal stochastic nucleation modeling, Poisson's process is recognized as the appropriate method[88,89]. In Poisson's process, the arrival rate or the intensity defines the expected value for the number of events happening in a given time. It is helpful to understand the simplest case of studying this probability, which is the probability of no nucleation occurance in a confined volume V_D with total elapsed time t. If we assume the process has a constant rate Γ_D, from homogeneous Poisson's expression for zero-event successes, we can obtain $P_{LIQ}(t)$ through :

$$P_{LIQ}(t) = P\{N = 0\} = \frac{(np)^0}{0!}\exp(-np) = \exp(-\Gamma_D t) \tag{2.13}$$

$$P_{NUC>1}(t) = 1 - P_{LIQ}(t) = 1 - \exp(-\Gamma_D t) \tag{2.14}$$

The constant rate Γ_D is equal to the nucleation frequency, which is defined as below, where A is the interface area for the heterogenous nucleation

$$\Gamma_D = V_D * \text{Nr}_{hom} + A * \text{Nr}_{het}. \tag{2.15}$$

In reality, the temperature-dependent rate Γ_D leads to a heterogeneous Poisson process. A true representation should involve a full consideration of all the previous time steps. Then Equation 2.12-13 are transformed to an integral form:

$$P_{LIQ}(t) = \exp\left(\int_0^t -\Gamma_D(T(t))dt\right) \tag{2.16}$$

$$P_{NUC>1}(t) = 1 - \exp\left(\int_0^t -\Gamma_D(T(t))dt\right) \tag{2.17}$$

Based on such assumption, we can derive the probability of the 1st nucleation falls at (*t, t+dt*) is the product of the probability that no nucleation for all the elapsed time *t* and the probability that it nucleated at elapsed time *t+dt*:

$$P_{NUC-1}(t, t + \Delta t) = \exp\left(\int_0^t -\Gamma_D(T(t))dt\right) *$$
$$(1 - \exp\left(\int_t^{t+\Delta t} -\Gamma_D(T(t))dt\right)) \tag{2.18}$$

We will then discuss how to implement the Monte Carlo simulation to simulate the stochastic nucleation. From the simulation point of view, we first discretize the total volume into rectangular grids. To carry out Monte Carlo stochastic simulation, we examine every liquid node at time *t* and inquire whether it is about to nucleate. Different from the above equations, only the 2nd part of the product has remained as we have known that the node stays liquid for the elapsed time t. Then the probability of nucleation is unity minus the probability of avoiding any nucleation at *t+dt*, which is given below:

$$P_{NUC}(t, t + \Delta t) = (1) * (1 - P_{LIQ}^{ijk}\big|_{t,t+\Delta t}) \tag{2.19}$$

Compared to Eqn. 2.16, we consider every step as an individual separate isothermal process and a chain of such processes formed the entire phase transformation. There are two ways of evaluating $P_{LIQ}^{ijk}\big|_{t,t+\Delta t}$. First, it is to evaluate the conditional probability of no nucleation happen in (*t, t+dt*), which should be the quotient of unconditional probabilities of no nucleation happen in (*t+dt*) over no nucleation happen in *t*. Another way is to evaluate through the integral of Eqn.2.16. In both ways, we obtained identical the formulation as below:

$$P_{LIQ}^{ijk}\big|_{t,t+\Delta t} = \frac{\exp(-\Gamma_D(t+dt))}{\exp(-\Gamma_D t)} = \exp\left(\int_t^{t+\Delta t} -\Gamma_D(T(t))dt\right) = \exp(-\Gamma_D dt) \tag{2.20}$$

Hence, the probability for nucleation is (d*h* is the dimension of the node):

$$P_{he} = 1 - \exp(-\text{Nr}_{het}(T)dh^2 dt) \tag{2.21}$$

$$P_{hom} = 1 - \exp(-\text{Nr}_{hom}(T)dh^3 dt) \tag{2.22}$$

2.3.4 Crystal growth

The temperature-dependent crystal growth is characterized by the interface response function. Two typical theories are used to describe the interface velocity for the interface response function, i.e. the transitional states theories(TST) and diffusion limited theories(DLT). [90] Both theories employed the same structure of formalism as follows,

where Q is the activation energy, ΔG_{ls} is the Gibbs free energy difference between liquid and solid silicon, k_B the Boltzmann constant, and c is the related kinetic constant[91]:

$$v(T) = c\, e^{-\frac{Q}{k_B T}}(1 - e^{-\frac{\Delta G_{ls}}{k_B T}}) \tag{2.23}$$

Stolk *et al*. [90] found out for silicon epitaxial crystallization on from amorphous silicon that the DLT agrees better with the measured data. Therefore the model and the corresponding fitting parameters are used for the crystallization simulation in the super-lateral crystallization in chapter 3. For the comprehensive phase transformation simulation introduced later, the generation of latent heat in the heat transfer equation (2.24-25) will be calculated based on this growth rate and the subsequent change in solid/liquid fractions of each finite-difference grid inside the simulation.

2.4 Coupled simulator for heat transfer and phase transformation

Pulsed laser heating induced phase transformation is a time-dependent multiphysics process. Heat transfer and phase transformation are coupled and need to be solved at the same time. There are simple phase transformation coupling in COMSOL, however, it does not account for the nucleation process. To the best of our knowledge, there is no commercial or open-source program that is capable of simulating the stochastic nucleation process. Hence a house-built simulator is required and has been developed.

The simulation models are inspired by the papers from Leonard[88,89]. The simulator is originally developed by Jung Bin In[91,92] including the C++ package and the Matlab main program. Letian Wang verified and documented the algorithm, added additional data monitoring and geometry import functionalities, developed a proper user interface for running and analyzing batches of simulations.

The temperature distribution is obtained through solving the transient heat conduction partial differential equations. The heat transfer equation solved are listed as below, where $\dot{Q}_{hv}$ stands for the laser heating and the $\dot{Q}_L$ stands for the latent heat associated with phase transformation.

$$\rho C_p \frac{dT}{dt} = \nabla \cdot (k\nabla T) + \dot{Q} \tag{2.24}$$

$$\dot{Q} = \dot{Q}_{hv} + \dot{Q}_L \tag{2.25}$$

The simulation process flow is demonstrated in the block diagram in Fig. 2.6. The geometry is discretized into rectangular grids. Then finite difference method is used to iteratively calculate the temperature from the heat transfer equation. A new scalar φ is updated in every time step to describe the ratio of different phases within one grid, which includes crystalline, amorphous and liquid phases. When the emperature of this node is higher than the melting point, the solid phase will began to transform into liquid. There is no nucleation modeling on the melting part.

The nucleation is modeled during the solidification process. In each time step, we will first check if the node is full of liquid or has some residual of the crystals. Only when full of liquid, nucleation is possible. In that case, we calculate the nucleation probability based on Poisson's process and CNT. Homogeneous nucleation inside the liquid as well as heterogenous nucleation from the silicon and oxide surface has been modeled. Due to the downward heat conduction direction, the free surface will have much smaller

undercooling compared to the oxide interface. As a consequence, the nucleation in the free surface is not modeled. After we obtained the nucleation rate, then a random number generator is applied to generate a real random number between 0 to 1. Since the probability in a single node is at the order of 10^{-15}, a high precision random number generator should be applied to appropriately capture the low probability event[89](dSFMT). If a new random number is smaller than the predicted probability, we consider nucleation has happened, then the scalar standing for the crystal phase will start to accumulate the crystal growth based on the growth rate specified. For crystal growth, the ratio of the crystalline phase will increase at a speed of the crystal growth speed. Once the node is filled with solid, it will expand the growth to the neighboring grids. With a 32-bit float precision, it is of very low chance that the crystal growth just complete in one grid and stop expansion. Therefore, it is assumed this node-by-node expansion can mimic the crystal growth in the macro scale. It is noted that all the crystals grown from one nucleus will share the same crystal identifier to define its crystal grain[91]. The detailed numerical scheme and software architecture is introduced in Appendix A2.
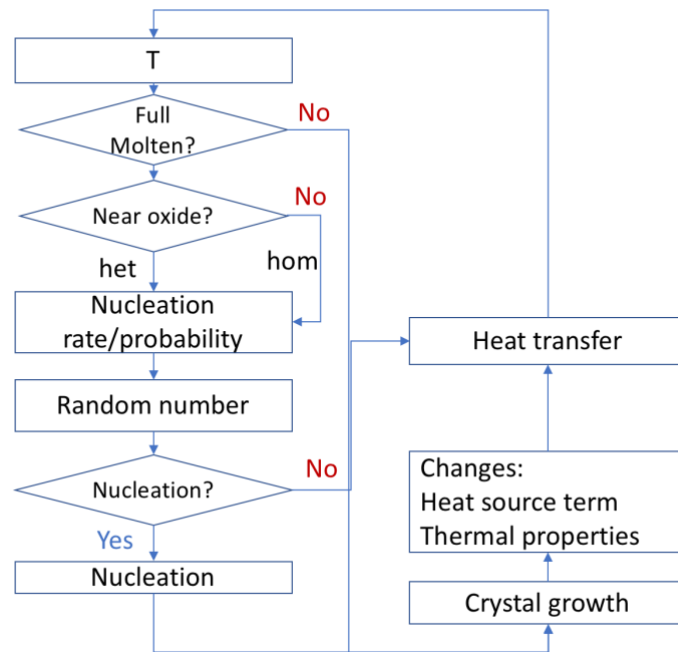
Figure 2.6 Block diagram and flow chart for the simulation of heat transfer, nucleation and phase transformation

The numerical scheme of the time-dependent simulation is based on finite difference time stepping. For the simplicity of implementation, an alternative-directional-explicit (ADE) algorithm. An empirical guideline for stability consideration is that to adjust the time steps that the maximum volumetric phase change rate of the unit cells was limited below 0.25 % during each time step[91]. The simulation domains are separated as silicon and substrate. The phase transformation is only calculated at the top silicon domain while the heat transfer is calculated in both domains. The minimum size of the cubic grid was 10 nm at the silicon domain, but larger meshes were used for the structures below the silicon to reduce the computation and speed up the simulation.

2.5 Nanofabrication

We follow a conventional CMOS fabrication process in Berkeley Marvell Nanolab. In Fig. 2.7, we show that the overall process consists of thin-film deposition, mask design, lithography, and reactive ion etching (RIE). The details of the fabrication process can be found in Appendix A3.

1. Thin Film Deposition
A
a-Si film on silica

2. Photolithography
B
photoresist on a-Si film

3. Reactive Ion Etching
C
a-Si disks on oxide mesa and substrate
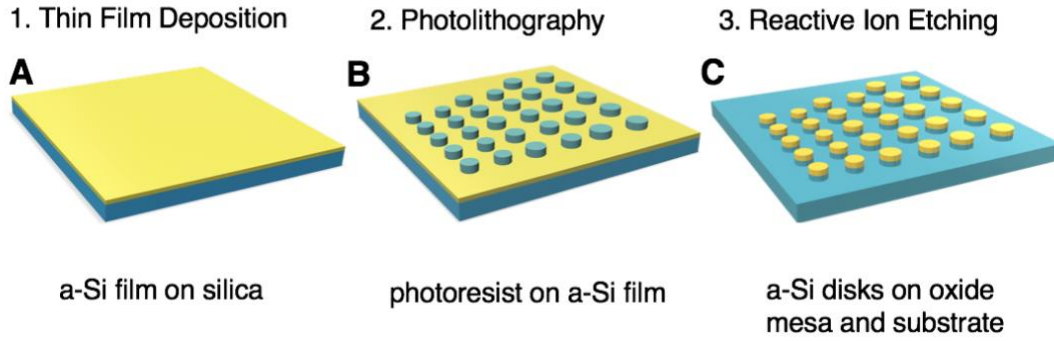
Figure 2.7 Fabrication process flow for the nanoresonators

For the study of reversible phase change, we obtained single crystalline silicon nanostructures on silica through the transfer-based fabrication method[56]. Then asymmetric geometries and the 400nm period nanodisk arrays are patterned through Electron Beam Lithography (Crestec) and same RIE.

2.6 Characterization

Optical microscopy is applied to characterize every step of fabrication and laser processing. For the images displayed in this dissertation, an optical microscope (Olympus BX60) and CMOS camera (AmScope MU300) have been utilized to characterize the optical bright field and dark field images. It is important to note the white light illumination from microscopy is non-coherent, which will not excite the group resonance of the nanodisks. Therefore, its optical characteristics is equivalent to a single nanodisk.

Raman spectroscopy is employed to identify nanodisk of the polycrystalline silicon and amorphous silicon. The Raman spectroscopy is typically used to determine the vibrational, rotational and other low-frequency modes of molecules. In semiconductor solids, it has been successfully used to determine lattice dependent vibrational modes of the atoms. For crystalline and amorphous silicon, distinct Raman shift spectra are observed and well-studied[93], which is used for tracking silicon phase transformation in this dissertation. Raman spectroscopy on silicon nanostructures contains additional features compared to bulk silicon, including resonant excitation[94], surface-enhanced Raman spectroscopies(SERS), phonon confinement modes etc. Resonant excitation and SERS effect is not considered as the intensity of Raman peak is not used in our analysis. The phonon confinement can be used to correlate the size distribution to the peak position width, asymmetry and full-width half maximum[95], which is however not utilized in this study.

Raman spectroscopy mapping is further applied to investigate the laser energy-dependent phase transformation on the nanodisk. With densely pack nanostructure arrays of different geometries, one simple scan of laser pulses can generate big groups of both energy variant and statistically distributed processing results(Fig. 2.8A). The high throughput feature of Raman mapping ensures the speed of data collection under a controlled instrument condition. Overall, quantitative screening of the effect of laser fluence and nanoparticle geometries on phase transformation is significantly accelerated.

A Renishaw inVia Micro Raman System with a 532nm laser excitation source, 100X objective lens (Olympus MS Plan, NA0.95) and a 100nm-resolution motion stage are used for Raman spectra mapping. The mapped spectra are analyzed with the built-in WiRE 3.3 software. Spectra curves are fitted with combined Gaussian and Lorentzian profiles with the peak centered between 480-522 cm-1.
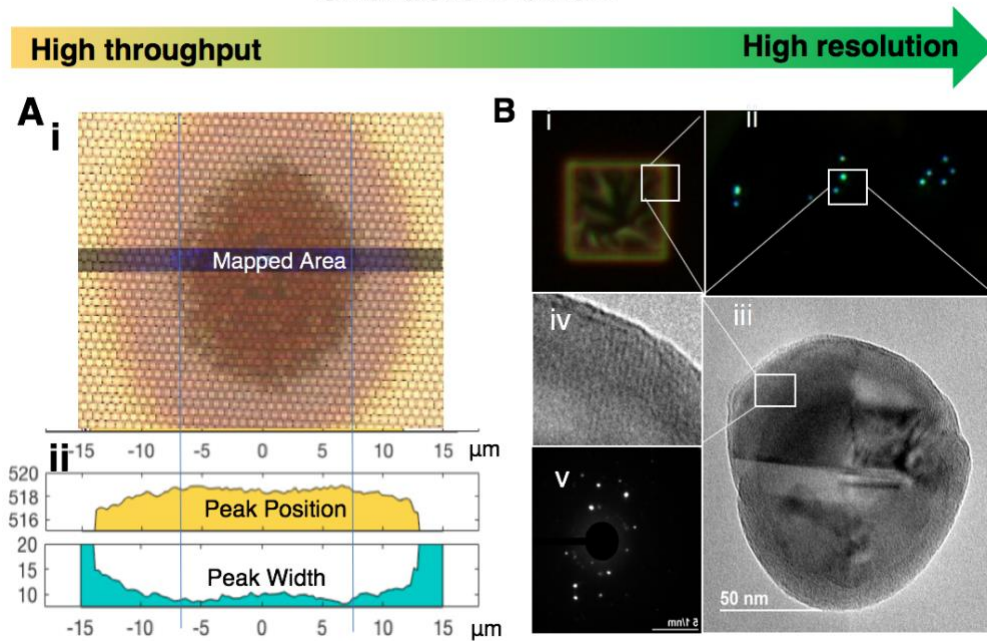
Figure 2.8 Schematics of the characterization method used in the present work. (**A**) The optical and Raman spectroscopy mapping coupled high throughput characterization. (**B**) The transfer-based TEM characterization method.

Scanning electron microscopy(SEM) is utilized for characterizing the geometry and chemical composition. The gold coating is avoided to preserve the crystallinity characteristic after laser processing. To reduce the charging effect, multiple contact regions are utilized during the mounting of the sample and the electron voltage and current are set to be low (10kV, 80nA). Electron Backscattered Diffraction (EBSD) mapping has a spatial resolution of 100nm, which helps the crystallization characterization in the thin film. But the resolution is not enough for the characterization of nanodomain crystallinity. EDS mapping helps to define the material composition in the laser processed area, which is important for one collaborated work. Transmission electron microscopy(TEM) images are taken from the Lawrence Berkeley National Lab(LBNL) microscopy center with assistance from Dr. Frances Allen. The TEM sample preparation requires transferring the processed silicon nanoparticles onto

electron transparent membranes, which are the 20nm /40 nm thick silicon dioxide membrane in this case. In my dissertation, the femtosecond laser has been irradiated from the backside of the sample and used to induce mild ablation and shock wave at the interface of the nanoparticle and oxide substrate. The subsequently generated recoil force is the driving force to transfer the nanoparticle to the membrane. The optical dark-field image is first used to locate the transferred nanoparticle. The nanosecond laser-induced dewetted nanoparticle in this Fig 2.8 B shows a polycrystalline structure.

3 Optically modulated self-assembly

3.1 Introduction

Recent advancement in dielectric metasurfaces and structural color leads to the active research towards the fabrication of the dielectric nanoresonator array. As we discussed in the introduction 1.1, the scalable nanomanufacturing of dielectric particle array is critical for the wide application of the novel devices. Various on-demand printing and patterning have been proposed. Printing Si resonators with tunable size was realized using the Laser-induced Forward Transfer (LIFT) method.[32] However, this method requires accurate alignment of the laser beam onto the donor substrate as well as synchronization of the donor and receiver substrate positions for writing complex nanoparticle arrays with submicron unit size,[96] which limits its scalability. Surface morphologies of Al[23] and Ge islands [24] were precisely tuned through laser pulse energy density and polarization, which successfully demonstrated laser's application in structural color printing. Therefore, a final milestone would be the development of a process that can pattern and tune the particle number, placement and size in a scalable fashion.

In this work, we realized Laser-induced Modulated Assembly (LiMA) to optically manipulate the nanostructure assembly process and simultaneously modulate the nanoparticle size, number and placement. It is noteworthy that in typical dewetting the laser pulse acts simply as a transient heat source. In contrast, the LiMA process relies on the modulation of the local laser absorption due to the near-field optical energy coupling. Due to the near field interaction, LiMA does not require elaborate focusing of the laser beam and is easily scalable. The present method can ultimately produce mono-periodic, bi-periodic and tri-periodic patterns, hence directly facilitating the application of Fano resonance [97,98] and spectroscopy.[99] The content of this section has been published in ACS Nano[100] .

3.2 Laser-induced modulated assembly (LiMA)

3.2.1 Methods and overview

With the described methods from section 2.5, here 30nm thick amorphous silicon film is deposited on the silica substrate. These pre-patterned holes varying from 250 to 500nm in diameter are spaced with a period of 800nm, which can be seen in the Fig. 3.1A.

For laser processing, a high power Nd:YAG pulsed laser (New Wave Solo II Laser, 532nm, 13 ns) is employed to generate large area arrays for characterization. The YAG laser is focused using a Mitutoyo APO 2X objective lens with a beam diameter at 40 microns. A high repetition rate Nd:YVO$_4$ laser (Spectra Physics Navigator, 532nm, 25 ns) is employed to study second pulse effects on tuning of the Si nanoparticle property. The laser is focused with a Mitutoyo APO 2X objective lens, creating a beam size of 15 microns in diameter.

A commercial-grade simulator (Lumerical FDTD[101]) based on the finite-difference time-domain method was used to perform the calculations. For "S" particle, a 140nm in diameter nanoparticle is placed on top of a 5 μm quartz with 10nm overlapping to depict the truncated geometry. For "L" particles, a 220 nm nanoparticle with 20nm overlapping is adapted to describe the truncated geometry. The plane-wave source is at 2 μm distance on top of quartz and the FDTD domain contains the source and a 2 μm quartz domain. Crystalline Si (c-Si) properties are selected from the built-in model while amorphous Si (a-Si) properties are from Ref.[102]. Reflection monitor with a spectrum resolution 10nm/point is placed at a height matching the numerical aperture of the objective lens we used. 5nm grid in the xy plane and 2nm grid in the z direction with 1000 fs simulation time are applied.
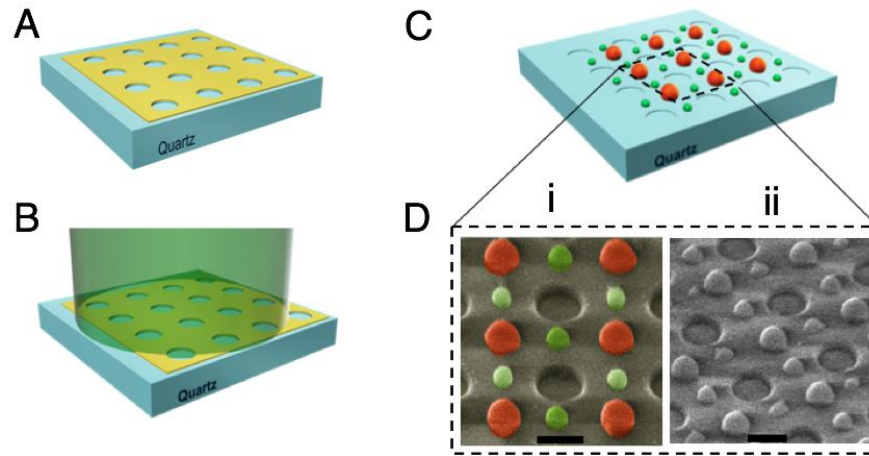
Figure 3.1 Schematics of experiment and the dewetting phenomena. (**A**) The patterned amorphous silicon thin film on silica. (**B**) the nanosecond laser irradiation on the patterned thin film. (**C**) The silicon nanodot array formed by dewetting. (**D**) The SEM images of the dewetted nanodots from a 20nm thick amorphous Si film with 335 nm hole size irradiated by a single 13 ns laser pulse at 1.5 J/cm^{2} fluence. Reproduced with permission from ref [100] Copyright 2019 American Chemical Society.

As a result of dewetting induced assembly, a large Si nanoparticle (termed as "L" particle) was formed at the center of four neighboring holes (Fig. 3.1D). Each hole is surrounded by symmetrically placed smaller sized particles (the "S" particles). The assembled particles are of bottom-truncated spherical shape (Fig. 3.1D). Theoretical studies[103–106] have shown that non-spherical particles can be effectively modeled to predict and design resonators for metasurface applications. The L nanoparticle size fell at 230±10nm while the S particles were in the range of 140±10nm. An "Orange-Green" false color combination is added into the SEM image in Fig. 1A, iii, corresponding to the actual bright-field micrograph (Fig.3E, i) that shows an "Orange+Green" alternating pattern.

Laser-induced modulated assembly (LiMA) of nanoparticles in 2D is schematically shown in Fig. 3.2. Modulation of the nanoparticle arrangements (including size, number, and symmetry) is achieved by adjusting the laser beam polarization, amplitude and number of pulses. As the fabrication of Mie resonator metasurfaces, LiMA

enables the deliberate placement of the resonance peak and active selection of resonator combination.
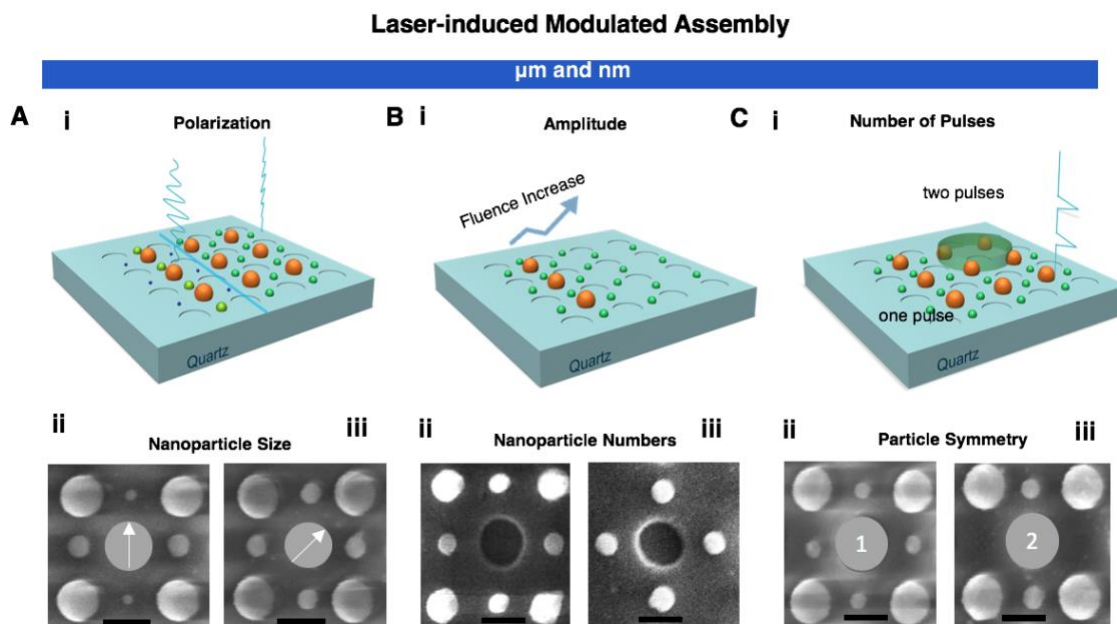
Figure 3.2 Schematics and characterization of laser-induced modulated assembly (LiMA). Detailed methods include (**A**) Polarization direction; (**B**) laser fluence and (**C**) number of pulses. Representative SEM images of the fabricated Si nanoparticle array are displayed in the subfigures (ii-iii), showing the capability of manipulating the nanoparticle size, number of nanoparticles, and particle symmetry. Reproduced with permission from ref 100 Copyright 2019 American Chemical Society.

3.2.2 Polarization based modulation

Light polarization is the key LiMA mechanism that features near-field absorption and can be harnessed to tune the nanoparticle size. Using a sample rotational stage, the polarization was set at angles of 0°, 45° and 90° with respect to the horizontal (+x) direction. Here, a 22 nm thick amorphous thin film with 250 nm hole pattern was irradiated by one 13 ns laser pulse. As illustrated in Fig.3.3 A(i-iii), the assembled S particles exhibited an interesting size variation against the polarization angle. In the case of light polarization in the horizontal direction (Fig. 3.3Ai), smaller S particles (i.e. "S$_P$" (70±10 nm)) are produced in the polarization direction (P), while larger S particles (i.e. "S$_{PP}$" (170±5 nm)) are formed in the perpendicular direction of polarization (PP). On the other hand, laser irradiation polarized at a 45o angle produces just S$_{PP}$ particles (Fig. 3.3A, ii). The configuration is shown in Fig. 3.3A-iii is identical to the one in (i) but rotated by 90o. The size of S$_P$ nanoparticles falls in the deep-blue scattering range. Note that the scattering captured under optical microscopy was overwhelmed by the response of major resonator L particles. Finite-Difference Time-Domain (FDTD) simulation

revealed spatially varying absorption based on the near-field light coupling to an amorphous nano-patterned Si film. The simulated absorption distribution in a unit cell is presented in Fig. 3.3B(i-iii). Due to near-field optical effects, the local absorption enhancement is strongly dependent on the polarization angle. The local absorption distribution can be mapped into 4 quadrants; the left/right quadrants are labeled in the "x direction" and the up/down quadrants are in the "y direction". As noted in Figs. 3.3 B and E, the distribution of the local absorption maxima (termed as "hotspots") is perpendicular to the polarization direction.
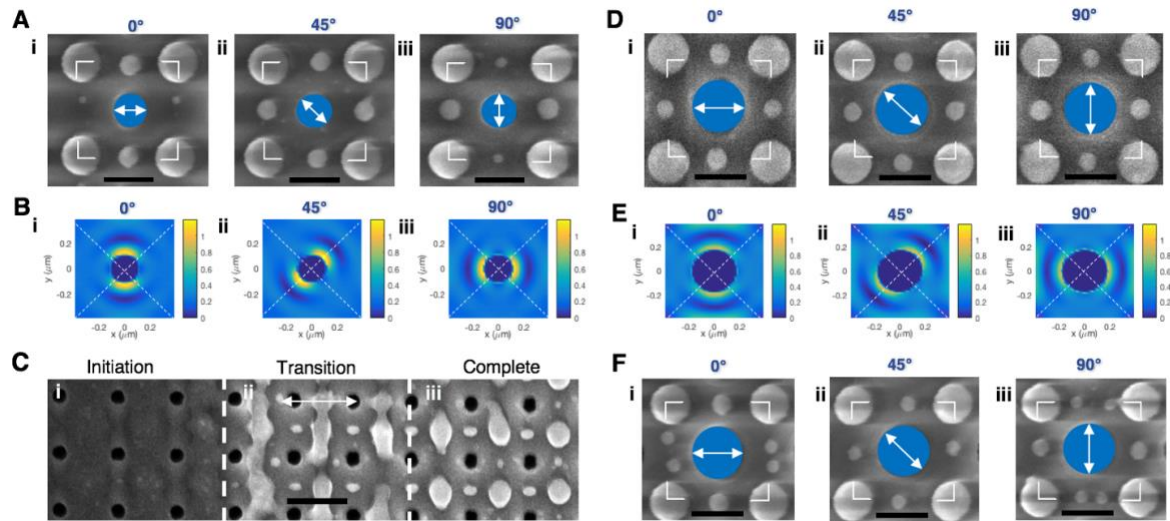
Figure. 3.3. Polarization-dependent near-field absorption and nanoparticle size modulation. (**A, D** and **F**) SEM images of nanoparticle distributions over different polarization angles (i-iii) relative to the horizontal direction with a hole size of 250nm(A) and 400nm with high fluence(D) and low fluence(F). (**B** and **E**) FDTD simulated spatial distribution of absorption cross-section for different polarization angles (i-iii) and hole size of 250nm(A) and 400nm(D). Dashed lines are the boundaries of 4 quadrants and the unit cell in FDTD simulation corresponds to the boxed area in A, D and F. (**C**) 2D assembly pattern with an increased fluence from left to right. Polarization directions are labeled with white arrows. Scale bars are 400nm for A, D and F and 800nm for C respectively. Reproduced with permission from ref [100] Copyright 2019 American Chemical Society.

We observed that the non-homogeneous transient heating, melting and dewetting triggered by near-field absorption should be the origin of the nanoparticle tuning mechanism. Fig.3.3C shows different stages of assembly induced by laser irradiation with fluence near the dewetting threshold. Non-uniform melting is first observed at the initiation stage. The y quadrants melted and dewetted, exposing the substrate between the holes. At the transition stage, it appears that early melting in the y direction introduced by concentrated hotspots led to the formation of S_{PP} particles through direct dewetting. On the other hand, x quadrants melted and merged into a continuous liquid stripe along the y axis. Solidification arrested a Rayleigh-Plateau type of instability[14,107] experienced by the liquid strip. However, at increased fluence this instability developed fully, breaking the stripe into large particles while satellite droplets yielded the so-called S_s particles, which

are similar to those reported in the solidification of liquid metal stripes.[14,108] Our observations highlight the crucial role of the polarization-dependent heating, melting and self-assembly induced by the near-field laser beam energy deposition.

With a given laser wavelength, the variation of hole sizes can define the magnitude of near-field enhancement and therefore tune the size range of nanoparticles. When the size of the hole is increased to 400 nm, the high fluence regime (Fig. 3.3 D) yields a similar pattern to Fig. 3.3 A but the particle size difference between S_P and S_{PP} become much smaller; which is explained by the FDTD simulations, where a reduced near-field enhancement in PP direction was observed in Fig. 3.3E. However, with a slightly lower fluence, we observed the particle in polarization direction is split into 2 dots, whose placement also follows a polarization-dependent pattern (Fig. 3.3F). The formation of 2-dot pattern is also related to laser amplitude, which will be explained in the following section.

To quantitatively analyze near-field enhancement, we define hotspots as the regions whose absorption cross-sections are 2 times or larger than the overall average(Fig. 3.4). The hotspot intensity is defined as the average absorption cross-section over the hotspot area. The normalized intensity difference and the particle volume difference over the x and y directions are given below and plotted. The hotspot intensity is positively correlated with the nanoparticle size increase.

$$Norm. Hotspot\ Intensity. Diff. = \frac{Abs_x - Abs_y}{\frac{1}{2}(Abs_x + Abs_y)} \qquad \text{Eq. 1a}$$

$$Norm. Particle\ Vol. Diff. = \frac{r_x^3 - r_y^3}{\frac{1}{2}(r_x^3 + r_y^3)} \qquad \text{Eq. 1b}$$

B
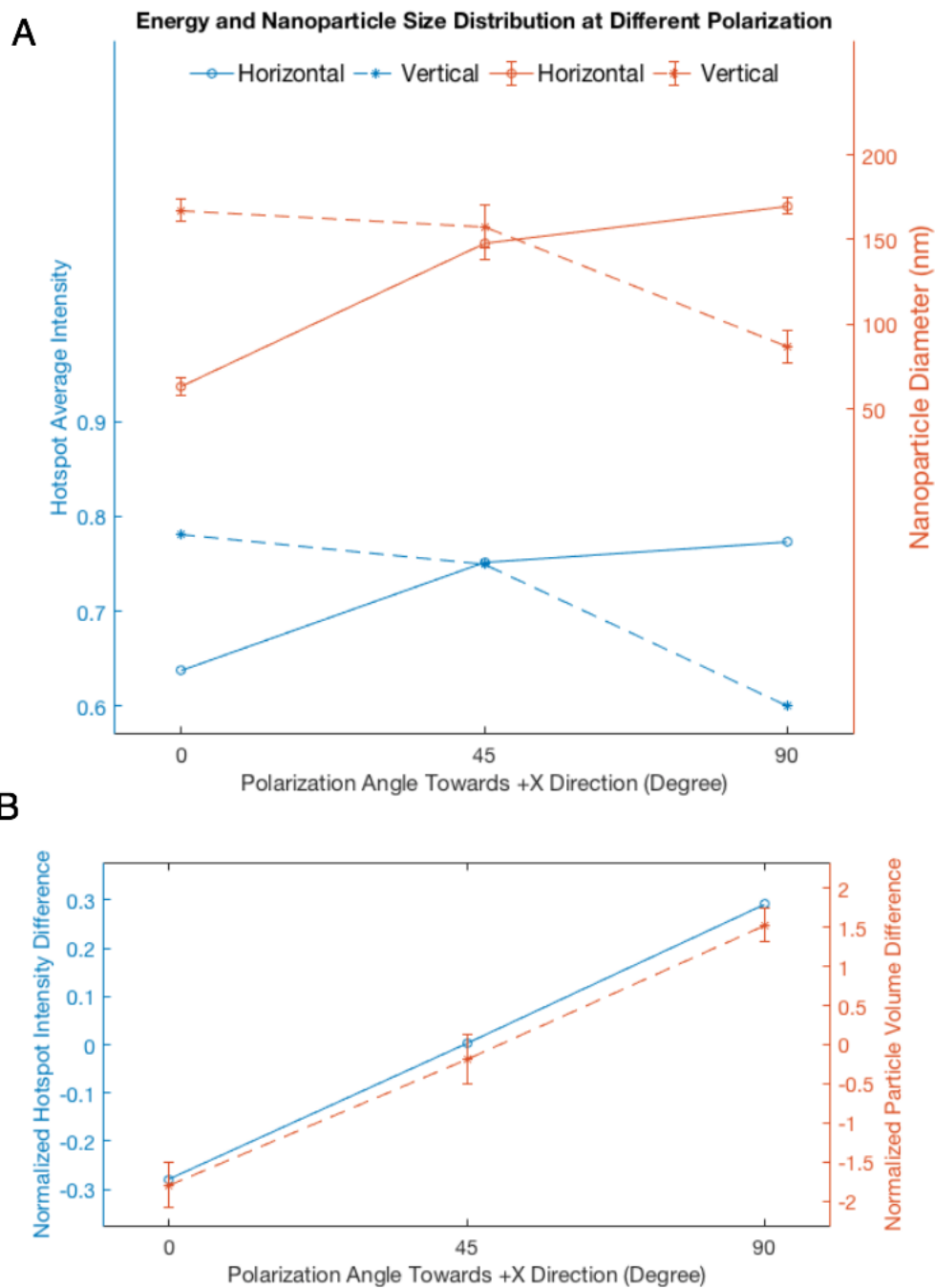
Figure 3.4 Polarization-dependent nanoparticle size distribution and absorption simulation. (**A**) Hotspot average absorption(left) and nanoparticle diameters(right) against polarization in different directions. (**B**). Normalized hotspot intensity difference (left), and particle volume difference(right) in horizontal and vertical directions against polarization. Reproduced with permission from ref 100 Copyright 2019 American Chemical Society.

3.2.3 Amplitude based modulation

The second LiMA mechanism entails the programming of the number of nanoparticles via regulating the laser light amplitude (i.e. fluence). Two distinct regimes are identified for laser fluence below and above the ablation threshold. For laser fluence below the ablation threshold, LiMA offers control of "S" nanoparticle numbers from 0 to 2 in two different directions (Fig. 3.5A). The origin of such variation is based on the spatial absorption distribution and the energy-dependent dewetting state transition. The schematic in B illustrates how these two effects take place. With the increase of absorbed energy, four energy-dependent "S" nanoparticle dewetting states are distinguished, i.e. α, β, γ, and δ. Here, α state indicates dewetting initiation, where only big patch of liquid started dewetting from the quadrant (refer to Fig. 3.5C-Initiation) with no S particle formation. Afterwards, satellite particles are formed, from one small (β state), two small (γ state) to ultimately one large (δ state) S particle. The relative absorbed energy levels of these four states are labeled as dashed lines in Fig. 3.5 B. We then plotted two curves describing the absorbed energy against different locations across the laser-irradiated region in Fig. 3.5 B (lower axis), where different locations on the substrate receive increasing laser fluence from left to right due to the Gaussian laser beam profile. The emergence of α, β, γ, and δ states on the substrate is linked to the absorbed energy curves in Fig. 3.5B through arrows. Since the absorbed energy in the PP direction is higher than in the P direction, the PP line is higher than P line in Fig. 3.5B. As a consequence, we can clearly see on Fig. 3.5B that the transition of states always initiates earlier in the PP direction than in the P direction, which is depicted in Fig. 3.5C. This difference leads to various combinations of particle numbers in two directions. It should be noted that the local laser energy density gradient on Fig. 3.5C is steep, rendering the transition region too short. With shallower imparted energy density gradients, each energy state can occupy a wider region, giving opportunities of forming a symmetrical and uniform assembled region. A series of "S" nanoparticle combinations are obtained by applying loosely focused laser beams and therefore shallower laser energy density gradients are shown in Fig. 3.5A. Combinations of corresponding different states in the PP and P directions are mapped in Fig. 3.5B. It is noteworthy that Fig. 3.5A (ii) demonstrates dewetted states of "S" particles while the development of L particle has not been completed due to the fact energy level of correspondent states are relatively low.
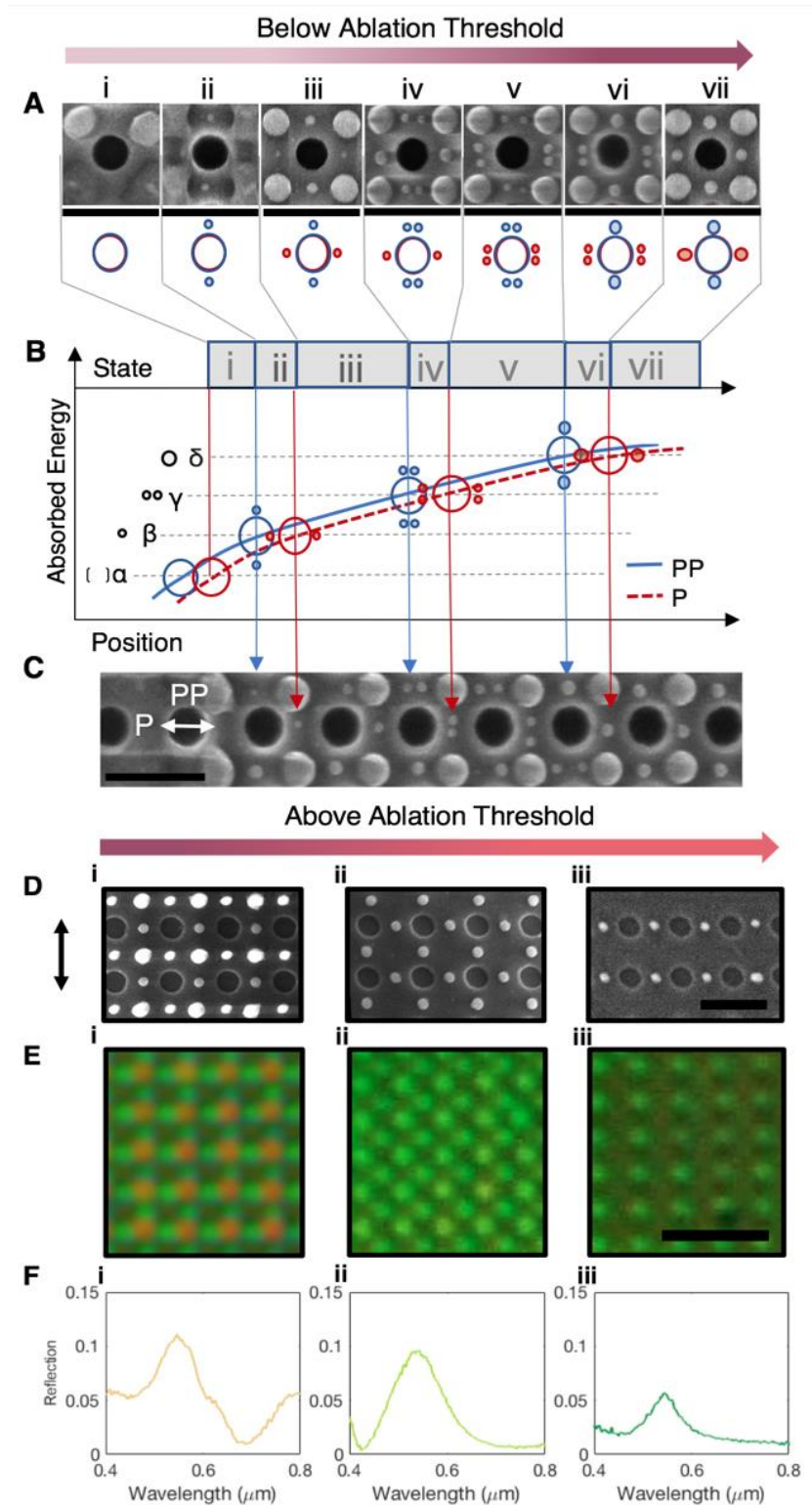
Figure. 3.5. Energy-dependent assembly state transitions and the modulation of nanoparticle number. (**A**) SEM images and schematics of different nanoparticle arrangements irradiated by loosely focused laser pulses of increased fluence on a 400 nm hole patterned a-Si film. Nanoparticles assembled in PP and P directions are marked with

blue and red colors, respectively. (**B**) Schematics of polarization and energy-dependent modulated assembly in PP and P directions. The different assembled nanoparticle combinations are mapped on (**C**) the graph of the absorbed energy vs the position across a spot irradiated by a tightly focused Gaussian laser beam under increasing laser fluence from left to right. Dashed horizontal lines in (**B**) mark different energy levels for assembling S particles into different states (α, β, γ, and δ). Polarization directions in A-C are the same and labeled with a white arrow with reference to the hole. (**D-F**) modulation of "L" and "S" particle numbers above the ablation (i.e. nanoparticle removal) threshold. (**D**) SEM images of three representative arrangements (i-iii) under fluence of 1.5, 1.8 and 2.0 J/cm2 for a 335 nm hole pattern. (**E**) Bright-field optical microscopy corresponding to different arrangements in D. (**F**) Microscopy reflection spectra for the patterns shown in D and E. The scale bars are 1μm for A, C and D, 2 μm for E respectively. Reproduced with permission from ref 100 Copyright 2019 American Chemical Society.

By applying laser fluence above the ablation threshold corresponding to the targeted particles, the number of "L" and "S" nanoparticles can be programmed (Fig.3.5D). The optical response is therefore also configured accordingly (Fig.3.5E and F). High fluence (1.8 J/cm2) subtracts L particles, thereby leaving a square 4-dot S particle array (Fig. 3.5D, ii). An even higher fluence (2.0 J/cm2) will subtract 2 more S particles and generate 2-dot patterns (Fig. 3.5D, iii). The preserved 2 S particles are located in the horizontal direction, which is also the hotspot location. This result revealed further evidence of the process dynamics following the laser-material interaction. The enhanced absorption leads to the dewetting of "S" particle in hotspot locations, after which the formation of "L" particle and "S" particle take place. The particle subtraction mechanism should happen in a later stage as the mass transfer driven by the spatially varying surface tension gradients could possibly provide enough force[51,109,110] to remove the liquid in the colder domains. Microscale reflection spectra were measured (Fig. 3.5F), suggesting a promising application as programmed optical resonator arrays. The detailed resonance analysis will be carried out in section 3.3

3.2.4 Number of pulses

The third LiMA mechanism features selective nanoparticle subtraction based on the polarization and amplitude of 2nd laser pulse irradiation. The method can effectively break the predefined "S" nanoparticle two-side symmetry (Fig. 3.6A, ii-iii), leaving single-side particle placement (Fig. 3.6B, ii-iii and Fig. 3.6C). The selective subtraction based on additional laser pulse is related to near-field enhanced absorption and successive rapid thermal expansion.[111] Different S particle sizes lead to different subtraction mechanisms. From the results of Fig. 3.6A and B, the larger S particles are effectively removed due to size-dependent resonance (Fig. 3.6D, i and iii). However, when the S particles are of similar size (Fig. 3.6C, i), the polarization-dependent near-field enhancement becomes significant (Fig. 3.6D, ii and iv), which was further validated in Fig. 3.6C. At low fluence, only particles in P directions (Fig. 3.6C, ii) are removed, while at higher fluence particles in the PP direction are also removed (Fig.

3.6C, iii). It is also noted the subtraction happens after the assembly process and it is therefore a post-processing based modulation.
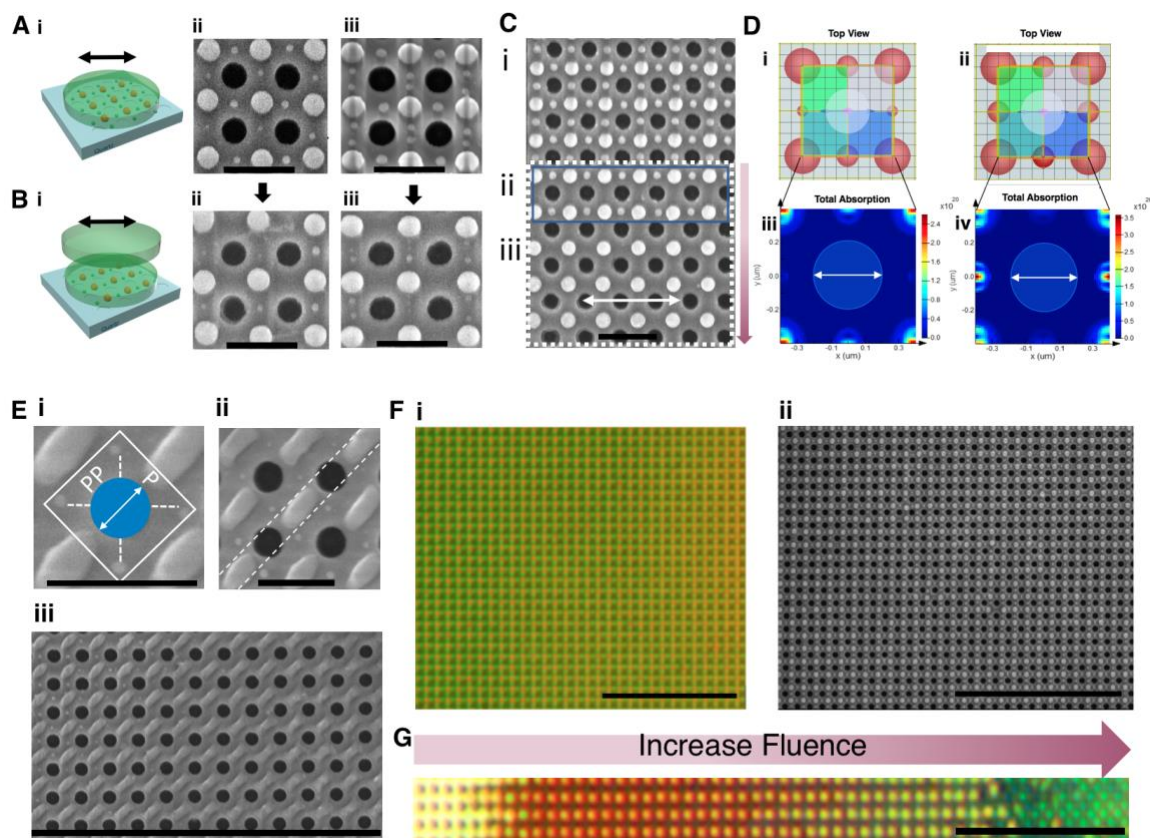
Figure. 3.6. Near-field enhanced selective particle removal and demonstration on the anisotropic shape, scalability and structural color. (**A**) 1st pulse induced dewetting on 400 nm hole pattern. (i) is schematics and (ii, iii) are representative SEM images of dewetted patterns corresponding to Fig. 3A(iii) and (vi). (**B**) 2nd pulse induced selective removal of particles. (i) is schematics and (ii, iii) are the representative SEM images of the pattern after 2nd pulse corresponding to A (ii and iii). (**C**) SEM image of nanoparticle pattern corresponding to Fig. 3A(vii) produced by (i) 1st pulse, (ii) selective (boxed region) removal and (iii) complete removal of "S" particles (dashed region) following 2nd pulse irradiation. (**D**) FDTD simulation explains the laser selective removal of nanoparticles in the patterned array. (i-ii) Top view for simulated geometries for particles of different size (i) and same size (ii), where the unit cells are labeled with boxes. (iii-iv) Absorption profile for (i) and (ii) correspondingly. (**E**) With 45 degree of polarization and low fluence, the L particle is dewetted partially in a controlled way. (i) 45 degree rotated unit cell schematics indicating the quadrants of PP and P. (ii) liquid stripes (dashed regions) are broken by the hole patterns. (iii) large scale controlled anisotropic nanostructure assembly. (**F**) Optical microscopy (i) and SEM(ii) images of large scale dewetted pattern. (**G**) A metasurface with various colors fabricated through 7 ns laser pulse irradiation with 1X objective lens on a 30 nm thick pre-patterned amorphous thin film. The scale bars are 10μm for E(iii), F and G and 1 μm for the rest. Reproduced with permission from ref [100] Copyright 2019 American Chemical Society.

We further demonstrate anisotropic patterning that features elliptical "L" particles and normal "S" particles (Fig. 3.6E). The dewetting mechanism is illustrated in Fig. 3.6E(i) with the PP and P quadrants for a 45° polarization. The PP direction shows an early dewetting feature as it absorbed higher energy, which introduced 4 S particles in 2 PP quadrants. In the P direction, the dewetting lags, forming liquid stripes diagonally between the holes (Fig. 3.6Eii) in a manner analogous to the Fig. 3.3C-Transition. However, since the liquid stripes are separated by the periodic hole array, the delayed dewetting formed ellipsoidal features (Fig. 3.6E, iii). The method shows good scalability, uniformity and potential applications in gradient resonator array and optical structural color surfaces. On the current experimental apparatus, the metasurface fabricated by a single Gaussian laser pulse is ~25 μm in size (Fig. 3.6F, i-ii). A uniform light field induced by flat-top beam profile can be easily applied to fabricate larger-scale patterns. A full visible color spectrum from blue to red is demonstrated with single laser pulse irradiation in Fig. 3.6G by adjusting the laser fluence. The modulation of the nanoparticle combination and crystallinity via the applied laser fluence and the respective variation of the color response will be discussed in the subsequent section. The emergence of nanoparticles in blue and green spectra is achieved in the high fluence regime where L particles has been removed (to the very right of Fig. 3.6G).

3.3 Optical resonance of generated silicon nanoparticle array

For patterns with only "S" particles (Fig. 3.4F(ii) and (iii)), the evident green peaks around 550 nm are the overlapped electric dipole (ED) and magnetic dipole (MD) resonances introduced by the "S" particles. The number of "S" particles can modify the intensity of the optical response without affecting the peak combination and position. For the pattern with both "L" and "S" particles, additional ED and MD features in 800 and 630 nm are introduced by the "L" particles. Similarly, for the case of both "L" and "S" particles, we captured the SEM images describing the "L" nanoparticle size is 220-240 nm. For simulation, 220nm and 20nm overlap are chosen to best describe the measurement. The simulated spectrum is listed in Fig. 3.7.
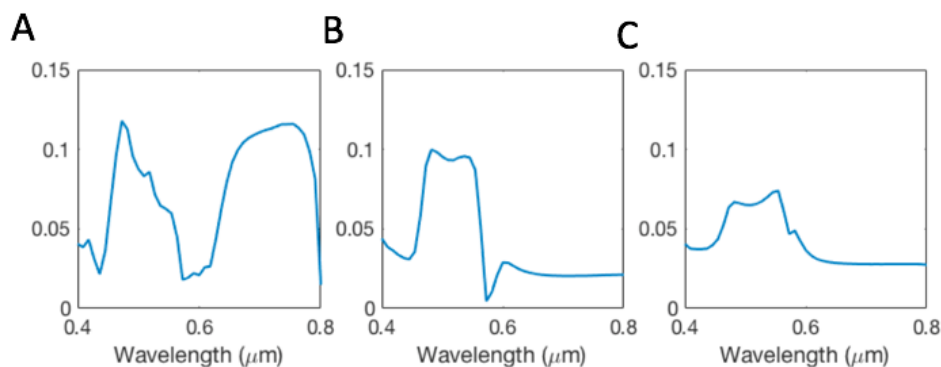
Figure 3.7 FDTD simulated reflection spectra of "L+S", "4-S", "2-S" nanoparticle array. The figures (**A-C**) correspond to Fig. 3.5F. Reproduced with permission from ref [100] Copyright 2019 American Chemical Society.

We utilized the field and vector field to determine and demonstrate the multipolar resonance of "S" particles on the substrates. By comparing with standard dipole and quadrupole plots, we determined the specific modes ED and MD in Fig. 2.3 .

3.4 Nanoparticle dewetting from the microsecond laser irradiation

The existence of the unique light modulated assembly is a combination of the near-field coupling, surface tension driven liquid instability and solidification. We show below in Fig. 3.8 that upon a 10 μs laser pulse irradiation, only L particles are formed in the center of neighboring 4 holes. Therefore this dewetting pattern does not present the Rayleigh-Plateau type of instability. It shows that transient dynamics is highly dependent on the time of the molten state.
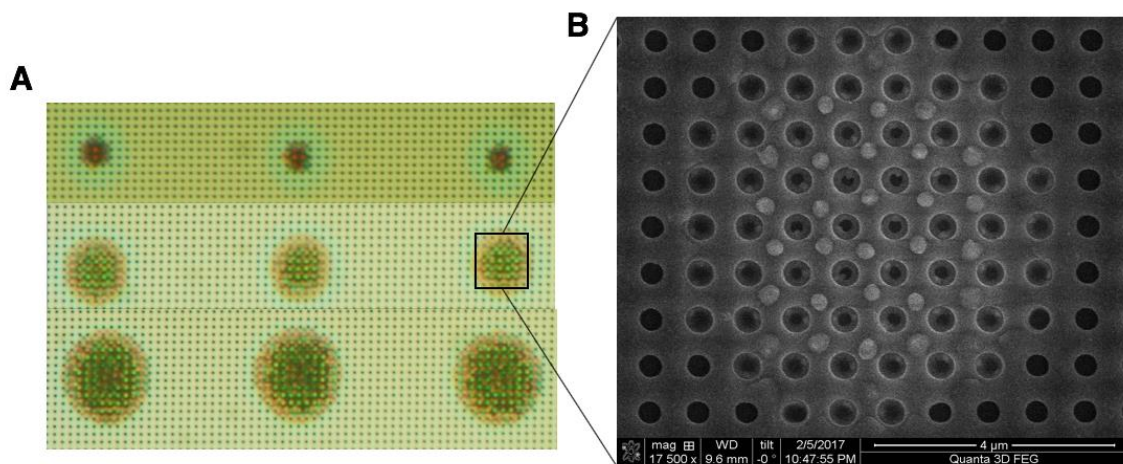
Figure 3.8 Nanoparticle dewetting from 10-microsecond laser irradiation

3.5 Conclusion

In summary, we proposed a laser programming method that can tune nanoparticle arrays' size, number, symmetry and crystallinity. Laser-induced modulated assembly(LiMA) utilizes nanosecond laser pulse irradiation as a source modulating the assembly of a pre-patterned amorphous Si film to a periodic nanoparticle array. The modulation archived polarization-dependent particle size modulation, fluence dependent particle number modulation and selective particle subtraction which all leverage near-field interaction during the process of fabrication. LiMA helps to program the silicon Mie resonator combination as well as the resonance peak position on different scales. Hence, the present laser-based integrated approach offers an effective way for programming dielectric metasurfaces and would be potentially applied in structural color and multi-dimensional optical data storage.

4 Nanosecond pulsed laser-induced crystallization and amorphization

4.1 Introduction

On-demand tuning of the crystallinity of semiconductor materials has long been pursued by material scientists and device engineers. Engineering the crystallinity of silicon has been studied intensively due to its place as the ubiquitous material for electronics, micro-electro-mechanical-system(MEMS), and photonics. Pulsed laser annealing has been the workhorse for the display industry and recently has been employed to improve the channel quality inside 3D memory devices[3]. In parallel to crystallization, amorphous silicon has also been widely used in photonics[60,112] and MEMS[113]. Femtosecond surface amorphization has been proposed for post-fabrication tuning silicon resonator frequencies[114]. Hence direct control of crystallization and amorphization of silicon nanostructures will offer an additional degree of freedom for device manufacturing and active modulation. Furthermore, fast and reversible phase transformation could enable silicon as a new phase change material (PCM) for visible photonics. The detailed motivations have been mentioned in section 1.1.2 and 1.2.3.

Despite all anticipated benefits, silicon has never been considered as a phase change material. Pulsed laser crystallization can be realized on thin film[115] and nanostructure[92]. Pulsed laser-induced amorphization has also been reported on bulk materials[116] and thin films[117]. Hence pulsed laser irradiation is a promising route for reversible phase change in silicon nanodomain. Previous research studied crystallization [118]and amorphization[117] in thin films at different configurations and laser pulses. For device applications, reversible phase transformation on the same nanostructure and preferably with the same modulation source is required. Hence, proper selection of the domain size as well as the laser pulse duration becomes critical in order to achieve the preferred quench rate range. On the other hand, as we observed in a previous study[100], laser melting may lead to the dewetting of silicon nanostructures just like metal and GST[100]. Suppression of dewetting during reversible phase transformation, thereby preserving the consistency of the optical properties remains a critical issue.

To tackle these challenges, several fundamental questions must be answered. For fast crystallization, super-lateral growth is a mechanism proposed by Im *et al*. [118]. While we probed its existence in thin films [115,119], it has not been observed on the silicon nanostructures. Via *in situ* TEM[92] observation during laser annealing of nanoscale precursors, we found that crystallization in fully melted domains is dominated by the strong stochastic dependence of nucleation. Therefore, it remains unknown how to introduce crystallization deterministically. Furthermore, the amorphization is far less well studied. It was first reported that the skin layer of a bulk silicon wafer amorphized upon picosecond pulsed laser heating[120]. Complete amorphization of a thin silicon film capped with an oxide layer has been reported, and the parametric study of the amorphization through different substrate temperatures indicated a nucleation based mechanism, although *in situ* evidence was provided. On the other hand, the femtosecond laser-induced surface amorphization has been probed *in situ* with a total time of 600 ps, indicating a nucleation-free process[121]. The quench rate has been identified as the main driving force determining the amorphization mechanism. Our recent work[100] shows

nanosecond laser pulses can introduce order-to-disorder one-way transformation on silicon nanostructures. Femtosecond laser quenching of the surface layer of bulk wafer reached a rate of 10^{12}K/s, and nanosecond laser heating on a thin film reached 10^{10}K/s. In contrast, nanosecond laser irradiation on a nanostructure could reach 10^{11}K/s[100]. Since silicon nanodomain has one order higher quench rate than the thin-film, *in situ* investigation becomes critical for distinguishing nucleation events. Silicon nanoresonator possesses a unique Mie resonance, hence providing a unique optical signature that is not available for the thin silicon films.

Here, we answer the above questions by showing that reversible phase transformation can indeed be realized on silicon nanostructures with the same nanosecond pulsed laser. We confirm a unique geometric pinning effect of isolated silicon nanostructures enabling deformation-free reversible phase change on various geometries. Transient optical reflection probing reveals the mechanisms and key criteria for ultrafast amorphization and crystallization. The temporal time scale is measured to be below 100 nanoseconds and the reversible cycle count can be extended to 400. Ultimately, we demonstrate single pixel-addressable active optical metasurfaces for applications in structural color displays and dynamic wavefront control.

4.2 Reversible phase transformation

In Fig. 4.1A we introduce the concept of laser-induced reversible phase transformation of Si nanostructures. a-Si, c-Si and l-Si stand for amorphous, polycrystalline and liquid silicon. We term the a-Si to c-Si phase transformation as "forward phase transformation", while c-Si to a-Si as "backward". The phase transformation process consists of melting and subsequent solidification. The terms "crystallization" and "amorphization" refer to specifically two distinct solidification processes instead of the whole phase transformations. The crystallization in forward transformation can be induced by either nanosecond or continuous wave(CW) laser. The CW laser scanning at mm/s speed essentially applies ms pulses and the irradiated amorphous silicon undergoes either solid phase or nucleation based crystallization[122], resulting in a large laser power window. Hence it is used for large area crystallization in all the figures. On the other hand, the low energy nanosecond laser pulses can introduce super-lateral growth[123] in thin films, which could provide faster crystallization speed. We experimentally probed and validated the same crystallization effect in nanodisks, which will be discussed later. For amorphization, it is known femtosecond laser pulses can introduce amorphization on bulk silicon[121]. Here we found nanosecond laser pulses are short enough to introduce amorphization in nanoscale silicon domains. The studied samples in the present work are 30nm thick arrays of amorphous Si (a-Si) nanodisks and nanoribbons on fused silica, whose characteristic lengths range from 200 to 1500nm. The fabrication processes can be found in section 2.6. The as-fabricated amorphous silicon sample's Raman spectrum is listed in Fig. 4.1E as "pristine" .
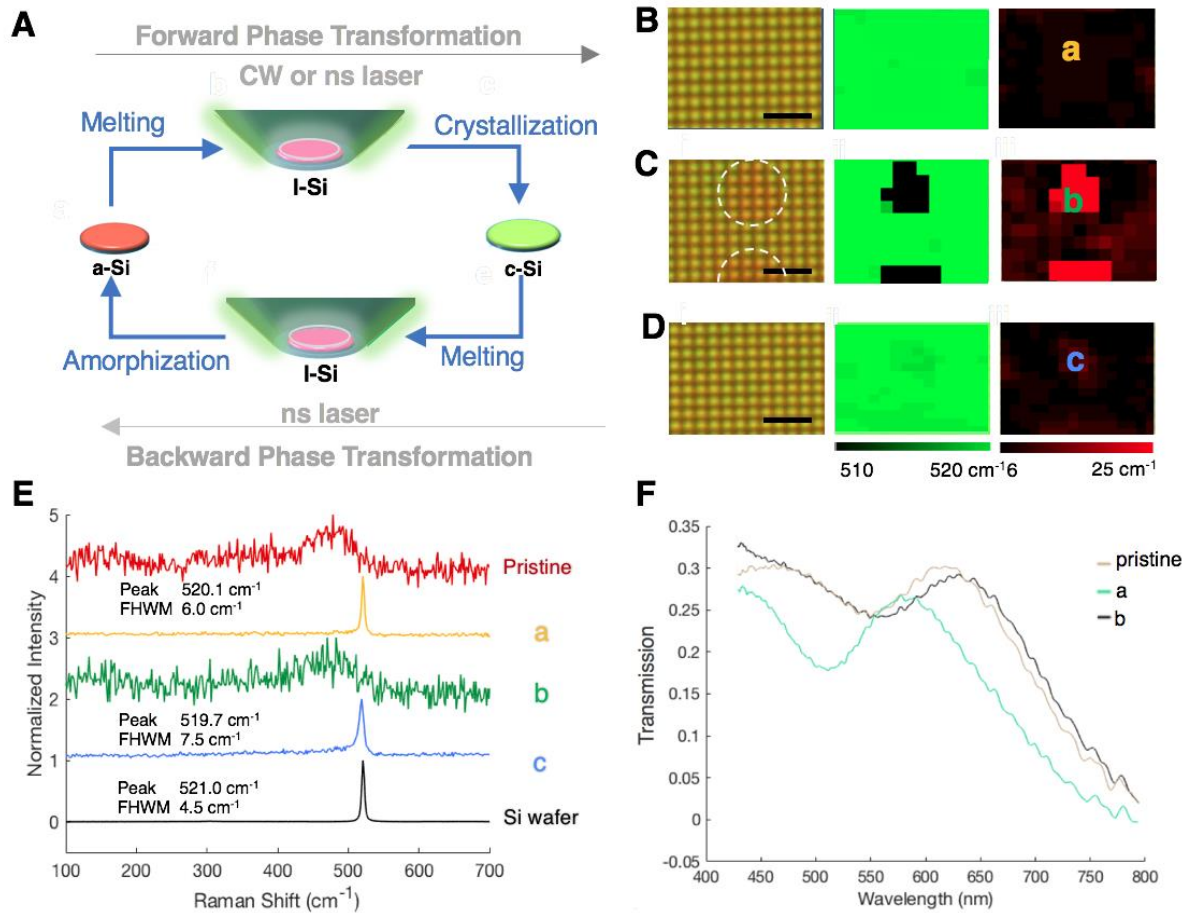
Figure 4.1 Schematics and experimental validation of reversible phase transformation of silicon nanostructures. (**A**) Schematics of reversible phase transformations. (**B**) 215nm diameter a-Si fully crystallized by CW laser into c-Si nanodisks and characterized with bright field optical image, mapping of Raman peak position and peak width(from left to right). (**C**) The c-Si disks in B are locally amorphized by two nanosecond laser pulses, (**D**) Amorphized nanodisks in C are "erased" with CW laser-induced crystallization. (**E**) Raman spectra of the labeled regions in B-C as well as pristine amorphous nanodisks and the single-crystal silicon wafer. (**F**) Transmission spectra of pristine a-Si disks and disks in regions a, b. The scale bars for B-D are 2 μm.

In Fig. 4.1B, the CW laser irradiation has crystallized nanodisks of 215nm in diameter into poly-crystalline states as indicated by the Raman spectrum "A" in Fig. 4.1E. The Raman peak mapping shows the whole laser processed area has the peak position close to 520 cm-1 and the width close to 6 cm-1. Silicon nanodisks with sizes smaller than 500nm fall into the Mie resonance regime124, presenting vibrant visible colors in bright-field and dark-field optical microscopy. The poly-crystalline nanodisks with 215nm diameter present a green resonating color(Fig. 4.1B). As we can see in Fig. 4.1C region b, c-Si nanodisks switched the resonance color from green to red upon irradiation of a 13 ns laser pulse. Those nanodisks share a "low density

amorphous"(LDA) broad Raman peak at 480 cm$_{-1}$(Fig. 4.1E), identical to the pristine amorphous phase. Given the well-studied correlation between the silicon's crystallinity and its Raman spectrum, we confirm the silicon phase changed from crystalline state to amorphous state. The phase transformed region can be identified through both bright field optical imaging and Raman mapping (Fig. 4.1C). In Fig. 1F, the transmission measurement of the laser-induced forward(a) and backward phase transformation(b) can blue-shift and red-shift the Mie resonance, finally returning its scattering spectrum close to that of the pristine amorphous phase. The change of optical resonances is properly captured with FDTD simulations using refractive indexes from literature[125,126]. In Fig. 4.1D, additional CW laser crystallization resets the crystallinity and photonic resonance (region c), indicating the initiation of the next phase change cycle.

We further found the use of a single nanosecond pulsed laser can obtain reversible phase transformation. From Fig. 4.2A, we confirm the nanosecond laser can induce forward phase change on a canvas of amorphous disks under a fluence of 1.8 J/cm$_2$. Backward transformation by a fluence of 2.1 J/cm$_2$ is shown in Fig. 4.2B. In the Raman peak mapping, we can clearly see the matching with the transformed optical image. With a higher fluence compared to Fig. 4.2A (1.9 J/cm$_2$), a-Si disks were transformed to a-Si in the center and to c-Si at the rim (Fig. 4. 2C) within the laser processed area. We term the a-Si to a-Si transformation as a "neutral phase transformation". Fig. 4.2C shows the fluence for crystallization is lower than that of neutral transformation, which evinces crystallization at near-complete melting. Hence, energy variation controls the solidification path to either crystallization or amorphization. The neutral transformation requires lower energy compared to the backward transformation since amorphous silicon has a lower melting point and thermal diffusivity.
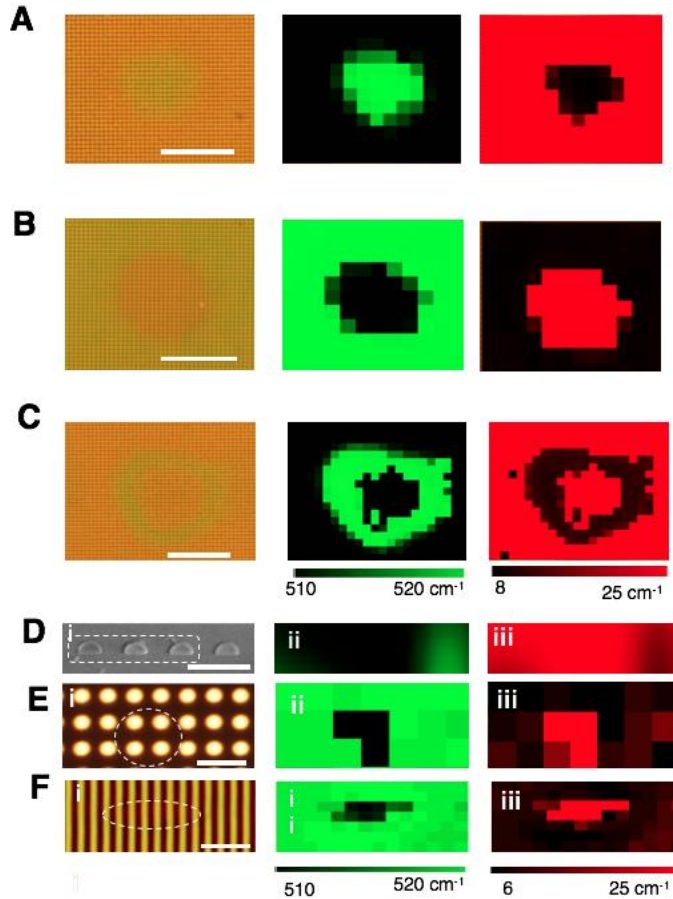
Figure 4.2 Nanosecond laser-induced reversible phase transformation. (**A**) forward (a-Si to c-Si) (**B**) backward(c-Si to a-Si,) and(**C**) neutral(a-Si to a-Si) phase transformations. Left to right are the bright-field image, Raman shift peak position and peak width mapping. For figure C, additional crystallization happens at the rim of the laser-irradiated area due to the low fluence. The color black in Raman peak position indicates the peak position is smaller than the lower bound, 510 cm-1 while in Raman peak width mapping, it means the width larger than the upper bound, 25 cm-1. The scale bars for A-C are 10 μm. (**D**) The 40nm thick asymmetric (half-circular) single crystal nanodisks exhibit pinning effects after amorphization. (i-iii) SEM image, Raman mapping of peak position and width. (**E**) The amorphization of 30nm thick crystalline nanodisks of 1.5μm diameter. (i-iii) bright field image and associated Raman mapping of peak position and width. (**F**) Location-selective amorphization of 500nm wide nanoribbons. The laser-irradiated area in (C-E) are labeled with dashed lines. The scale bars are 500nm for D and 4 μm for E-F.

Besides the geometry pining, the amorphization is also found robust and versatile. Raman mapping confirms the amorphization of the single crystalline silicon sample in Fig.4.2 D prepared using the method in the literature56 . Over 2 μm size nanodisks can be fully amorphized in Fig. 4.2 E. Furthermore, location-selective amorphization within one nanoribbon is achieved (Fig. 4.2F). We infer the amorphization is deterministic across different initial crystallinities and lateral geometries regardless of whether the domain

fully melts in the lateral dimension. The results are in agreement with the theoretical analysis where "complete amorphization" will deterministically happen at a critical quench rate of $6.65 \times 10_{10}$K/s[87].

4.3 Dewetting and its suppression

When the incident laser fluence is larger than the threshold level, the molten silicon nanodisk will experience dewetting. When a 28ns laser pulse incident on a group of nanodisks, we can see partial and fully dewetting happening at different regions in Fig. 4.3 A(ii). Based on this observation, we proposed the schematics of the dewetting happening on the nanodisks. Later we found for shorter pulse duration(13ns), the partial dewetting effect is not evident.
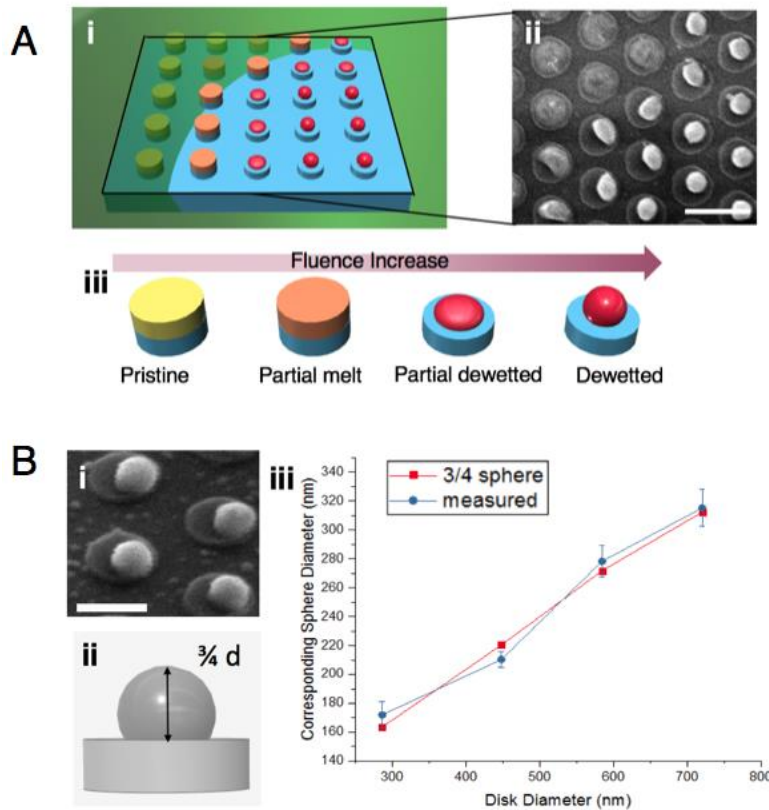
Figure 4.3 Characterization of dewetting in the molten silicon nanodisks. (**A**) Nanodisk irradiated with different laser fluences. (i)Schematics of nanodisks array irradiated with a Gaussian laser pulse. (ii) SEM image of laser irradiated nanodisk array corresponds to (i). (iii) Different states of laser-heated nanodisk. (**B**) Shape characterization of the dewetted nanoparticle. (i) Tilted SEM image of dewetted nanoparticles. (ii) Modeling of the shape and height of nanoparticles. (iii) Comparison of modeled nanoparticle size and SEM measurements.

Upon 13 ns laser heating, a unique geometry pinning effect enables high fidelity reversible transformations which are not found in GST[45] or previous studies[100]. Fig. 4.4 A shows a collection of the polycrystalline disks, amorphized disks and dewetted disks

from left to right. Both dewetted disks and amorphized disks show amorphous features in the Raman mapping. As we can see in Fig. 4.4 B, in contrast to the dewetted nanodots, the morphology and shape of the amorphized nanodisks remain almost identical to crystalline nanodisks. A slight edge rounding observed in nanodisks proximal to the dewetted dots. Fig 4.4 C further shows amorphized disks beyond this vicinity do not present such rounding.
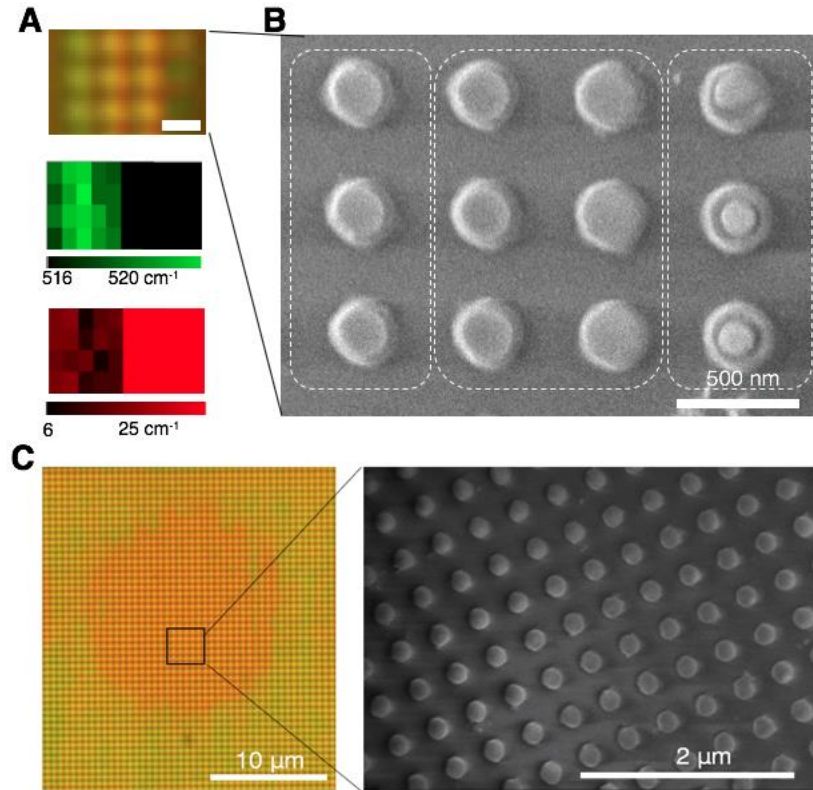
Figure 4.4 Characterization of geometry pinning effect. (**A**) Geometry pinning on a 220nm nanodisk array characterized by the optical image and Raman mapping of peak position and width(from top to bottom). The bright-field image contains a crystalline nanodisk (light green), amorphized nanodisk (orange) and dewetted disks (deep green). (**B**) Scanning electron microscopy(SEM) image for a, with white dashed lines labeling the aforementioned three regions. Scale bars are 500nm for A-B. (**C**) The geometry pinning effect on a large group of amorphized nanodisks

Different from the 28ns case, the dewetting suppression in 13ns case is considered thermodynamics dominated. If the dewetting in the current study is kinetically dominated as in laser-induced metal dewetting[109,127] or the case in 28ns irradiation, different input energies should result in gradual deformation rather than a clear distinction between dewetting and non-dewetting. Therefore, we infer the observed pinning effect is controlled by thermodynamics instead of kinetics. From the thermodynamic point of view, as silicon's work of adhesion is three times that of gold[128], its free energy reduction during dewetting is anticipated to be only one third. The smaller free energy reduction requires a higher energy input to overcome the energy barrier to initiate deformation, thus

leading to higher threshold fluence for dewetting. Below we provide geometry specific thermodynamic analysis.
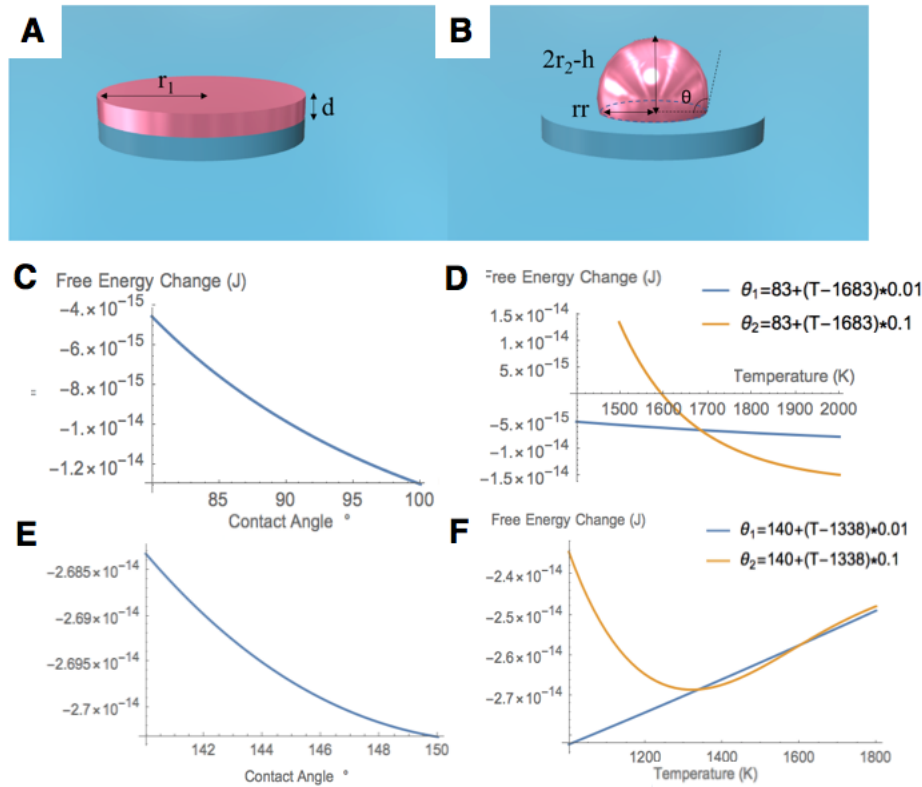
Figure 4.5 Thermodynamic analysis for the dewetting process. (**A-B**)The schematics of the molten silicon geometries (A)before and (B)after dewetting. (**C-D**)The free energy change after dewetting plotted against different contact angle and temperature for silicon . (**E-F**) same plots as (C-D)for gold.

a.   The volume conservation of the molten silicon

For nanodisk before dewetting(Fig. 4.5A), d is the thickness of the disk, and r_1 is the radius. Therefore the volume of the disk is $V_1 = \pi d r_1^2$.

The geometry of the dewetted dot is measured to be hemispherical. The lost height is defined as h. From the equilibrium contact angle θ, h is estimated as $h = r_2(1 + \cos[\theta])$. Then the volume of the dewetted dot is derived as:

$$V_2 = \frac{4\pi r_2^3}{3} - \pi h^2 \left(r_2 - \frac{h}{3} \right)$$

Through volume conservation, we can solve $V_1 = V_2$ to obtain:

$$r_2 = \frac{3^{1/3} d^{1/3} r_1^{2/3}}{(2 - 3\cos[\theta] + \cos[\theta]^3)^{1/3}}$$

b.   The surface area before and after dewetting

The liquid-gas interface area for a disk: $\qquad\qquad\qquad A_{l1} = 2d\pi r_1 + \pi r_1^2;$

The area of a spherical cap: $\qquad\qquad\qquad\qquad\qquad Asc = 2\pi h r_2;$

The liquid-gas interface area for a dewetted dot: $\qquad A_{l2} = 4\pi r_2^2 - Asc;$

The liquid-solid interface area for a disk: $A_{ls1} = \pi r_1^2$;

The radius of the contact area: $rr = \sqrt{r_2^2 - h^2}$;

The liquid-solid interface area for a dewetted dot: $A_{ls2} = \pi rr^2$;

The solid-gas interface area for a disk: $A_{s1} = 0$;

The solid-gas interface area for a dewetted dot: $A_{s2} = \pi(r_1^2 - rr^2)$;

c. Interfacial force balance (Young-Laplace equation)
$$\gamma_s = \gamma_{sl} + \gamma_l * \cos\theta$$

d. The free energy change after dewetting
$$\Delta G = \gamma_s * (A_{s2} - A_{s1}) + \gamma_{sl} * (A_{ls2} - A_{ls1}) + \gamma_l * (A_{l2} - A_{l1})\square$$

Substitute the Young-Laplace equation into above:

$$\Delta G = \frac{\pi r_1 \gamma_l}{(2 - 3\cos[\theta] + \cos[\theta]^3)^{2/3}} \left(-2d(2 - 3\cos[\theta] + \cos[\theta]^3)^{2/3} + \frac{1}{4} 3^{2/3} d^{2/3}(12 \right.$$
$$- 5\cos[\theta] + 4\cos[2\theta] + \cos[3\theta])r_1^{1/3}$$
$$\left. - \frac{(8 - 9\cos[\theta] + \cos[3\theta])^{2/3}\sin[\frac{\theta}{2}]^2 r_1}{2^{1/3}} \right)$$

e. Plot the free energy vs. different contact angle

The contact angle is measured to be close to 90 degrees. Observations showed that higher temperature gives a higher contact angle (85-95degree). Surface tension has a linear relation with temperature.

Therefore, we substitute in the geometrical parameter, r_1=100nm and d=30nm. We found ΔG is negatively correlated to the contact angle. The free energy reduction at the melting point is calculated as $-8.2 \times 10^{-15} J$.

f. Free energy vs. temperature

If a linear estimation of the contact angle is made:
$$\theta = (83 + (T - 1683) * k) \text{ Degree};$$

And we also substitute in the linearly temperature-dependent surface tension.
$$\gamma_l = (730 - 0.13 * (T - 1683)) mN/m;$$

From the listed k values, ΔG has the possibility to become positive at supercooled states. However, there is no valid experimental data describing the temperature-dependent contact angle of molten silicon on silica. Therefore we consider the free energy reduction to be still negative, which indicates that dewetting is a spontaneous process. Further, the free energy reduction is enlarged with an increase of the temperature, which entails the cause of dewetting under high laser fluence input.

Further, we can compare the results of silicon to the counterparts in plasmonics, gold. Liquid Au has a temperature-dependent surface tension as follows:
$$\gamma_l = (1138 - 0.19 * (T - 1338)) mN/m;$$

Its equilibrium contact angle with silica at its melting point is 140 degrees. As no temperature-dependent contact angle data is available, we estimated it to be similar to the variation in silicon. The free energy change against contact angle and temperature in Fig. 4.5 E-F has shown that the gold has a free energy reduction of $-2.68 \times 10^{-14} J$ at melting point, which is three times that for silicon($-8.2 \times 10^{-15} J$). This shows that Au

has a larger thermodynamic driving force for dewetting. Furthermore, if we put Au's contact angle and silicon's surface tension into equations, a $-1.8 \times 10^{-14} J$ free energy reduction is predicted, indicating that both surface tension and contact angle has an effect on the dewetting free-energy reduction.

4.4 Reflection probing of phase transformations

Due to the strong Mie resonance of silicon nanodisks, reflective probing of phase transformation can be used for monitoring the heating, melting, solidification, dewetting and cooling of the silicon nanodisk. The detailed schematics of the setup can be found in Appendix A4.

4.4.1 Single nanodisk probing

To investigate the detailed mechanisms of reversible phase transformations, we carried out transient reflection probing on a single nanodisk. In this experiment, the 633nm probing CW laser and the 532nm pump nanosecond laser are aligned collinearly and tightly focused on a single nanoresonator. The diffraction limited focus is verified through the modification of a single disk in Fig 4.6.
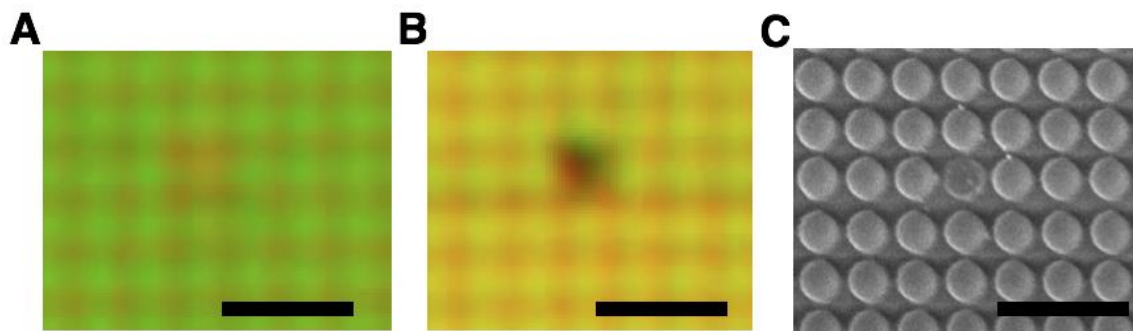
Figure 4.6 Minimum laser addressable feature size and periodicity. (**A**) 200nm diameter crystalline nanodisk array(green) with a 400nm period with single-pixel amorphized in the middle(red). (**B**) 300nm nanodisk array in a 400nm period with the single-pixel ablated in the middle. (**C**) The SEM image of the (**B**).

The laser phase transformation process will go through heating, melting, solidification and cooling, which is schematically shown in Fig. 4.7B. We would like to note a significant phase-dependent thermo-optical effect at 633nm probe wavelength (Fig. 4.7C). Specifically, the amorphous nanodisks offer reduced reflection (-15%) of probe beam upon pump laser irradiation and the crystalline ones present opposite effect (22%). Both thermal and carrier effects induced by optical excitation can modify the refractive index[129]. We observe the reflection decay in Fig. 4.7 C-D is much slower than the typical carrier decay (1ns) [130] but follows well the predicted temperature transient. Studies indicated the inverted position of the isentropic band gaps from c-Si and a-Si lead to positive and negative temperature coefficients (dn/dT)[131] in 633nm.
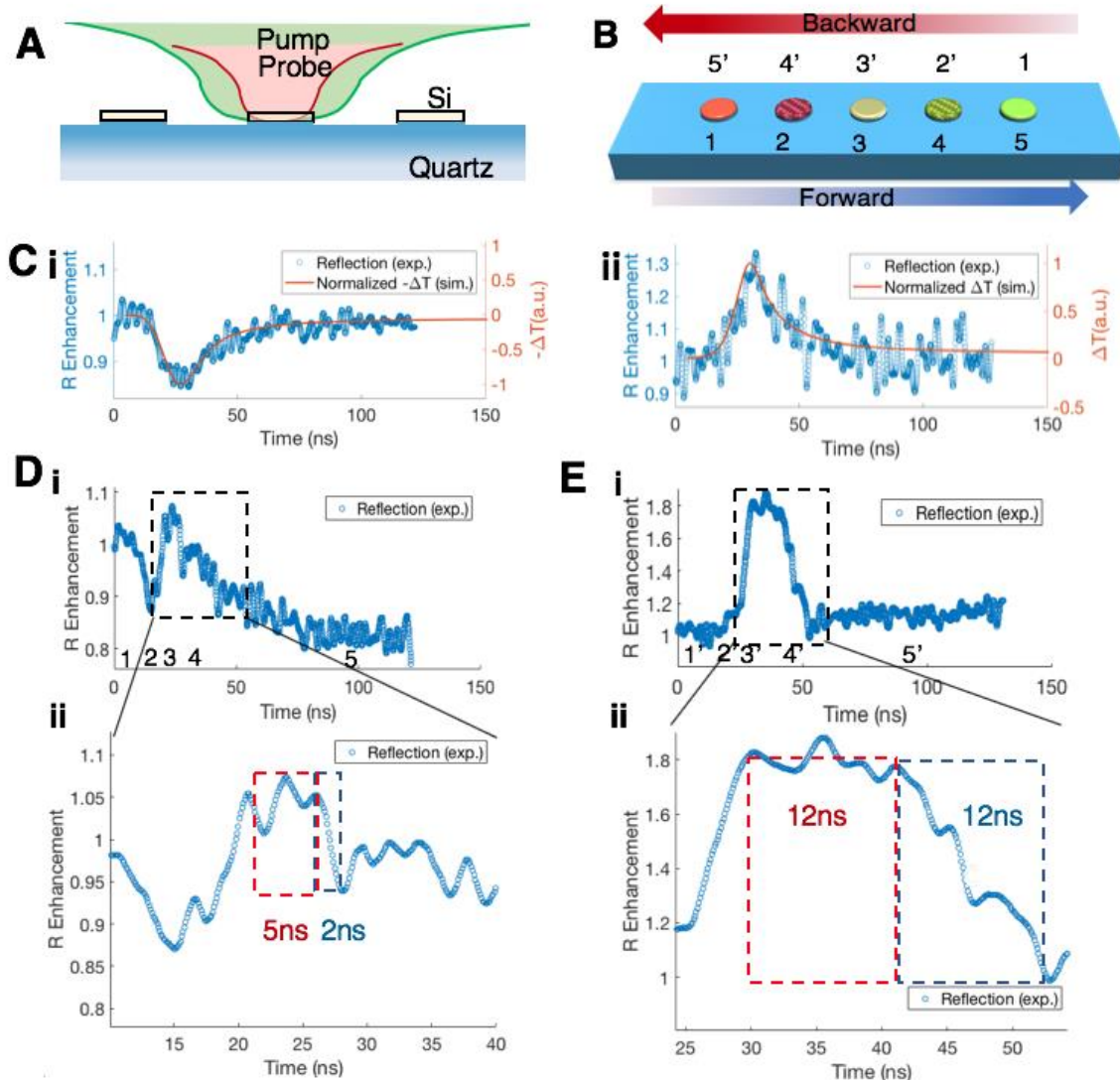
Figure 4.7 Probing of single nanodisk's reversible phase change. (**A**) Schematics of the single nanodisk optical reflection probing. The 532nm 13ns pulsed laser is used as a pump laser and the 633nm CW HeNe laser is used as a probing laser.(**B**) Schematics of transient states during laser phase transformation of the disk. Labels 1-5 (or reversely 5'-1') are a-Si, heated a-Si, liquid-Si, heated c-Si, c-Si. (**C**) The crystallinity dependent thermo-optical signals upon the irradiation of a 13 nanosecond laser pulse (i) on a-Si disks and (ii) on c-Si disks. The simulated temperature change has been normalized to the $(T_{max}-T_{min})$. Note that in B the sign is flipped for the comparison of the signals. (**D**) Probed transient reflection of the forward phase transformation(a-Si to c-Si). (**E**) Transient reflection of backward phase transformation (c-Si to a-Si). In the zoomed-in view (ii), the red dashed region indicates a molten state while the blue region indicates the solidification. The plotted reflection curves in B-E are all normalized to the signal level of initial reflectivity.

In Figure 4.7B, the numbers 1-5 and 5'-1' (the reverse process) stand for the amorphous, the heated amorphous, the liquid silicon, the heated crystalline and crystalline nanodisks. The transient processes can be categorized into heating (1->2),

melting (2->3), molten state and solidification (3->4) and cooling (4->5) period based on the aforementioned states. The heating and cooling are signified with phase-dependent thermo-optical effects. The initial drop and increase of the reflection signal in Figs. 4.7D and 3E, respectively, are the effect of heating (1->2) in amorphous and crystalline nanodisks. At the cooling process (4->5), the trend is however switched due to the change of crystallinity. The melting is characterized through an increased reflectivity based on High-Density Liquid phase[132]. This is in agreement with reported investigations, including e.g. our own experiments on the excimer laser annealing of thin Si films[115]. The existence of melting is further confirmed through increasing the laser fluence to dewetting (chap.). FDTD simulation is also provided in Fig. 4.11 validating the high reflective state can be offered from liquid silicon's refractive indices.

Much shorter melt duration and solidification time are observed for crystallization compared to amorphization. The time interval (3->4) can be further separated into the molten state (τ_{melt}) and the solidification period ($\tau_{solidify}$) by the on-set of solidification, which is the drop of the reflection signal. The experimental τ_{melt} is defined as the time duration when the acquired reflectance, R, is at its maximum. Following the melt duration, the experimental $\tau_{solidify}$ is defined by the duration from the time reflection starts to decrease until stage 4. Note that this drop shall be distinguished from the drop caused by cooling in crystalline nanodisks (Fig. 4.7Cii). A 2ns crystallization time is much shorter than 12ns amorphization time. The corresponding melt duration is also much shorter in crystallization.

Upon examining Fig. 4.7C, we infer that the 2ns-long fast crystallization is driven by super-lateral growth[123], where near-complete melting preserved some solid seed remnants for the regrowth of the crystal. The elimination of the spontaneous nucleation process leads to the short melt duration and the solidification time is based on the crystal growth speed of silicon, which is reported to be in the range of 10-18 m/s[133]. On the other hand, the 12ns long amorphization follows the deep undercooling of the liquid. The absence of nucleation sites on the non-participating interface with the substrate allows deep undercooling wherein the liquid silicon transforms into amorphous material through glass formation. This experimental observation in conjunction with our simulation results agree with the arguments presented by Kim *et al.*[117] Details of the heat transfer and phase transformation simulation are presented in next section. Our transient signal, however, cannot differentiate the contributions from nucleation and liquid-amorphous transformation. Our probing experiments in thin films[115] indicate that the nucleation will not trigger significant optical contrast. As the reflection drops continuously without any step change, at least we confirm glass transformation spans the whole 12ns. The 12ns and estimated 950K temperature supports the postulated silicon relaxation time map by McMillian at 2004[134].

4.4.2 Comprehensive heat transfer and phase transformation simulation
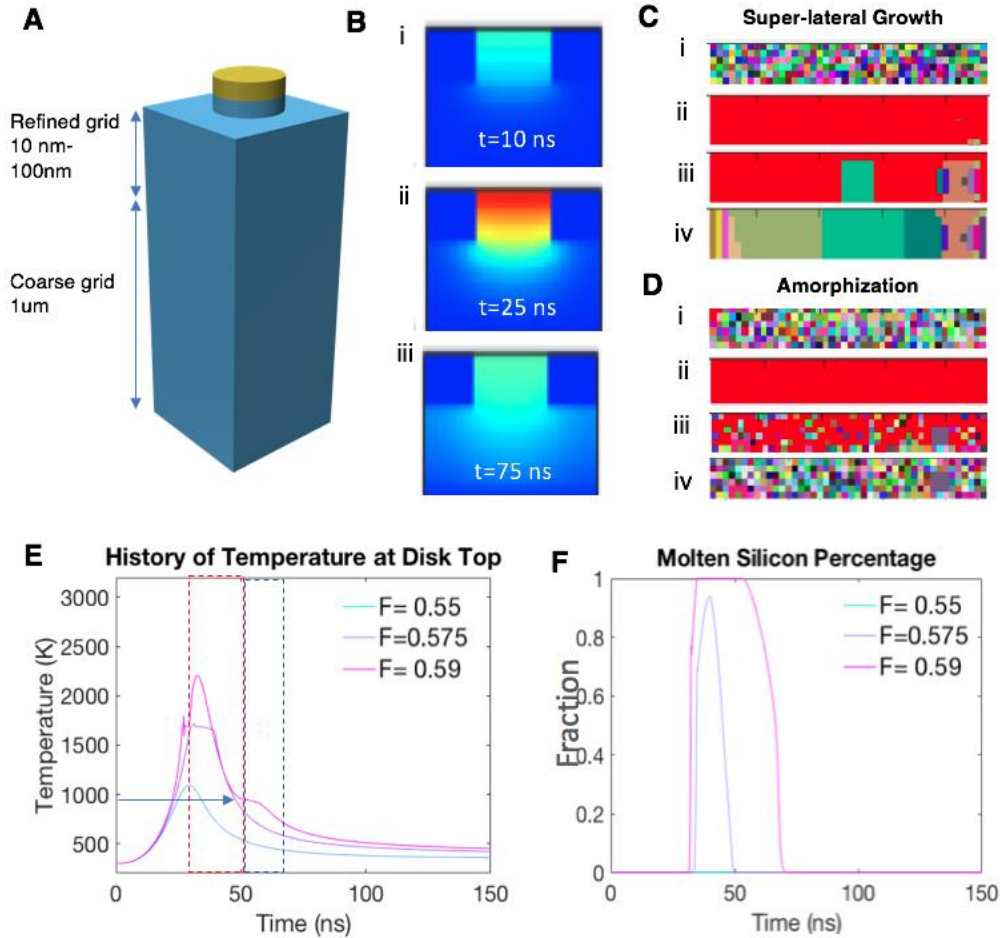
Figure 4.8 Comprehensive simulation to explain the transient reflectivity signals. (**A**) Schematics of simulated nanodisk sitting on the oxide mesa and the fused silica substrate. (**B**) Simulated transient temperature distribution at the top of the simulated domain with high fluence F=0.575 J/cm2. (**C**) Crystal map showing the process of super-lateral growth with red color stands for molten silicon and random colors stand for the nanocrystals. Initial nanocrystals are an artifact from setting up the simulation, which is explained below. (**D**) Crystal map showing the process of nucleation based amorphization. Colored crystals at (iii)-(iv) stand for the nuclei. (**E**) The temperature involution of the simulated heating(F=0.55 J/cm2), crystallization(F=0.575 J/cm2) and amorphization(F=0.59 J/cm2) under different laser fluences. Here the arrow labels the deep under-cooling that amorphization reached. The red and blue dashed boxes are indicating the melt duration and solidification process during the amorphization processes. (**F**) temporal evolution of the liquid silicon volume fraction during the heating, crystallization and amorphization processes.

Augmenting the description provided in the methods section, we show here a schematic of the modeled geometry in Figure 4.8 A. The substrate features gradient grid sizes to suffice the stability requirement. Then we show a characteristic temperature mapping during the laser heating process. As seen in Fig. 4.8 B-ii and iii, the nanodisk dissipates heat to the substrate in a 3D fashion, different from the thin film cases, which

explains the elevated quenching rate. The heat transfer simulation has been verified by comparing the transient thermo-optical signal as discussed in the main text.

Then we show the simulated melting, nucleation and crystal growth for crystallization and amorphization. The result is best described by displaying the snapshots of the crystal map during the processes (Fig. 4.8C). Molten silicon is labeled as red color in the snapshots. For crystallization, the simulation captured the growth from residual unmelt seeds at the silicon-oxide interface (Fig. 4.8A), illustrating the super-lateral growth and the nucleation-free fast dynamics. Note that the snapshot shown is 2D while the whole domain is 3D, suggesting the possibility of crystal growth from out-of-plane seeds. The source of residual crystal seeds[135] is the heterogeneous nucleation on oxide during the deposition of amorphous films. As it is impossible to reproduce the random existence of small seed crystals at the silicon oxide interface in the simulation, we assumed a polycrystalline domain as an artificial initial condition. After laser energy is fully delivered, only the bottom region of the initial crystals may survive melting (Fig. 4.8Cii), resembling the true physical scenario. For amorphization, full melting and liquid overheating are required to sustain undercooled liquid silicon. Consequently, nucleation events at an exponentially increased rate took place at D(iii) due to the deep supercooling reached. Ultimately, the liquid silicon surrounding nuclei transformed into amorphous silicon, which is not displayed in figure 4.8D(iv). Note that crystals on the map indicate the locations of the nuclei and the phase is amorphous.

Furthermore, we show the detailed curves of temperature evolution and volume fraction change of the liquid silicon. Since there is no crystal growth, the temperature of the molten silicon kept decreasing and reached deep supercooling (700K) that triggered amorphization. The predicted melt duration of around 12ns matched measured data (Fig. Fig. 4.8E and Fig. 4.7Eii). The generation of nuclei is estimated to happen around 12ns, which also agrees with the solidification time in Fig. 4.7E. The glass transformation of surrounding liquid silicon to the amorphous phase has not been modeled separately due to insufficient theoretical analysis. As indicated from the curves of F=0.575 J/cm2, the melt and solidification time sum up to 10ns, which is slightly longer than the observation (7ns). This is simply because the experimentally observed melting did not reach the predicted volume fraction (93%), and therefore the melting and crystallization could take a shorter time.

4.4.3 Energy dependent laser-material interaction

With the increase of incident laser energy, the laser-nanodisk interaction vary significantly(Fig. 4.9). For low power, a thermos-optical effect exist, which will be explained in detail in the following section. Then the melting initiated and the maximum reflectivity will increase with laser fluence. It is because the number of nanodisks that experience melting and the extent of each nanodisk melt are both increased. Then at a fluence of 2.1 J/cm2, the reflectivity plateaus due to the fact that the temperature increase does not increase the molten state's reflectivity, which is widely observed during the laser crystallization of the thin films[115]. Since full melting is introduced, we observed the amorphization in the solidification processes, which echos with the previous signals.

Then we found the laser-induced dewetting slightly reduces reflectivity compared to amorphization. Under high laser fluence, once melting is completed, dewetting kinetics takes place quickly just as in the case of molten metal droplets predicted by simulation[51]. The reflectivity of a dewetted molten nanoparticle is smaller than that of a molten nanodisk due to high scattering. Therefore, the initiation of dewetting will reduce the reflectivity. Detailed analysis of dewetting is beyond the scope of this paper. In summary, the above figure shows the increasing, plateauing and the dropping of the maximum reflectivity. These effects, especially the plateau feature, are only consistent with the existence of melting.
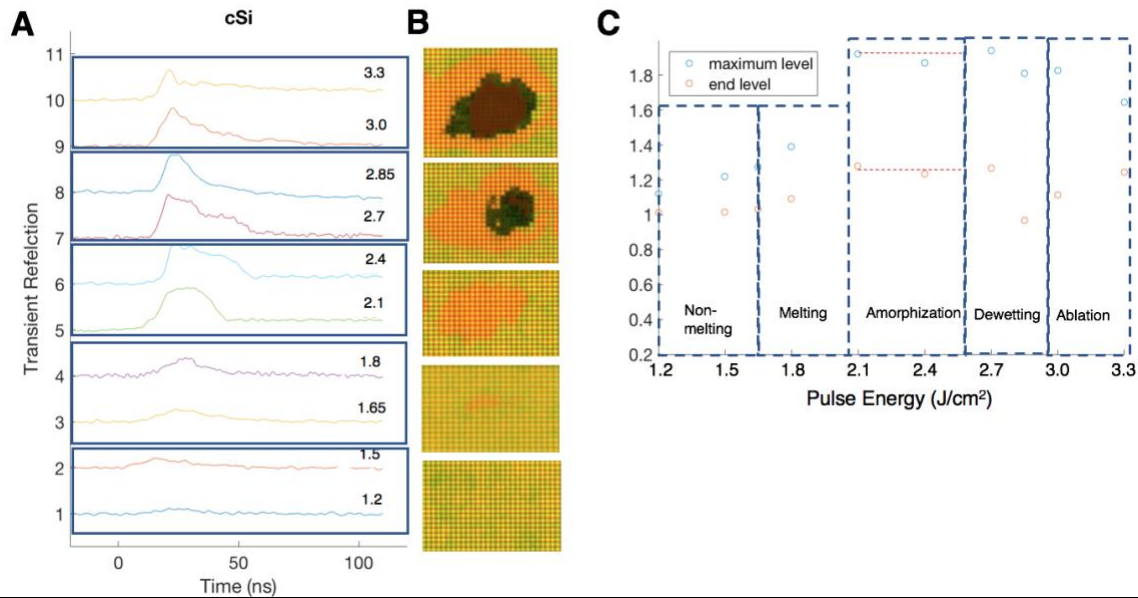
Figure 4.9 Energy-dependent laser-material interaction. (**A**) Transient reflection signal with increasing laser fluence. The boxes are grouping the signals for different physics happing during the transient processes, which are correlated to the images in b and the categories in c. (**B**) The corresponding image of the laser processed area. The scale bar is 10 μm. (**C**) The statistics of the measured signal against laser pulse energy. The blue dots are the maximum signal value along the whole process and normalized to the initial level to account for the HeNe probe laser fluctuation. The red dots are for the end level. The blue dashed lines between different laser energy level is categorizing the existing physics based on the signals we obtained. The red dash line are showing the plateau of the maximum signal, indicating the molten silicon's reflectivity is saturated.

4.5 Applications to active photonics
4.5.1 Highly repeatable cycling
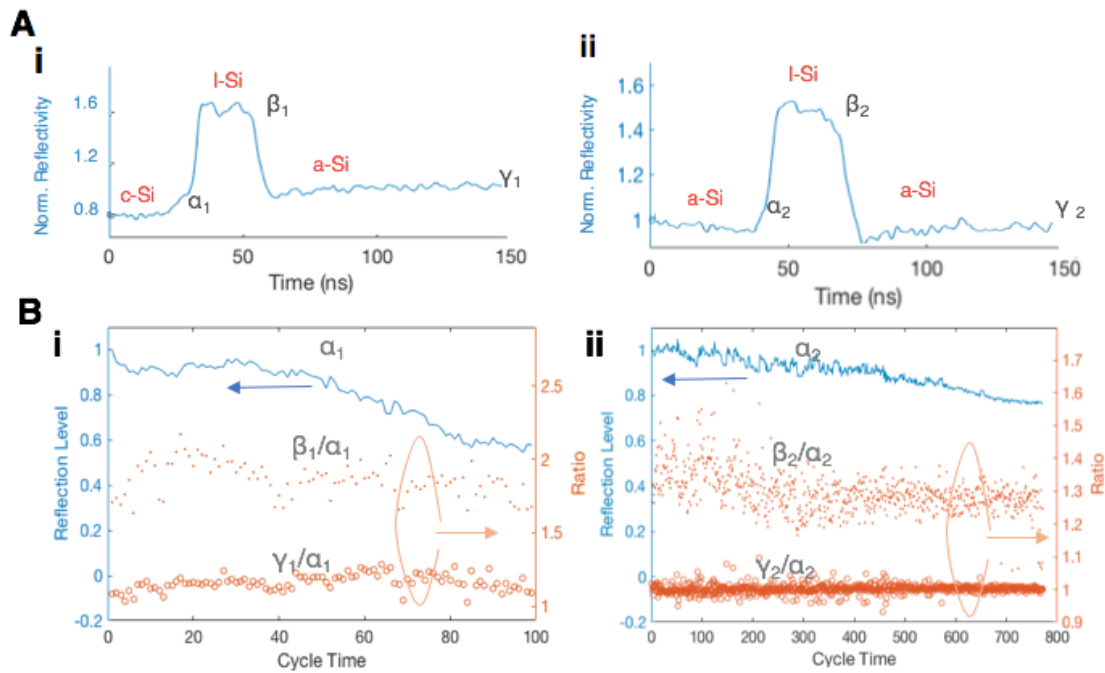
Figure 4.10 Characterization of high repeatable cycle lifetime. (**A**) Probed reflection signal from a group of nanodisks experiencing backward (i, c-Si to a-Si) and neutral phase transformations (ii, a-Si to a-Si). (**B**) Repeatable cycle lifetime of 210 nm diameter bare resonators with backward and neutral phase transformations signals from A. For reversible phase transformation in (i), additional CW laser scanning is applied to ensure crystallization. For repeated amorphization in (ii), a train of nanosecond pulses is applied. The reversible cycle lifetime is characterized through recording the signal's initial, peak and ending levels, termed as α, β, γ. The subscript 1 denotes the amorphization process and subscript 2 denotes the neutral process during consecutive phase transformations.

High speed, high contrast and highly repeatable switching behavior are observed. Both the forward and backward phase transformations conclude within 100ns, including the heating, melting, solidification and cooling processes. Consequently, the reversible switching frequency reaches 5MHz, which is comparable to industry start-of-the-art[136]. Due to the Mie resonance, 200nm crystalline state (c-Si) nanodisk is 80% of the amorphous phase (a-Si), resulting in a 20% non-volatile modulation (Fig. 4.10A). The order of magnitude matches with the FDTD simulation in the next section. The reflectivity contrast is consistent in both the forward and backward transformation measurements, providing additional evidence of reversibility for the transformation. The initial reflectance (α) is selected as the performance indicator for evaluating the lifetime of the resonator. For complete reversible phase transformations, CW laser scanning is applied to ensure more uniform quality of crystallization than nanosecond laser pulses. The nanodisks yield 50 cycles with only 10% degradation in α (0.5dB) but fully dewet after 80 cycles (Fig. 4.10B, i). Besides the reversible phase changes, we probed the lifetime of repeated neutral (a-Si to a-Si) transformations (Fig. 4.10 B, ii). It shows that the disks withstand ~400 such cycles with only 10% degradation in α (0.5dB) but fully

dewet after 700 cycles. In Fig. 4.10 B, β/α equals to 2 (or 1.3 depending on the initial crystallinity) ensures the resonators passed the melting threshold. The ratio γ/α describes the direction of phase transformation, i.e. backward (>1) or neutral (=1) phase transformation. Note that if high optical contrast is not intended, degradation and deformation can be fully suppressed with additional capping layers.

4.5.2 Phase dependent resonances

The optical resonances of the nanodisks will be shifted due to the change of refractive indices. Limited by the available experimental techniques, the refractive indexes are not measured for the nanodisks. Instead, refractive indices of crystalline[125] and amorphous silicon [126] from the literature have been used in the FDTD simulation in Fig. 4.11. For different states of 215nm sized nanodisks, the measurement and FDTD simulation agree well on the relative magnitude (Fig. 4.11B). From the comparison of Fig. 4.11C and E, the simulated reflection spectra also precisely capture the multipolar resonances in the nanodisks. The above two agreement confirmed the reasonable approximation between the actual refractive indexes and the literature. We further reproduced the CIE colors based on the microscope light source and simulated reflection spectrum, giving identical colors matching the bright-field and dark-field images(Fig. 4.12 B-C).
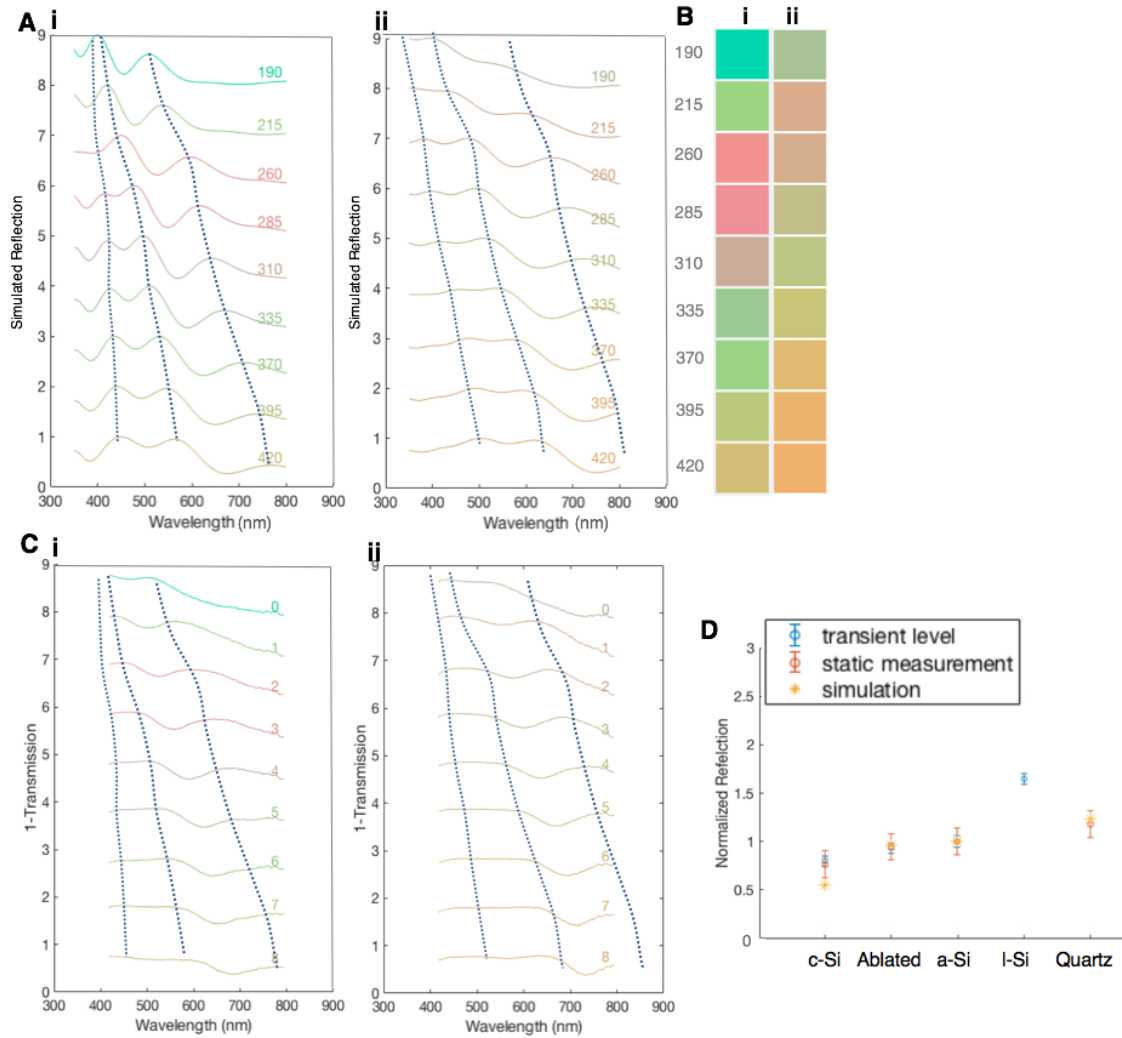
Figure 4.11 Phase-dependent refractive indices and resonances. (**A**) FDTD simulated reflection spectra of crystalline (i) and amorphous (ii) nanodisks with different diameters. The diameters (unit: nm). (**B**) CIE Standard color transformed from simulated reflection spectra from A(i-ii) respectively. (**C**) Measured (1-Transmission) spectra for crystalline (i) and amorphous(ii) nanodisks plotted as (B). The dashed lines in fig A and C are for the visual guidance of peak shifting. The scale is multiplied with 2.5 to show the peaks. (**D**) FDTD simulated reflection levels of silicon under different phases. The ablated state stands for the bare oxide mesa. Note that the static measurement is not available for liquid silicon, which is only transiently melted during laser irradiation.

4.5.3 Pixel-addressable display

Based on the reversible resonance shift, we demonstrate pixel-level active modulation on visible photonic arrays. The optical resonances of silicon nanostructures span broad visible spectra (Fig. 4.12 A-C), leading to wide color palettes[124]. Upon amorphization, the refractive index in the visible range is reduced and induces redshifts of multipolar resonances (Fig.4.12 A and Fig. 4.11). Enabled by a high N.A. objective

lens, we show the reversible encoding of digital information at selected pixels on 700nm pitched nanoresonator arrays (Fig. 4.12 D), which is the first demonstration of near-diffraction-limit pixel-level active modulation of a photonic array. With high-resolution patterning and resonating printing [137], the minimum optical addressable resolution is further reduced to 400nm per pixel (Fig. 4.6), paving the way to pixel-rewritable metasurfaces working at wavelengths below 800nm. Corresponding to the concept of plasmonic displays[26], we show high-resolution dielectric display of "LTL" letters (Fig. 4.12 E), which offers a display resolution up to 63,500 PPI, two orders of magnitude higher than today's mainstream electronic displays. As a proof-of-concept experiment, we further demonstrate a dynamic dielectric display showing text "LTL" transitioning to "CAL" (Fig. 4.12 F). Despite that only 0.5 Hz refresh rate is obtained on a motion stage, a high refresh rate display can be achieved through laser scanning digital light projection (DLP) or a spatial light modulator (SLM) [138].
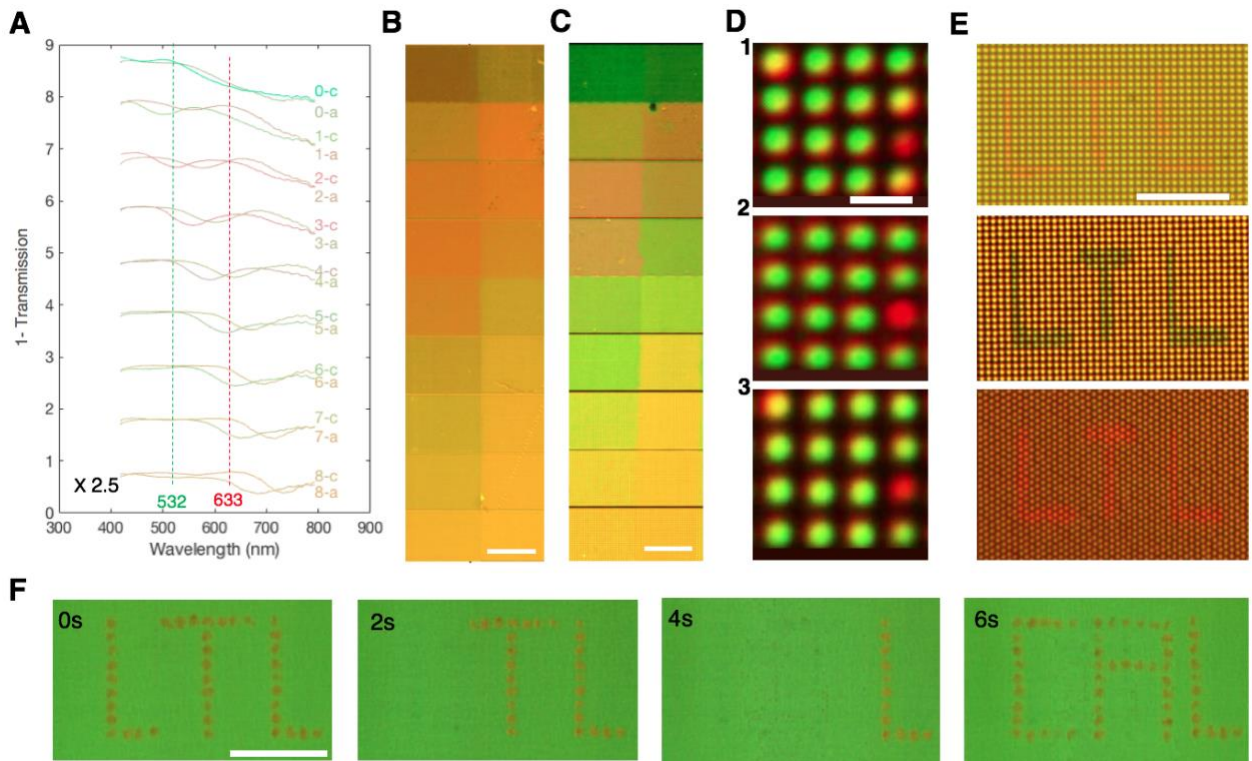
Figure 4.12 Phase-dependent resonance shift, pixel-addressable active modulation and a dielectric display. (**A**) The optical transmission spectra of the nanodisk arrays with different sizes and crystallinity. The diameters for the number "0" to"8" nanodisks are 190nm, 215nm, 260nm, 285nm, 310nm, 335nm, 370nm, 395nm, and 420nm respectively. The crystalline and amorphous phases are labeled as (-c) and (-a). The signal is multiplied by 2.5 and stacked for better visualization. (**B-C**) The optical (B)bright-field and (C)dark-field images of the crystalline (left) and amorphous (right) nanodisk arrays, with diameters ranged from number "0" to"8" from top to bottom. (**D**) 2D diffraction-limited pixel-addressable encoding. The 4-by-4 crystalline nanodisk array is originally resonating green color, and red dot (3,4) is a dewetted disk for reference. First, amorphization turns disk (1,1), (2,4) and (4,4) into yellow color. Then the

crystallization erases dot (1,1), (2,4) and (4,4) into green color. Lastly, re-amorphization addressed the same disk (1,1) again. (**E**) Diffraction limited laser printing of "LTL" letters on different amorphous disk arrays, whose diameter/pitch are 310nm/700nm, 335nm/750nm, 285nm/650 nm (hcp) array, from top to bottom. (**F**) A dynamic color display is showing the characters' transition from "LTL" to "CAL." The scale bars for B-F are 20 μm, 20 μm, 1 μm, 8 μm, and 20 μm.

4.5.4 Visible active metasurfaces

Lastly, we show a the proof-of-concept experiment of an active optical element in the visible wavelength. On the exact place, amplitude-based Fresnel Zone Plates (FZPs) are actively printed with different focal lengths (Fig. 4.13 A-C). The measured cross-section intensity distribution clearly showed the FZP's focal spot has shifted from 200 μm to 350 μm with a slight deviation from designed values (240 μm and 400 μm). The deviation is likely due to the printing pixel limitation and imperfect fabrication[138]. The laser printed FZPs achieved a diffraction-limited ($\lambda/2NA$, $\lambda=633nm$, $NA=100/2f=0.21$), full-width at the half-maximum focal spot of about 1.5 μm (Fig. 4.13D-E). Setups and characterization of the focal plane are described in Appendix A4.
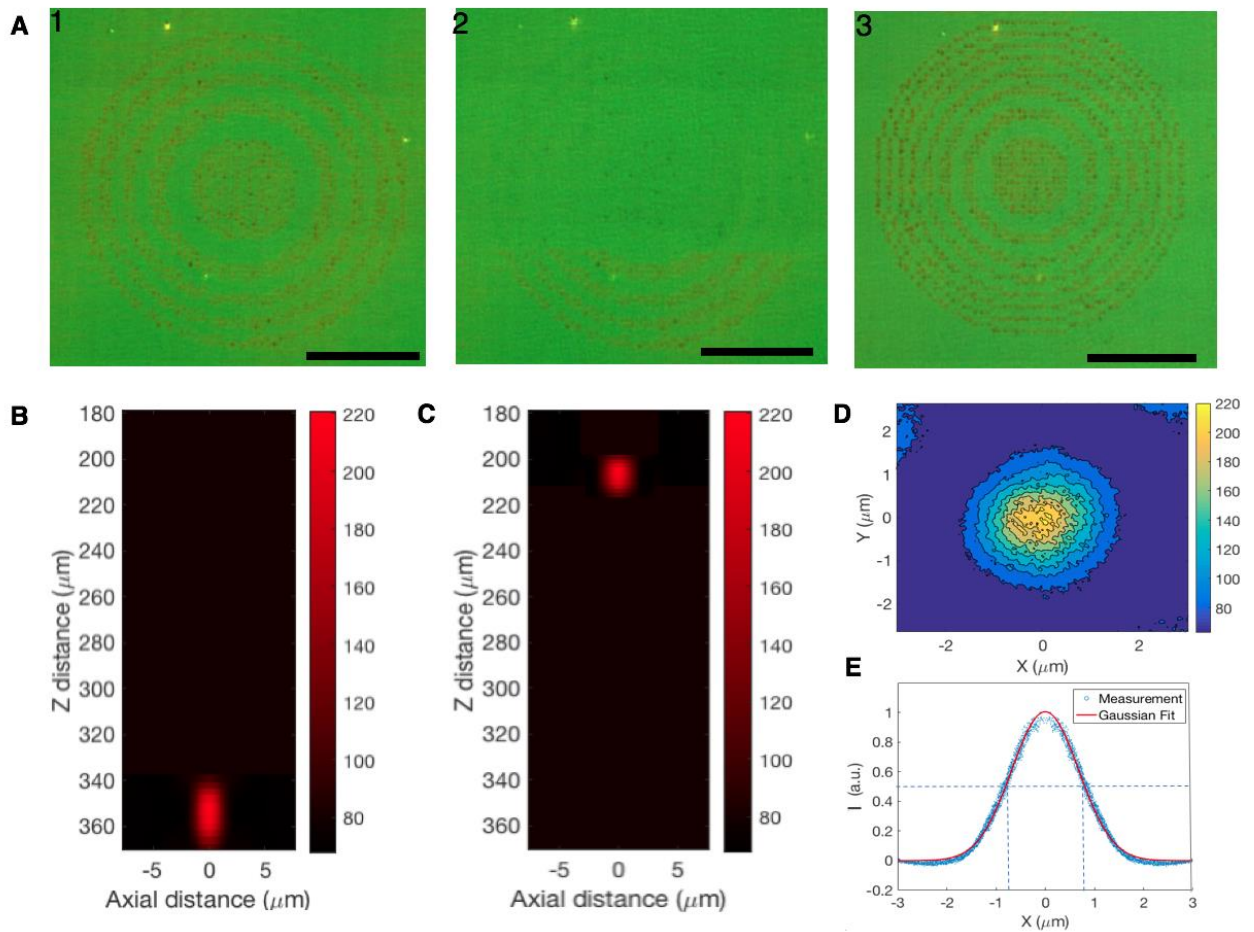
Figure 4.13 Active visible Fresnel zone plates with the on-demand tuning of focal lengths. (**A**) Dark-field images of (1) writing f=400 μm, (2) erasing and (3) rewriting f=240 μm FZPs on the same canvas and location. The scale bar is 30μm. (**B-C**) Measured spatial intensity distribution near focal planes of printed FZPs from A. The actual focal length is measured to be 353 μm and 207 μm respectively. The higher orders are not shown in the plot. (**D**) The focal spot of 1_{st} FZP characterized with CCD intensity image. (**E**)The line plot of radially accumulated intensity and Gaussian curve fitting.

4.6 Discussion and future work

Reversible phase transformation of silicon nanodomains is obtained upon the irradiation of nanosecond laser pulses. The thermophysical properties of silicon suppress the dewetting in nanoscale and keep the geometry intact upon phase transformations. Such a geometry pinning effect eliminates the need for capping layers and therefore preserves the maximum optical contrast between the resonator and air. Transient reflection probing validated the mechanisms of near-complete melting induced crystallization and full melting induced amorphization. The experimental results confirmed the crystal structural change indicated by Raman spectroscopy is indeed a derivative of phase transformations and within the classical thermal regime. The

complete non-volatile modulation concludes within 100ns while solidifications only take less than 20ns. The geometry pining and ultra-short transformation time paved the way for the reversible phase change silicon for active photonic applications. As a proof-of-concept, we demonstrate the pixel addressable active modulation on silicon resonator arrays with 400nm minimum spatial resolution. Based on the reversible resonance shift, we further demonstrate the high-resolution dynamic displays and active visible wavefront control. The wavefront control demonstration differs from the previous reports[29] in that it is based on individual resonators, works at visible wavelengths, and can be easily cycled multiple times. If the light field is delivered through SLM, such components can be arbitrarily written [138] and printed at a nanosecond time scale. Besides the optical wavefront control, rewritable metasurfaces can also be readily applied to holography and encryption[139]. Beyond the resonance shift, silicon has crystallinity dependent thermo-optical and non-linear properties[140], which are intriguing for implementing active tuning functionalities.

Besides active photonics, the site-selective amorphization shown in Fig. 4.2 could enable laser tuning of the optical properties for the manufacturing of silicon photonics. More manufacturing applications can be investigated for silicon photonics and MEMS. Reports have indicated Ge, GaP and GaAs share similar potential as phase change materials upon ultrafast laser irradiation[141], which further extends the material and crystallinity database for semiconductor and photonics fabrication

With nanosecond laser modulation, the switching time is currently limited to tens of nanoseconds and only nanoresonators below a 100nm thickness can be amorphized. Furthermore, multilevel phase transformation is not obtained, which is important for wavefront control applications. However, given reported femtosecond(fs) laser-induced crystallization[32] and amorphization[121] effects on silicon, we anticipate fs-laser irradiation on silicon nanoresonators can further improve the switching frequency, expand the resonator size and thereby provide multilevel phase transformations. With the controlled number of fs laser pulses or cooling time, preliminary studies[32,140] show that multilevel phase transformations can be obtained through deliberately inducing combined crystalline and amorphous phases.

Based on a realistic COMSOL simulation in Fig. 4.14, we predict the quenching behavior of a nanodisk upon a sub-nanosecond pulsed heat source. The simulation readily shows that nanodisks with thickness up to 50 nm can quench to 1000K in around 1 ns, while thickness up to 500nm can quench within 10ns. The maximum cooling rate and switch speed are essentially limited by the heat conduction to the surrounding media. If we impose femtosecond or picosecond laser irradiation on the nanoresonator, the surrounding media will not be heated up before full-melting, which gives the fastest possible heat dissipation to the molten silicon. Here we estimate the fastest cooling through simulating the heat dissipation of a nanodisk with a temperature at melting point (COMSOL Multiphysics). The substrate's thermal conductivity is set to be either 1.5 or 15 W/mK, representing the silica or silicon nitride cases. As we can see from Fig. 4.14, the fastest cooling exists when the nanodisk is small, thin and the substrate is of high thermal conductivity. For nanodisks up to 500nm in diameter and 50nm in thickness, it still takes less than 1 ns to quench below 1000K. For disks with 500nm thickness, it is still possible to quench to below 1000K within a similar time scale as measured in nanosecond laser irradiation. The thermophysical properties are attached in Table.2.1.
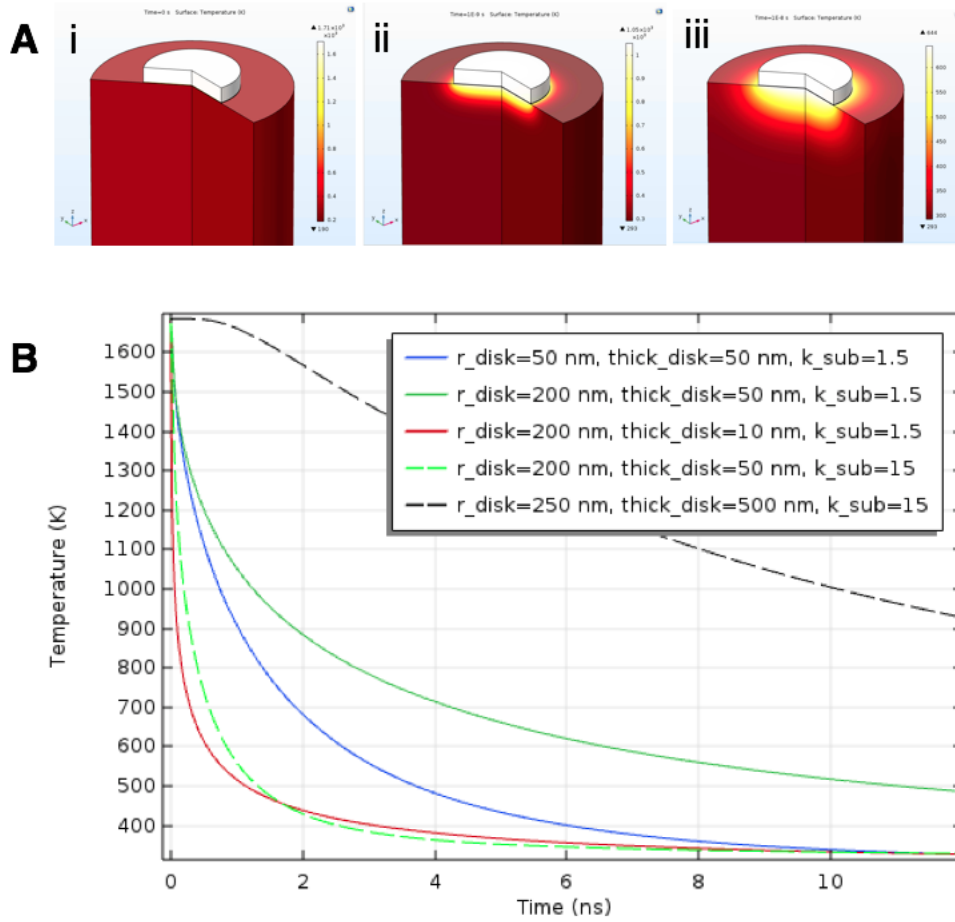
Figure 4.14 Faster quenching and larger domain sizes enabled by femtosecond laser irradiation. (**A**) The temperature field evolution. (**B**) temperature evolution for the center of nanodisk with different disk geometries

The silicon phase transformation consumes energy on the same order as GST. We adopted the same simulation used in Fig. 4.14, with the difference that the nanodisk is 30nm thick and the pulse duration is 13 ns. In Fig. 4.15, the isolated cases refer to bare, un-supported nanodots and are calculated based on just the sensible and latent heat required for melting. The energy required for melting isolated Si is three times of that for GST. However, the difference is smaller when the nanodot is on the substrate and irradiated by a nanosecond laser. The shaded area stands for the possible range based on different laser pulse durations from sub-nanosecond to 13 nanoseconds. On silica substrates, silicon consumes around 2-3 times the energy compared to GST.

Pulse Energy Required for Melting
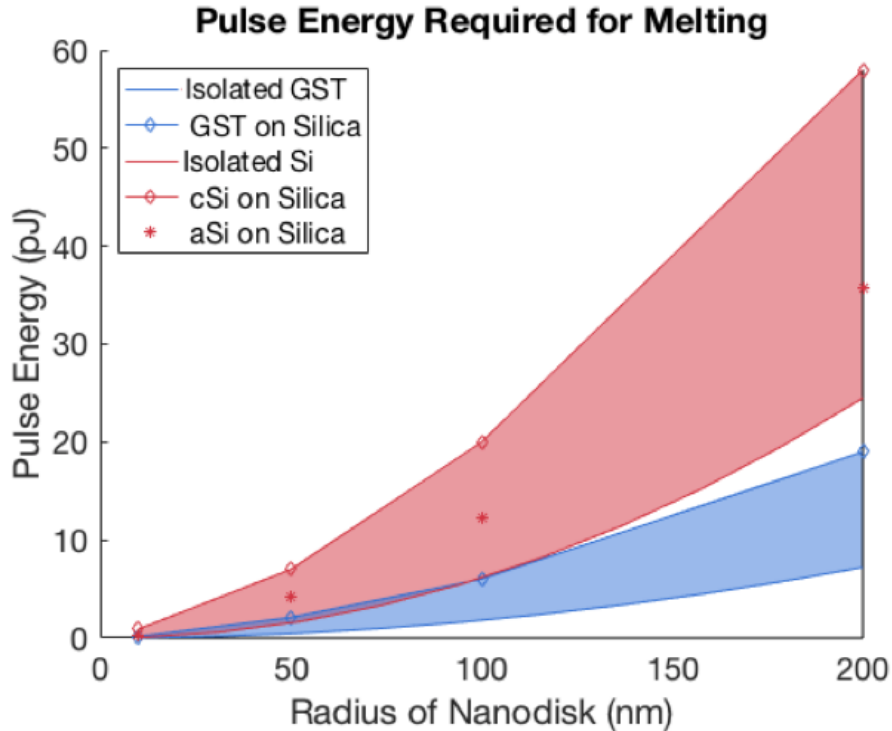
Figure 4.15 Required pulse energy to melt Si vs. GST. Blue shaded area stands for GST and the red stands for Si.

We will link the nanostructure phase transformation to the optical response through a comprehensive library(Fig. 4.16A). For example, on-chip integration requires high-contrast transmission and phase delay with no significant requirement on the period. On the other hand, metasurfaces typically target a very small footprint. The substrates and capping conditions for these applications also differ. The nanostructure geometry is associated with its photonic functionalities, including optical transmission, phase delay and nonlinear properties. The fundamental input includes the amorphous and crystalline phase complex refractive index. On one level, the model will predict the range of transmission contrast(Fig. 4.16B) and the phase delay(Fig. 4.16C) to generate optimized structures. On another, the geometry defines the quench rate and associated laser pulse parameters for crystallization and amorphization.

Optimization algorithms among competing criteria should be pursued. Significant transmission and phase delay contrast are obtained through larger size nanodisks, whose dimensions are close to the wavelength of visible light. Larger size entails larger height or lateral diameter (Fig.4.16B-C). However, larger height induces slower phase transformation while larger diameter increases the footprint and discontinuity of geometrical phases. A delicate trade-off needs to be made and preferably through optimization algorithms.
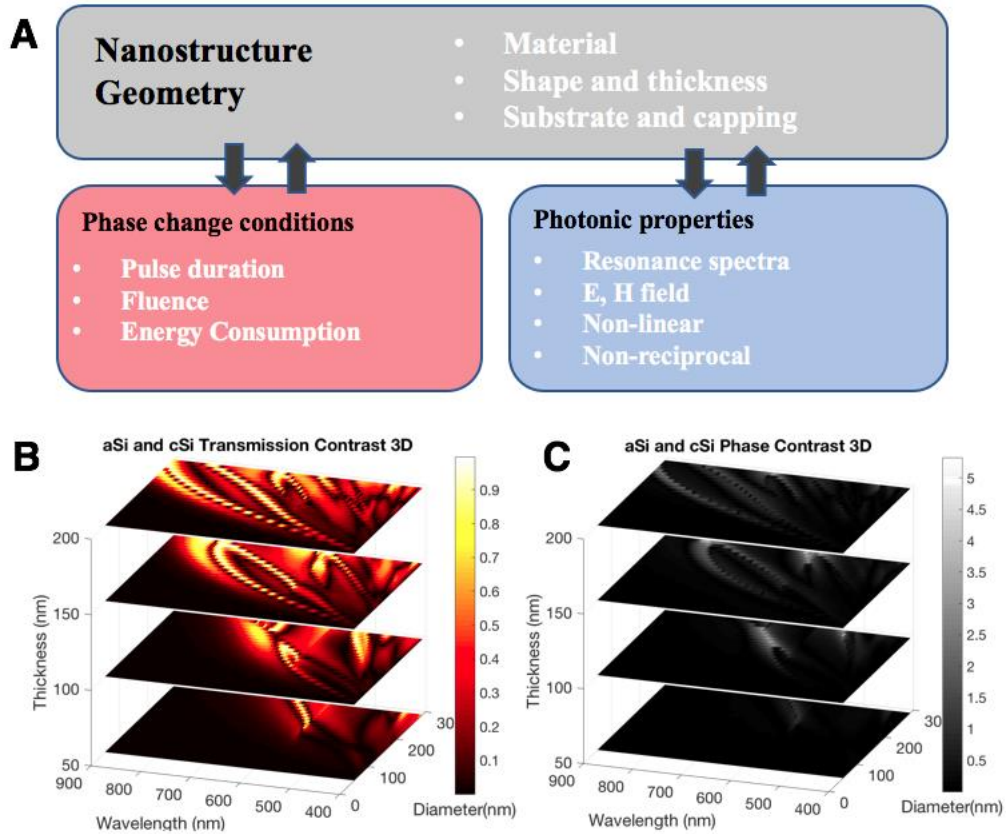
Figure 4.16 Building database for building active photonic devices. (**A**) The library linking the phase change and optical properties of silicon nanostructures; (**B**) transmission contrast and (**C**) phase delay of crystalline and amorphous phase silicon nanodisks with different thickness and radius at different wavelengths.

5 Ultrafast femtosecond laser interaction with silicon nanostructure

5.1 Introduction

As discussed in the chap. 1.2.1, the pulse duration of the femtosecond (fs) laser is shorter than the time scale of thermalization between carriers and lattice, therefore it provides a precise excitation and probing tool to study light-material interaction and fundamental material light interaction in ultra-high temporal resolution. Extensive studies have been carried out on the fs laser interaction with bulk semiconductor materials, including the carrier dynamics[142], non-thermal melting[143], solidification[121] and ablation[144,145].

Carrier dynamics and non-thermal melting have been well-studied. When laser irradiation is applied at low fluence near the melting threshold, thermal melting takes place at around tens of picoseconds, increasing its reflectivity[146]. For high fluences, the multiphoton absorption promotes a large number of valence electrons to the conduction band. These carriers can energize the vibrations of longitudinal optical (LO) phonons and subsequently the atomic ordering. This effect is previously called as plasma annealing and recently recognized as non-thermal melting[147]. The ultrafast non-thermal disordering will give rise to reflectivity as well as reduce the Second Harmonic Generation (SHG) signals of bulk silicon[148]. Confirmed by pump-probe femtosecond X-ray experiments, the non-thermal melting initiates at sub-picosecond and completes at several picoseconds [147].

For solidifications, amorphization is mostly observed and studied. However, different time scales are reported on the amorphization experiments, indicating a big range of quench rates. One experiment found the melting state will exist for tens of nanoseconds for InSb and tens of nanometers amorphous layer is formed, inferring that it initiated from the solid-liquid interfaces[149]. Another experiment pushed the absorption depth to 7nm and used silicon as a high conductivity substrate, indicating an amorphization time scale at 600 ps[121]. A relaxation map of silicon is proposed to link the undercooling and time scale for predicting stable phases, which helps explain the large spread of the time scales.[134]

For ablation, three energy-dependent mechanisms have been identified in bulk semiconductors. For low fluences (below 100 mJ/cm2), the material removal is based on the evaporation and sublimation which happens in the nanosecond and microsecond time scales[150]. For high fluence at 300-500 mJ/cm2, the material is heated and melted sufficiently, hence homogeneous nucleation induced bubble formation leads to spallation, phase explosion. For even higher fluences (around 1J/cm2), a gaseous plasma phase is formed and the induced strong space-charge effects lead to the material ejection, which is widely termed as Coulomb explosion[151]. For the last regime, our group has carried out pump and probe reflection and shadowgraph characterization on silicon substrate[144,152]. The details of plasma formation processes are modeled and validated recently[153].

Compared to bulk semiconductor materials, limited investigations have been carried out on thin films. Fs laser-induced thin-film crystallization is initiated from the surface layer and propagate towards the substrate interface[154]. The crystallization will further modify the surface morphology of the thin film and was applied to generate photo-

trapping structures[155] for photovoltaic applications[156]. Material removal of semiconductor thin film is limited[32] and the *in situ* observation is absent. On metal thin films, the melting and generation of gas introduce bulging and material removal. Ablation studies on insulating and metal thin films both have established that hydrodynamic material removal occurs in nanosecond or longer time scales[157,158].

When the spatial resolution is reduced to the nanoscale, the ultrafast laser interaction becomes fundamentally different. Silicon nanoresonators feature strong light localization due to Mie resonance[104] and demonstrate low ohmic loss compared to the plasmonic counterpart. Femtosecond laser interaction with Mie resonant nanocrystalline silicon nanoparticle found an ultrafast 2.5ps relaxation time.[159] Through analytical modeling, the authors further argued a transient scattering pattern change based on the ultrafast carrier dynamics. Beyond carrier dynamics and optical properties, studies towards phase transformation and structure modification are still absent. From fs laser interaction with metal particles, studies revealed that near-field effects have allowed the emergence of two distinct regimes, atomic material removal[160] and explosive[161] ablation. Hence it will be intriguing to explore the ultrafast phase transformation and ablation dynamics in nanoscale.

Besides the fundamental aspects, the exploration of femtosecond interaction with nanoresonators could fuel the development of scalable manufacturing. As we discussed in chap 1.1.1, the difficulty of scalably fabricating nanoresonators has limited the wide application of the functional optical metasurfaces. Pulsed laser processing of nanoresonators has been demonstrated for scalable patterning[162], pixel-addressable patterning[137] as well as single-pixel isotropic tuning[162,163]. However, there is no demonstration of fabrication and tuning of sub-wavelength anisotropic nanostructures. The anisotropic nanostructures, however, are essential to the Fano resonance and Pancharatnam-Berry phases for the sensing and optical phase modulation.

In this chapter, we show a single femtosecond laser pulse can controllably ablate near-field enhanced regions within a silicon nanoresonator. Both 400nm and 800nm femtosecond laser pulses shape the circular nanodisks into polarization-dependent nanobars and bowtie structures based on the incident polarization and fluence. Such controllable shaping can be used for the laser printing of bowtie sensing structures and Pancharatnam-Berry phase metasurfaces. From the laser-material interaction aspect, nanodisks receiving 400nm laser pulses produce rounding edge morphologies, which we refer to as "hydrodynamic" features. The 800nm laser pulses can selectively ablate 420nm or larger nanodisks with irregular cross-section, without evincing additional hydrodynamic deformation. FDTD simulations correlate the ablation with the enhanced electric field. The fact that resonators become amorphized regardless of the existence of the ablation confirmed the ultrafast quenching after either thermal or non-thermal melting. Pump and probe reflection probing confirmed the existence and the sequence of nonthermal melting, ablation and thermal melting.

5.2 Selective material removal within the nanodisk

In Figure 5.1, we show the concept and the experimental results of femtosecond laser-induced selective material removal inside a nanoresonator. Silicon nanodisk arrays are fabricated with diameter *d* from 200nm to 400nm, and a periodicity *p=2d*. 30nm thick

disks are sitting on top of 50nm oxide mesa and fused silica substrate (Fig. 5.1 A). Detailed fabrication methods can be found in section 2.5 and Appendix A3. With a Gaussian-shaped 130 fs laser pulse (Spitfire, Spectra-physics, 800nm), an array of 400nm in-diameter nanodisks received different fluence their specific locations (Fig. 5.1 B). The material removal starts along the y-axis of the resonator (Fig. 5.1B labeled with dashed lines, corresponds to the gold region in Fig.1A inset and is aligned with the polarization direction of the incident laser. With the increase of the incident energy, the removed area expands preferably towards the center with a uniform rate as schematically illustrated in Fig. 5.1C.
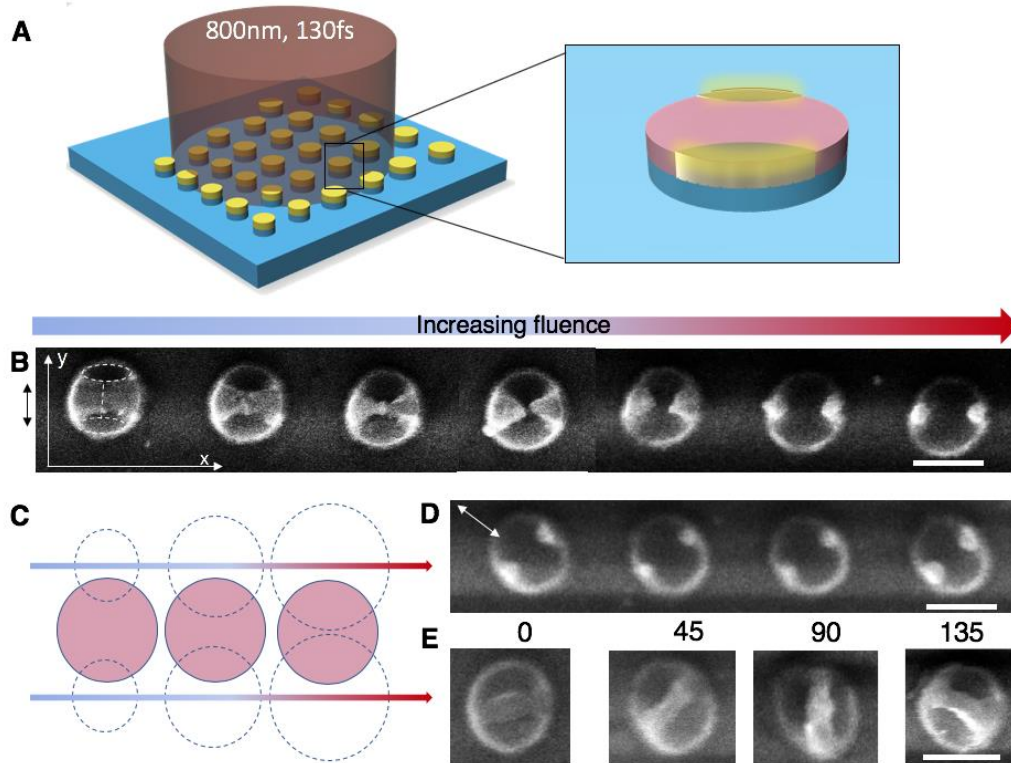
Figure 5.1 Polarization-dependent selective material removal inside silicon nanoresonators. (**A**) schematics of the pulsed laser processing of nanoresonators. (**B**)laser fluence dependent selective material removal on nanoresonator with 400nm size. (**C**) the schematics of the near-field selective material removal with increasing fluence. (**D**) printing nanodot-pair in a tilted angle. Slight image distortion is observed due to the severe charging effect of bare quartz and the periodicity of nanoresonators. (**E**) printing of anisotropic nanobars with arbitrary orientation. The angles of polarization with regard to the vertical direction are plotted on top of each sub-figure. All the scale bars are 400nm

With increasing fluence, the remaining parts formed a connected bowtie structure. There is a protrusion in the center of the bowtie structure, possibly due to hydrodynamic mass transfer. It is believed that the remaining part of the structure, the "bridge" between two islands requires slightly higher incremental energy to ablate. Therefore, the remaining carrier energy after the partial ablation is not enough to ablate the material completely, but enough to generate thermal melting of the sharp tip. With further

increase of the energy, the ablation finally removed the "bridge", and "sculptured" the resonator into a bowtie structure. Furthermore, strong laser irradiation starts to ablate the sharp tips of the bowtie and form a spherical dot along the x-axis. The results show femtosecond laser processing of isotropic nanostructures can generate anisotropic structures with a high degree of controllability based on the fluence. With precise control of laser energy, the bowtie structure can reach a very controlled gap at the range of 10-30nm. Such range has been reported to bring strong near-field enhancement essentially boost fluorescence sensing[164]. More details about this application can be found in section 5.6.

The selective shaping of the resonator can further be modulated by the polarization. In Fig. 5.1D, we show the formation of tilted angle selective removal, which confirms the selective ablation is not related to the orthogonal periodicity of the nanodisks. It is concluded that the ablation is not related to the collective excitation of the nanodisks but just the optical excitation of a single nanodisk. When the polarization is rotated with an arbitrary angle, the deformed structures can also be printed accordingly in Fig. 5.1 E. These polarization-dependent nanobars paved the way to on-demand printing of Pancharactnam-Berry phase metasurfaces. More details about this application is offered in section 5.6.
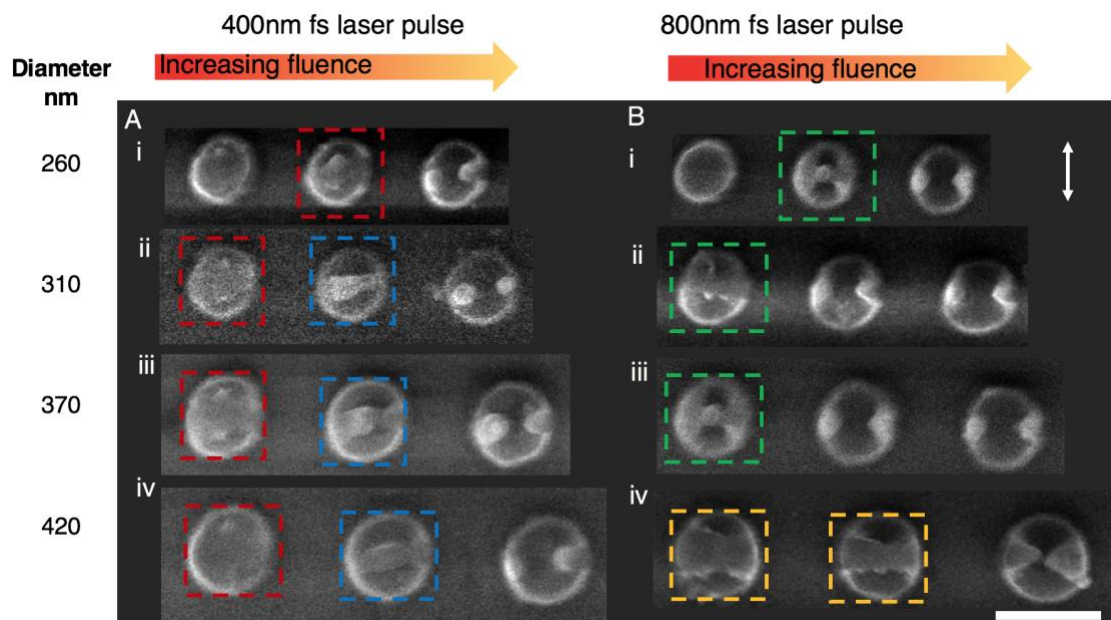
Figure 5.2 Effect of nanoresonator sizes and incident laser wavelength. (**A**) Resonators of irradiated with 400nm wavelength femtosecond laser. The red and blue boxes identify the detachment of the material as well as the formation of the nanobars. (**B**) resonators irradiated with 800nm wavelength femtosecond laser, respectively. The green and yellow boxes identify the resonators that have a protrusion in the middle as well as the resonators with irregular ablation residuals. The diameters for (i-iv) are 260, 310, 370 and 420 nm accordingly. From left to right, the laser fluence is increasing. Incident laser pulse polarization is labeled with arrows. The scale bar is 500nm.

Through the controlled experiments, we further reveal that both the nanoresonator's size and laser wavelength will affect the selective removal process. From Fig. 5.2, it is clear that the ablation initiated from the same location regardless of the incident laser wavelength. For the nanodisks that received 400nm wavelength laser irradiation, three different features are observed compared to those with the 800nm wavelength. A significant delamination effect is observed at the edge of the remaining material (Fig. 5.2A red boxes), i.e. some material appears to be detached from the substrate but not being ablated away. Detailed explanation should be pursued based on comprehensive modeling with electrodynamics. Secondly, we observed a stronger hydrodynamic[165] behavior in the 400nm irradiation (Fig. 5.2A both red and blue boxes),. Thirdly, the ablation is non-uniform in 400nm. When the fluence increases, the removal presents a higher rate near the rim of the disk rather than uniformly in Fig.5.1. As a consequence, no bowtie structures are observed but only the nanobars for high fluence irradiation (Fig. 5.2A blue boxes). With an even higher fluence, similar spherical nanodot pairs are found.

For 800nm laser irradiation, nanodisks with different diameters present different final morphologies. For nanostructures with 420nm diameter or larger, we found the residual material has an irregular cross-section without any rounding (Fig. 5.2B yellow boxes). The irregular geometry resonates with the ablation mechanism of Coulomb explosion, where the material is ejected due to strong space-charge effects with high laser fluences[150]. Nevertheless, the tendency to form a round "ball" in the middle of the bowtie structure is observed on the disks with smaller diameters (Fig.5.2B green boxes). This phenomenon is not well-understood. All these findings warrant detailed optical simulation on the geometry and wavelength-dependent near-field enhancement, which is discussed in the following section.

5.3 Enhancement from FDTD simulation
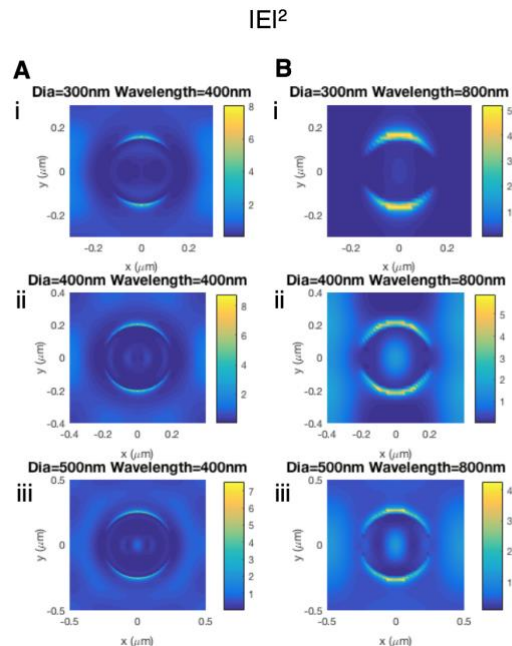
Figure 5.3 FDTD simulation of near-field enhancement on silicon nanoresonators with different diameters. (**A-B**) The plot of E field magnitude with 400nm (A)and 800nm(B) incident laser wavelength respectively. The polarization is aligned with the y-axis.

Through FDTD simulation, we infer laser-induced enhancement is associated with the electric field enhancement. From Fig. 5.3, the maxima of the electric field enhancement are located at the two edges of the resonators and aligned with the y-axis, which agrees with the experimental observations. The agreement is also obtained between different electric enhancement between two incident laser wavelengths in Fig. 5.3A and B. The overall weak ablation and strong hydrodynamic behavior in the 400nm light field are correlated to weaker field concentration. As a result, the carrier excitation does not generate enough space charge to detach the material but provide enough thermal energy to melt them and generate hydrodynamic effects.

However, high field enhancement is associated with the nanodisks with diameters smaller than 420nm(Fig. 5.3B). Its correlation to the center "ball" formation (Fig. 5.2B green box) is not clear, where the "ball" formation is believed to entail excessive thermal melting. A clear explanation of this effect is absent, requiring comprehensive modeling of the light coupling, carrier excitation and dynamics.[54] Note that the reflectivity as well as the non-linear absorption coefficient varies within the pulse due to the transient electron density distribution.

5.4 Evidence of amorphization
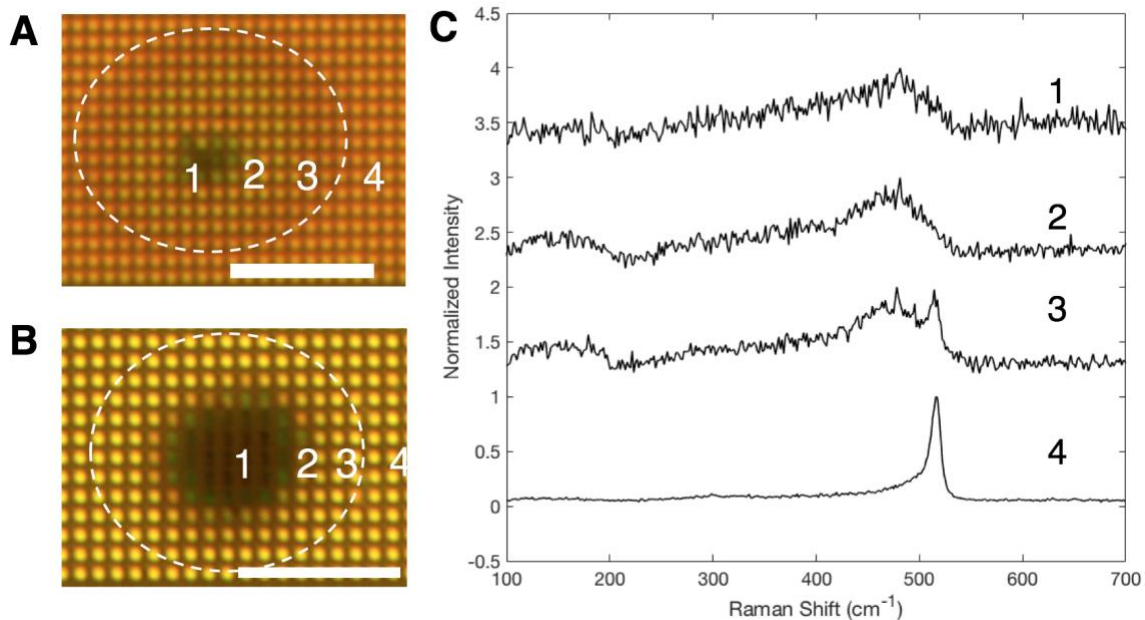
Figure 5.4 Optical and Raman spectroscopic characterization of the femtosecond laser irradiated nanoresonators. (**A**) bright-field image for nanoresonators receiving one 800nm fs laser pulse. The nanodisks have a diameter of 370nm and the period is 750nm. (**B**) the same plot as A with the nanodisks of a diameter of 420nm and a period of 850

nm. (C) Raman shift spectra at different locations in A are plotted accordingly, which is very similar to B. The scale bars are 15 μm.

Through Raman spectroscopy, the irradiated nanostructure is confirmed to be in the amorphous phase regardless of the existence of ablation. In the optical image from Fig. 5.4A, a femtosecond laser pulse irradiated on the polycrystalline silicon nanodisk array. Due to the Gaussian distribution, different regions are formed and labeled as 1-4. Raman spectroscopy is carried out at labeled locations with a focused beam size of 1μm. The color-changed region (location-1) is where material removal happens. The region 2 is believed to have experienced phase change, giving a shifted resonance manifested by yellow color. Region 3 does not present a significant resonance change probably only subject to surface melting and recrystallization. Region 4 is the pristine polycrystalline silicon nanodisks, presenting orange resonance color. From the Raman point measurement, the boundary region 1-2 is determined to have an amorphous phase. Such crystalline to amorphous transformation caused by femtosecond laser irradiation has been reported before in bulk silicon[166][121], which is the first time observed on thin nanostructures. Based on the experiment in bulk silicon[121], we infer the amorphization is caused also by the melting and ultrafast quenching.

For nanodisks smaller than the 420nm in diameter (Fig. 5.4A), the ablation will generate protrusion in the middle as a result of thermal melting. The fact that regions with ablation also resulted in an amorphous phase indicates that fast quenching happens after thermal melting and subsequent hydrodynamic rounding. For nanodisks larger than 420nm(Fig. 5.4B), the ablation should not invoke thermal melting, but the residual resonator turns to the amorphous phase as well. This finding suggests that non-thermal melting could be responsible for incurring disorder the lattice. The fact that regions without ablation (region 2) also become amorphous indicates that other forms of melting exist for these disks, whose experimental characterization can only be done *in situ*.

In summary, we established evidence of quenching and amorphization after the thermal melting, as well as evidence of non-thermal melting. Nevertheless, it remains unknown what happens before the ablation and how does the ablation coexist with thermal melting and hydrodynamics.

5.5 Evidence from pump and probe imaging

Optical pump and probe reflection probing and imaging is a common technique for investigating the transient carrier, thermal and structure change of semiconductor material subject to the ultrashort pulsed laser. The incident laser pulse is beam-split to create a pair of pump and probe pulses with a controlled time delay in between. The pump pulse will modify or modulate the material and the probe pulse will serve as probe signal interacting with the pumped material system. The collection of the reflected probe pulse with a variable time delay formed a view of the material changes induced by the pump laser. The optical setup is built by Minok Park in the laser thermal lab with a similar setup as ref.[144]. Transient states during laser interaction are proposed in Fig. 5.5A . Pump and probe results on the 30nm thin, 500nm disk array are included in Figure 5.5 B-C. The ablation threshold for the silicon nanodisk is calculated based on the

mapping of the image and Gaussian distribution of laser beam, which turns out to be 180 mJ/cm2 for the disk, and 240 mJ/cm2 for the thin film.
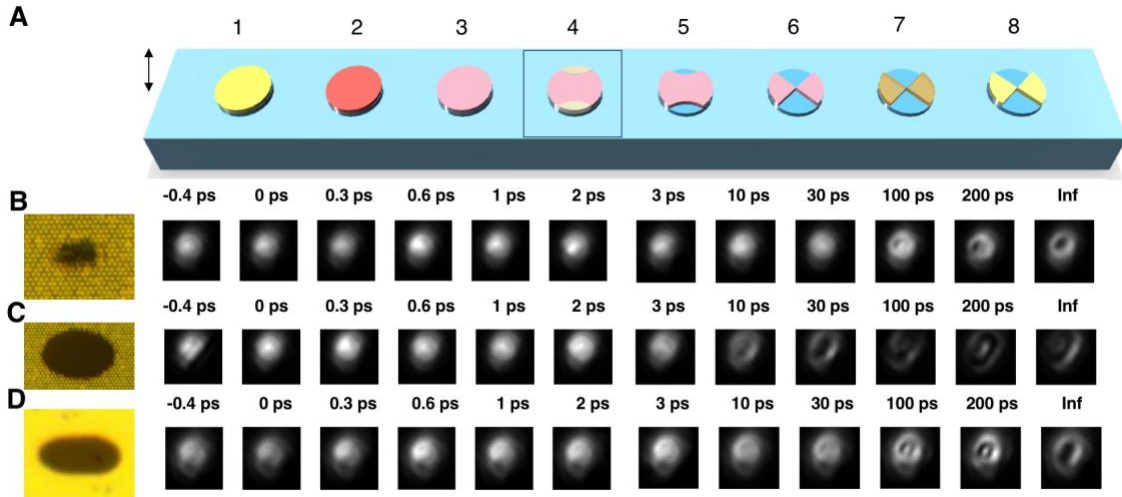
Figure 5.5 Pump and probe imaging of the nanodisks receive fs laser ablation. (**A**) schematics of different states during laser interaction with nanodisks. 1, pristine, 2, carrier excitation, 3, non-thermal melting, 4, charge accumulation, 5, initiation of non-thermal ablation, 6, complete non-thermal ablation, 7, thermal melting and 8, amorphized nanoresonator. (**B-C**) The femtosecond laser processed 500nm-in-diameter nanodisk array with (B) low power and (C) high power. (**D**)The femtosecond laser processed nanodisk array with the same power as C. 10X objective lens has been used for pumping and probing. For the reflected light, only those with the same polarization is collected.

From the pump-probe images in Fig. 5.5, we first clearly see an increased reflection starting within 1ps and extended through 3ps. As normal thermal melting requires a time scale of 1 ns[53], such a high reflection state has to be associated with the carrier induced effects.. In the optical reflection[167] and SHG[168] experiments, the ultrafast high energy pulse will introduce dense electron-hole plasma. This dense carrier indeed can increase the reflectivity but restores to normal within 1ps[144], which is not the case in our experiment. If the excitation is strong enough, the x-ray diffraction experiment[143,147] unambiguously shows excited carriers will transfer the energy to Longitudinal optical (LO) phonons and vibrate the lattice in a picosecond time scale and introduce so-called non-thermal melting[147,167]. The high reflectivity started fade at around 3-10 ps. It is because the generated carriers is continuously thermalize with the phonons[53], weakening the lattice disordering effect. Later on, we see the emergence of a dark region at the center of the beam. From the silicon wafer ablation experiments, the dark regions are the indication of a strongly absorbing plasma from ablation[152]. In our experiments, the plasma formation starts as early as 10 ps or as late as tens of ps depending on the pulse energy. It can be explained as the higher fluence will generate higher local field enhancement and total energy, thus bring an earlier ablation. Along with the dark region, we see an increasing reflection in the center of the reflected beam (approximately 200ps). We infer it is the increase of thermal melting beneath the nonthermally molten silicon layer[154].

From the pump and probe imaging, we confirmed the existence and the sequence of the nonthermal melting, the subsequent ablation as well as the thermal melting at the very end. The existence of non-thermal melting explains why ablated nanodisks (>420nm) without hydrodynamic feature will end up forming the amorphous phase, as the non-thermal melting has already discorded the lattice. Those with hydrodynamic features have experienced thermal melting and subsequent quenching. The sequence between ablation and thermal melting explained why there are hydrodynamic behaviors after partial materials removal.

We include a comparison between nanoresonators (Fig. 5.5C) and thin films irradiated from the same pulse energy (Fig. 5.5D). As we can see, the nanodisks present a stronger and earlier plasma formation compared to the thin film. However, the difference in the actual energy coupling efficiency prevents us from establishing a strong claim that the nanodisks have more severe and earlier ablation due to the near-field enhancement. Further studies, possibly at the single nanodisk level are needed to clarify these issues.

5.6 Potential applications

Crystalline silicon dimer has been proven to provide Surface Enhanced Raman Spectroscopy(SERS) and Surface Enhanced Fluorescence (SEF). [164] While the field-enhancement and associated SERS is not as strong as plasmonic counterparts, the SEF effect on silicon dimers is one order higher than that on plasmonics, which is due to the suppression of fluorescence quenching effects. Amorphous silicon dimer has also been confirmed the SEF and can facilitate the single molecular fluorescence[169]. Compared to dimers, the field enhancement of bowtie structures can be more precisely confined in the gap between two resonators without leaking in the rims, which becomes a better candidate for spatially-resolved chemical and biological imaging[170]. However, both dimers and bowties are patterned through Electron Beam Lithography (EBL), which is costly and offers low throughput.

Here we show fabrication of gap controlled bowtie structures through femtosecond laser selective ablation. Through FDTD simulation, we see the a-Si bowtie structures can provide 7 fold of field enhancement just as the c-Si ones(Fig. 5.6 B and D). The near field enhancement changes less than 1.5 times from 15 nm gap to 80 nm gap (Fig. 5.6 A and B). It shows that the enhancement is robust to the variation of gap distance, which correlated to the incident laser energy.
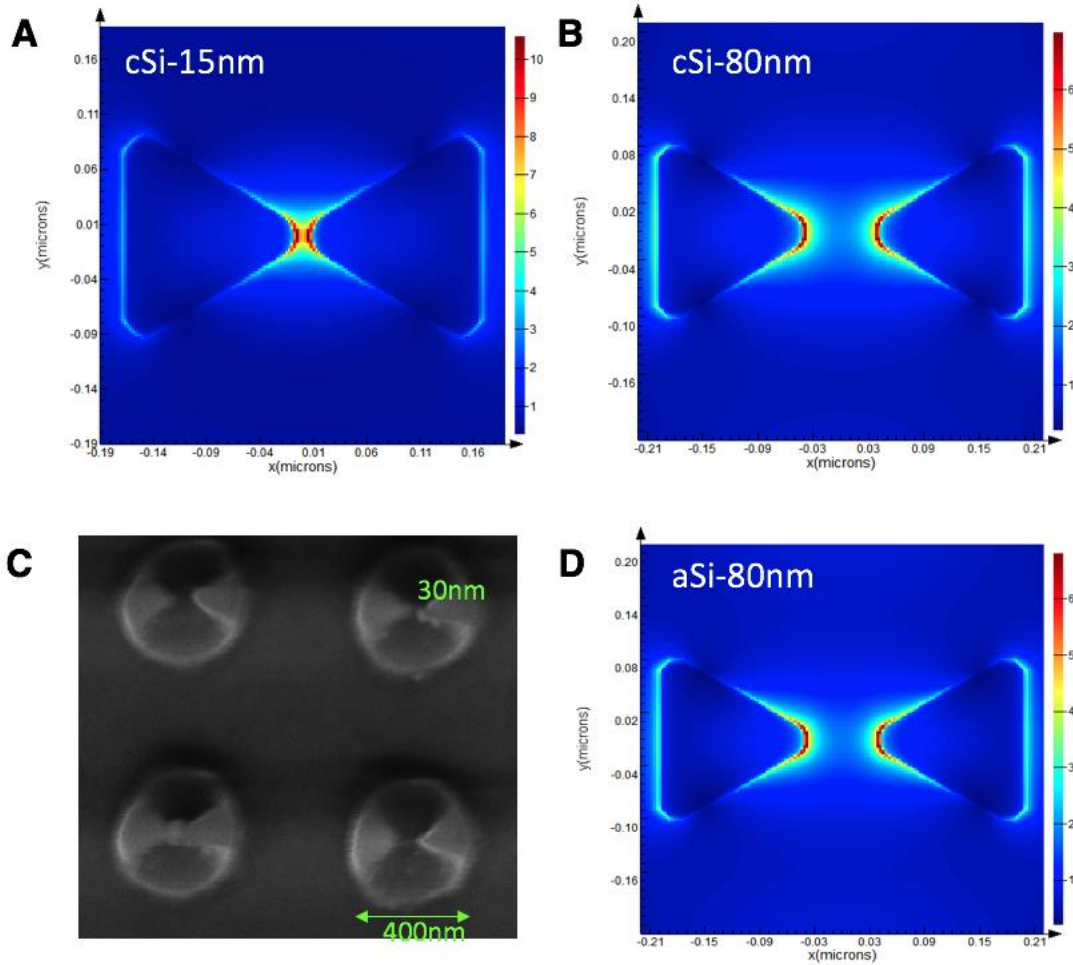
Figure 5.6 The simulated near-field enhancement of the bowtie structure. (**A-B**) the electric field magnitude plot for the crystalline bowtie structures with 15nm(A) and 80nm (B) gap distance. The triangles are modeled from the nanodisks with 400nm in diameter. (**C**) the SEM image of the laser fabricated bowtie structures with different gaps. (**D**) the electric field plot of the amorphous silicon bowtie with an 80nm gap.

As a second application, the femtosecond laser can on-demand print Pancharatnam-Berry (P-B) metasurfaces on a pre-fabricated canvas. As we mentioned earlier, the nanobar orientation can be controlled by the polarization of the incident laser. And it can be used to create the spatially distributed P-B phase for advanced optical functionalities. Here we show that such large scale printing is possible with the expanded laser light (Fig. 5.7A) or the focused laser beam(Fig. 5.7B). Then through FDTD simulation, we demonstrated that periodically placed nanobarn array with different orientations can form P-B metasurfaces (Fig. 5.7C). The periodicity is controlled to be 600nm. When the Right Circular Polarization (RCP) passes through the metasurfaces. The phase of the transmitted Left Circular Polarization (LCP) is spatially placed in gradient, which can be effectively used for the beam steering. It is noteworthy that the visible wavelength beam steering can be formed when the periodicity is smaller than 800 nm. It is important to note that the efficiency of the metasurfaces is determined from

various aspects, including the geometrical placement of the P-B resonator, as well as the individual resonator's transmission contrast between x and y components of the electrical field. For individual resonators, the contrast of the transmission coefficient should be optimized through varying the geometry of the nanobars. A higher anisotropy is generally creating a larger contrast.
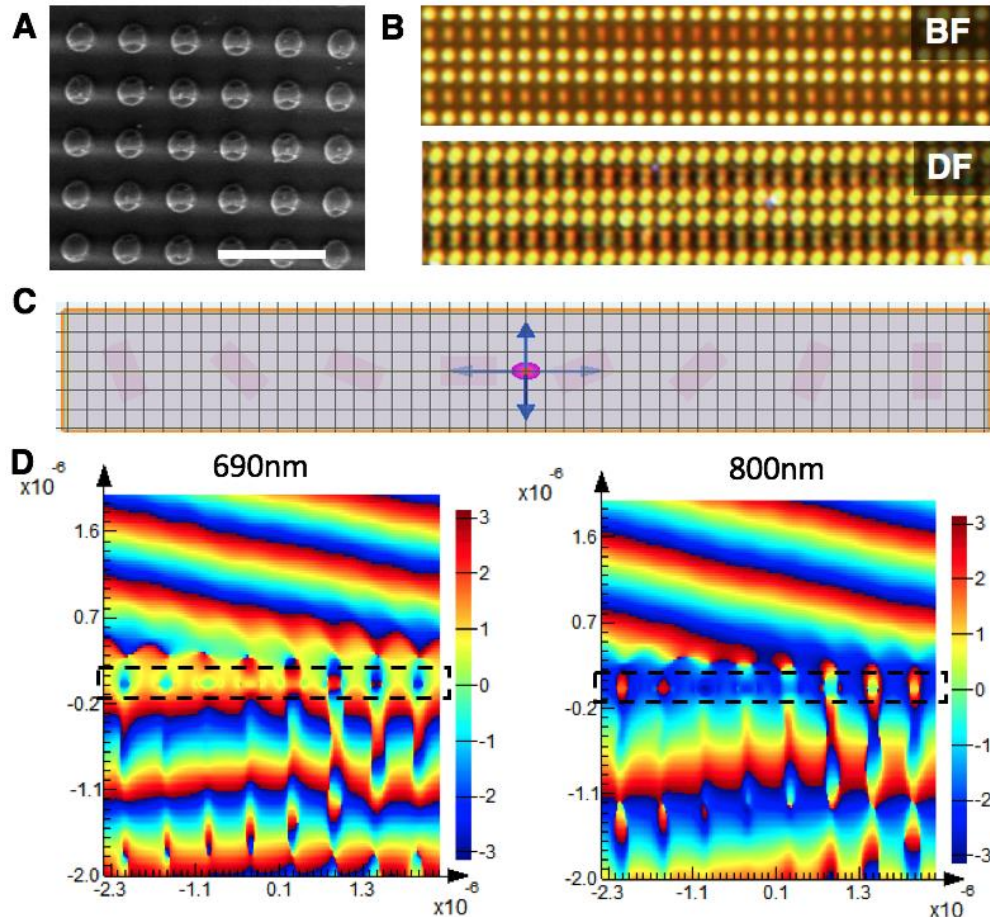
Figure 5.7 Proposed laser printable Pancharatnam-Berry phase metasurfaces. (**A**) the SEM images of the large scale printed nanobar array. The scale bar is 2 μm. (**B**) The optical bright field and dark field images of the line scanned laser printing of anisotropic nanobar array. (**C**) FDTD simulation setup of 8 nanobar structures with 45-degree incremental rotation. The nanobars are 200*400nm and placed with 600 nm period. (**D**) The left circular polarized (LCP) light phase map when the incident light is right circular polarization (RCP). Both 690nm wavelength and 800nm wavelengths are plotted. The metasurfaces are labeled with black dashed lines. The direction of light propagation is in +y direction. The reflected beam shows a random phase distribution.

6 Conclusion

To recapitulate, this dissertation starts with the introduction to the potential opportunities lying on the pulsed laser processing of silicon nanostructures (Chap.1). The introduction is accompanied by the related fundamental physics of pulsed laser interaction with nanostructures, including optical coupling, heat transfer, and phase transformation (Chap. 2). The heat transfer and phase transformation coupled simulation tool is introduced along with the experimental techniques.

We first utilized the near-field enhanced absorption and surface tension driven liquid instability to demonstrate the optical modulated assembly of silicon nanoparticles(Chap 3). Nanoparticle arrays' number, size and symmetry can be readily modulated through pulsed nanosecond laser's amplitude, polarization and number of pulses. Consequently, the resonance peaks of the silicon nanoparticle array can be controlled on-demand.

Reversible phase transformation on silicon nanostructures is obtained through nanosecond laser irradiation. Through ultrafast quenching of the nanostructure, we realized complete amorphization. With the same nanosecond laser irradiation, we obtained crystallization through near-complete melting and super lateral crystal growth. The reversible phase transformation is probed on a single nanodisk. The transient signal combined with comprehensive simulation revealed the deep undercooling of the liquid silicon and the long amorphization time. It is believed that our results lend support to the postulated silicon relaxation time map posted in 2004. Additionally, we observed the strong geometry pinning effect where dewetting will not happen for molten silicon nanodisks. Through thermodynamic analysis, we show such pinning is due to silicon's large adhesion work with oxide surfaces. Lastly, we applied the reversible resonance shifts to active metasurfaces in the visible range for the display and wavefront control.

With femtosecond laser pulses, we observed and investigated the selective ablation within the nanodisk. From SEM observation and FDTD simulation, we infer it is the enhanced electric field, and subsequent carrier excitation induced "cold" ablation of the nanodisk. Raman spectroscopy shows the crystalline nanodisks all have been transformed into the amorphous phase regardless of the occurrence of ablation. The irregular ablated cross-section and hydrodynamic features indicate both non-thermal ablation and thermal melting take place, depending on the laser fluence, wavelength, polarization and nanodisk dimensions. Pump and probe imaging confirmed the sequence of nonthermal melting, ablation and subsequent thermal melting. With the selective material removal, the isotropic nanodisk can be shaped into anisotropic bowtie with controllable gap distance, which serves as a scalable fabrication method for fluorescent sensing array. The polarization-dependent fabrication of nanobars enables laser printing Pancharatnam-Berry phase metasurfaces.

References

1. Sameshima, T., Usui, S. & Sekiya, M. XeCl excimer laser annealing used in the fabrication of poly-Si TFT's. *IEEE Electron Device Lett.* **7**, 276–278 (1986).
2. Wong, S. *et al.* Monolithic 3D integrated circuits. in *VLSI Technology, Systems and Applications, 2007. VLSI-TSA 2007. International Symposium on* 1–4 (IEEE, 2007).
3. Lisoni, J. G. *et al.* Laser thermal anneal of polysilicon channel to boost 3D memory performance. *Dig. Tech. Pap. - Symp. VLSI Technol.* **95**, (2014).
4. Shipway, A. N., Katz, E. & Willner, I. Nanoparticle Arrays on Surfaces for Electronic, Optical, and Sensor Applications. *ChemPhysChem* **1**, 18–52 (2000).
5. Cavallini, M., Biscarini, F., Gomez-Segura, J., Ruiz, D. & Veciana, J. Multiple Length Scale Patterning of Single-Molecule Magnets. *Nano Lett.* **3**, 1527–1530 (2003).
6. Somorjai, G. A., York, R. L., Butcher, D. & Park, J. Y. The evolution of model catalytic systems; studies of structure, bonding and dynamics from single crystal metal surfaces to nanoparticles, and from low pressure (<10 $_{-3}$ Torr) to high pressure (>10 $_{-3}$ Torr) to liquid interfaces. *Phys. Chem. Chem. Phys.* **9**, 3500–3513 (2007).
7. Stewart, M. E. *et al.* Nanostructured plasmonic sensors. *Chem. Rev.* **108**, 494–521 (2008).
8. Kuznetsov, A. I., Miroshnichenko, A. E., Brongersma, M. L., Kivshar, Y. S. & Luk'yanchuk, B. Optically resonant dielectric nanostructures. *Science* **354**, (2016).
9. Jahani, S. & Jacob, Z. All-dielectric metamaterials. *Nat. Nanotechnol.* **11**, 23–36 (2016).
10. 2011-Cui-Cao-Silicon-Carbon Nanotube Coaxial Sponge as Li-Ion Anodes with High Areal Capacity.pdf.
11. Tsoukalas, D. From silicon to organic nanoparticle memory devices. *Philos. Trans. R. Soc. A Math. Phys. Eng. Sci.* **367**, 4169–4179 (2009).
12. Zijlstra, P., Chon, J. W. M. & Gu, M. Five-dimensional optical recording mediated by surface plasmons in gold nanorods. *Nature* **459**, 410–413 (2009).
13. Wu, H. *et al.* Stable cycling of double-walled silicon nanotube battery anodes through solid-electrolyte interphase control. *Nat. Nanotechnol.* **7**, 310–5 (2012).
14. Fowlkes, J. D. *et al.* Hierarchical Nanoparticle Ensembles Synthesized by Liquid Phase Directed Self-Assembly. *Nano Lett.* **14**, 774–782 (2014).
15. Fowlkes, J. D., Kondic, L., Diez, J., Wu, Y. & Rack, P. D. Self-assembly *versus* directed assembly of nanoparticles via pulsed laser induced dewetting of patterned metal films. *Nano Lett.* **11**, 2478–2485 (2011).
16. Wood, T. *et al.* All-Dielectric Color Filters Using SiGe-Based Mie Resonator Arrays. *ACS Photonics* **4**, 873–883 (2017).
17. Ye, J. & Thompson, C. V. Templated solid-state dewetting to controllably produce complex patterns. *Adv. Mater.* **23**, 1567–1571 (2011).
18. Cui, Y. *et al.* Integration of colloidal nanocrystals into lithographically patterned devices. *Nano Lett.* **4**, 1093–1098 (2004).
19. Flauraud, V. *et al.* Nanoscale topographical control of capillary assembly of nanoparticles. *Nat. Nanotechnol.* **12**, 73–80 (2016).

20. Hong, S., Lee, H., Yeo, J. & Ko, S. H. Digital selective laser methods for nanomaterials: From synthesis to processing. *Nano Today* **11**, 547–564 (2016).
21. Sygletou, M., Petridis, C., Kymakis, E. & Stratakis, E. Advanced Photonic Processes for Photovoltaic and Energy Storage Systems. *Adv. Mater.* **29**, (2017).
22. Makarov, S. V. *et al.* Light-Induced Tuning and Reconfiguration of Nanophotonic Structures. *Laser Photon. Rev.* **11**, 1700108 (2017).
23. Zhu, X., Vannahme, C., Højlund-Nielsen, E., Mortensen, N. A. & Kristensen, A. Plasmonic colour laser printing. *Nat. Nanotechnol.* **11**, 1–6 (2015).
24. Zhu, X., Yan, W., Levy, U., Mortensen, N. A. & Kristensen, A. Resonant laser printing of structural colors on high-index dielectric metasurfaces. *Sci. Adv.* **3**, e1602487 (2017).
25. Chen, Y. *et al.* Dynamic Color Displays Using Stepwise Cavity Resonators. *Nano Lett.* **17**, 5555–5560 (2017).
26. Duan, X., Kamin, S. & Liu, N. Dynamic plasmonic colour display. *Nat. Commun.* **8**, 14606 (2017).
27. Wuttig, M. & Yamada, N. Phase-change materials for rewriteable data storage. *Nat. Mater.* **6**, 824–832 (2007).
28. Gu, M. & Li, X. The Road to Multi-Dimensional Bit-by-Bit Optical Data Storage. *Opt. Photonics News* **21**, 28–33 (2010).
29. Wang, Q. *et al.* Optically reconfigurable metasurfaces and photonic devices based on phase change materials. *Nat. Photonics* **10**, 60–65 (2016).
30. Tittl, A. *et al.* A Switchable Mid-Infrared Plasmonic Perfect Absorber with Multispectral Thermal Imaging Capability. *Adv. Mater.* **27**, 4597–4603 (2015).
31. Michel, A.-K. U. *et al.* Using Low-Loss Phase-Change Materials for Mid-Infrared Antenna Resonance Tuning. *Nano Lett.* **13**, 3470–3475 (2013).
32. Zywietz, U., Evlyukhin, A. B., Reinhardt, C. & Chichkov, B. N. Laser printing of silicon nanoparticles with resonant optical electric and magnetic responses. *Nat. Commun.* **5**, 3402 (2014).
33. Montelongo, Y., Yetisen, A. K., Butt, H. & Yun, S.-H. Reconfigurable optical assembly of nanostructures. *Nat. Commun.* **7**, 12002 (2016).
34. Dong, K. *et al.* A Lithography-Free and Field-Programmable Photonic Metacanvas. *Adv. Mater.* **30**, 1703878 (2018).
35. Michel, A. K. U. *et al.* Reversible Optical Switching of Infrared Antenna Resonances with Ultrathin Phase-Change Layers Using Femtosecond Laser Pulses. *ACS Photonics* **1**, 833–839 (2014).
36. Wuttig, M., Bhaskaran, H. & Taubner, T. Phase-change materials for non-volatile photonic applications. *Nat. Photonics* **11**, 465–476 (2017).
37. Hosseini, P., Wright, C. D. & Bhaskaran, H. An optoelectronic framework enabled by low-dimensional phase-change films. *Nature* **511**, 206–211 (2014).
38. Yin, X. *et al.* Beam switching and bifocal zoom lensing using active plasmonic metasurfaces. *Light Sci. Appl.* **6**, e17016 (2017).
39. Rios, C. *et al.* Integrated all-photonic non-volatile multi-level memory. *Nat. Photonics* **9**, 725–732 (2015).
40. Cheng, Z. *et al.* Device-Level Photonic Memories and Logic Applications Using Phase-Change Materials. *Adv. Mater.* **30**, (2018).
41. Cheng, Z., Ríos, C., Pernice, W. H. P., Wright, C. D. & Bhaskaran, H. On-chip

photonic synapse. *Sci. Adv.* **3**, e1700160 (2017).

42. Sean, L. Memory Industry Perspective of Chalcogenide Glass Uses and Issues New NVM Technology is Rare. in *International Workshop on The New Functionalities in Glass* (2007).

43. Clarke, P. IEDM: SK Hynix makes PCM-based 3D crosspoint memory. *EENews*

44. Salinga, M. *et al.* Monatomic phase change memory. *Nat. Mater.* **17**, 681–685 (2018).

45. Karvounis, A., Gholipour, B., MacDonald, K. F. & Zheludev, N. I. All-dielectric phase-change reconfigurable metasurface. *Appl. Phys. Lett.* **109**, (2016).

46. Pitchappa, P. *et al.* Chalcogenide phase change material for active terahertz photonics. *Adv. Mater.* **31**, 1808157 (2019).

47. Gerislioglu, B., Ahmadivand, A., Karabiyik, M., Sinha, R. & Pala, N. VO2-Based Reconfigurable Antenna Platform with Addressable Microheater Matrix. *Adv. Electron. Mater.* **3**, 1700170 (2017).

48. Li, P. *et al.* Reversible optical switching of highly confined phonon–polaritons with an ultrathin phase-change material. *Nat. Mater.* (2016). doi:10.1038/nmat4649

49. Dong, W. *et al.* Wide Bandgap Phase Change Material Tuned Visible Photonics. *Adv. Funct. Mater.* **29**, 1–9 (2019).

50. de Galarreta, C. R. *et al.* All-Dielectric Silicon/Phase-Change Optical Metasurfaces with Independent and Reconfigurable Control of Resonant Modes. 1–34 (2019).

51. Afkhami, S. & Kondic, L. Numerical simulation of ejected molten metal nanoparticles liquified by laser irradiation: Interplay of geometry and dewetting. *Phys. Rev. Lett.* **111**, 1–5 (2013).

52. Callan, J. P. Ultrafast dynamics and phase changes in solids excited by femtosecond laser pulses. (2000).

53. Sundaram, S. K. & Mazur, E. Inducing and probing non-thermal transitions in semiconductors using femtosecond laser pulses. *Nat. Mater.* **1**, 217–224 (2002).

54. Petrakakis, E., Tsibidis, G. D. & Stratakis, E. Modelling of the ultrafast dynamics and surface plasmon properties of silicon upon irradiation with mid-IR femtosecond laser pulses. *Phys. Rev. B* **99**, 195201 (2019).

55. Phillips, K. C., Gandhi, H. H., Mazur, E. & Sundaram, S. K. Ultrafast laser processing of materials: a review. *Adv. Opt. Photonics* **7**, 684–712 (2015).

56. Deng, Y. *et al.* All-Silicon Broadband Ultraviolet Metasurfaces. *Adv. Mater.* **0**, 1802632 (2018).

57. Staude, I. & Schilling, J. Metamaterial-inspired silicon nanophotonics. *Nat. Photonics* **11**, 274–284 (2017).

58. Shcherbakov, M. R. *et al.* Enhanced third-harmonic generation in silicon nanoparticles driven by magnetic response. *Nano Lett.* **14**, 6488–6492 (2014).

59. Lin, D., Fan, P., Hasman, E. & Brongersma, M. L. Dielectric gradient metasurface optical elements. *Science* **345**, 298–302 (2014).

60. Arbabi, A., Horie, Y., Bagheri, M. & Faraon, A. Dielectric metasurfaces for complete control of phase and polarization with subwavelength spatial resolution and high transmission. *Nat. Nanotechnol.* **10**, 937–943 (2015).

61. Kruk, S. *et al.* Edge States and Topological Phase Transitions in Chains of

Dielectric Nanoparticles. *Small* **13**, 1–6 (2017).

62. Chong, K. E. *et al.* Observation of Fano resonances in all-dielectric nanoparticle oligomers. *Small* **10**, 1985–1990 (2014).

63. Piggott, A. Y. *et al.* Inverse design and demonstration of a compact and broadband on-chip wavelength demultiplexer. *Nat. Photonics* **9**, 374 (2015).

64. Tomlin, S. G., Khawaja, E. & Thutupalli, G. K. M. The optical properties of amorphous and crystalline germanium. *J. Phys. C Solid State Phys.* **9**, 4335–4347 (1976).

65. Aspnes, D. E., Studna, A. A. & Kinsbron, E. Dielectric properties of heavily doped crystalline and amorphous silicon from 1.5 to 6.0 eV. *Phys. Rev. B* **29**, 768–779 (1984).

66. Resonance. *Wikipedia*

67. Liu, J.-M. Optical Resonance. in *Principles of Photonics* 204–223 (Cambridge University Press). doi:10.1017/CBO9781316687109.007

68. Kuznetsov, A. I., Miroshnichenko, A. E., Fu, Y. H., Zhang, J. & Luk'yanchuk, B. Magnetic light. *Sci. Rep.* **2**, 492 (2012).

69. Liu, S. *et al.* Resonantly Enhanced Second-Harmonic Generation Using III-V Semiconductor All-Dielectric Metasurfaces. *Nano Lett.* **16**, 5426–5432 (2016).

70. Shorokhov, A. S. *et al.* Multifold Enhancement of Third-Harmonic Generation in Dielectric Nanoparticles Driven by Magnetic Fano Resonances. *Nano Lett.* **16**, 4857–4861 (2016).

71. Yang, Y. *et al.* Nonlinear Fano-Resonant Dielectric Metasurfaces. *Nano Lett.* **15**, 7388–7393 (2015).

72. Paniagua-Domínguez, R. *et al.* Generalized Brewster effect in dielectric metasurfaces. *Nat. Commun.* **7**, 10362 (2016).

73. Miroshnichenko, A. E. *et al.* Nonradiating anapole modes in dielectric nanoparticles. *Nat. Commun.* **6**, 1–8 (2015).

74. Chen, H.-T., Taylor, A. J. & Yu, N. A review of metasurfaces: physics and applications. *Reports Prog. Phys.* **79**, 76401 (2016).

75. Chen, J., Zhang, G. & Li, B. Thermal contact resistance across nanoscale silicon dioxide and silicon interface. *J. Appl. Phys.* **112**, 64319 (2012).

76. Toberer, E. S., Baranowski, L. L. & Dames, C. Advances in Thermal Conductivity. *Annu. Rev. Mater. Res.* **42**, 179–209 (2012).

77. Wang, Z., Alaniz, J. E., Jang, W., Garay, J. E. & Dames, C. Thermal conductivity of nanocrystalline silicon: Importance of grain size and frequency-dependent mean free paths. *Nano Lett.* **11**, 2206–2213 (2011).

78. Blundell, S. J. & Blundell, K. M. *Concepts in thermal physics*. (OUP Oxford, 2009).

79. McMillan, P. F., Wilson, M., Daisenberger, D. & Machon, D. A density-driven phase transition between semiconducting and metallic polyamorphs of silicon. *Nat. Mater.* **4**, 680 (2005).

80. Okada, J. T. *et al.* Persistence of covalent bonding in liquid silicon probed by inelastic x-ray scattering. *Phys. Rev. Lett.* **108**, 1–4 (2012).

81. Ganesh, P. & Widom, M. Liquid-liquid transition in supercooled silicon determined by first-principles simulation. *Phys. Rev. Lett.* **102**, 2–5 (2009).

82. Errington, J. R. & Debenedetti, P. G. Relationship between structural order and the

anomalies of liquid water . *Nature* **409**, 318–321 (2001).

83. Jackson, K. A. *Kinetic Processes: crystal growth, diffusion, and phase transformations in materials*. (John Wiley & Sons, 2006).

84. Volmer, M. & Weber, A. Nuclei formation in supersaturated states. *Z. Phys. Chem.* **119**, 227–301 (1926).

85. Turnbull, D. & Fisher, J. C. Rate of nucleation in condensed systems. *J. Chem. Phys.* **17**, 71–73 (1949).

86. Im, J. S., Gupta, V. V. & Crowder, M. A. On determining the relevance of athermal nucleation in rapidly quenched liquids. *Appl. Phys. Lett.* **72**, 662–664 (1998).

87. Shneidman, V. A. Interplay of latent heat and time-dependent nucleation effects following pulsed-laser melting of a thin silicon film. *J. Appl. Phys.* **80**, 803–811 (1996).

88. Leonard, J. P. & Im, J. S. Modelling Solid Nucleation and Growth In Supercooled Liquid. *MRS Proc.* **580**, 233 (1999).

89. Leonard, J. P. & Im, J. S. Stochastic modeling of solid nucleation in supercooled liquids. *Appl. Phys. Lett.* **78**, 3454–3456 (2001).

90. Stolk, P.A., Polman, A., Sinke, W. C. Experimental test of kinetic theories for heterogeneius freezing in Si. *Phys. Rev. B* **47**, (1993).

91. In, J. Bin *et al.* Generation of single-crystalline domain in nano-scale silicon pillars by near-field short pulsed laser. *Appl. Phys. A* **114**, 277–285 (2014).

92. Xiang, B. *et al.* In situ TEM near-field optical probing of nanoscale silicon crystallization. *Nano Lett.* **12**, 2524–9 (2012).

93. Voutsas, A. T., Hatalis, M. K., Boyce, J. & Chiang, A. Raman spectroscopy of amorphous and microcrystalline silicon films deposited by low-pressure chemical vapor deposition. *J. Appl. Phys.* **78**, 6999–7006 (1995).

94. Dmitriev, P. A. *et al.* Resonant Raman Scattering from Silicon Nanoparticles Enhanced by Magnetic Response. *Nanoscale* **8**, 9721–9726 (2016).

95. Kumar, R., Sahu, G., Saxena, S. K., Rai, H. M. & Sagdeo, P. R. Qualitative Evolution of Asymmetric Raman Line-Shape for NanoStructures. *Silicon* **6**, 117–121 (2014).

96. Zywietz, U. *et al.* Electromagnetic Resonances of Silicon Nanoparticle Dimers in the Visible. *ACS Photonics* 150615100343009 (2015). doi:10.1021/acsphotonics.5b00105

97. Zhao, W. *et al.* Fano resonance based optical modulator reaching 85% modulation depth. *Appl. Phys. Lett.* **107**, 0–5 (2015).

98. Zhao, W., Leng, X. & Jiang, Y. Fano resonance in all-dielectric binary nanodisk array realizing optical filter with efficient linewidth tuning. *Opt. Express* **23**, 6858 (2015).

99. Huang, Z. *et al.* Strong-Field-Enhanced Spectroscopy in Silicon Nanoparticle Electric and Magnetic Dipole Resonance near a Metal Surface. *J. Phys. Chem. C* **119**, 28127–28135 (2015).

100. Wang, L. *et al.* Programming Nanoparticles in Multiscale: Optically Modulated Assembly and Phase Switching of Silicon Nanoparticle Array. *ACS Nano* **12**, 2231–2241 (2018).

101. Lumerical Solutions, Inc.

102. Demichelis, F. *et al.* Optical properties of hydrogenated amorphous silicon. *J. Appl. Phys.* **59**, 611–618 (1986).

103. Fu, Y. H., Kuznetsov, A. I., Miroshnichenko, A. E., Yu, Y. F. & Luk'yanchuk, B. Directional visible light scattering by silicon nanoparticles. *Nat. Commun.* **4**, 1527 (2013).

104. Kuznetsov, A. I., Miroshnichenko, A. E., Fu, Y. H., Zhang, J. & Luk'yanchuk, B. Magnetic light. *Sci. Rep.* **2**, 492 (2012).

105. Evlyukhin, A. B. *et al.* Demonstration of magnetic dipole resonances of dielectric nanospheres in the visible region. *Nano Lett.* **12**, 3749–3755 (2012).

106. Evlyukhin, A. B., Reinhardt, C. & Chichkov, B. N. Multipole light scattering by nonspherical nanoparticles in the discrete dipole approximation. *Phys. Rev. B - Condens. Matter Mater. Phys.* **84**, 1–8 (2011).

107. Wu, Y., Fowlkes, J. D., Rack, P. D., Diez, J. A. & Kondic, L. On the breakup of patterned nanoscale copper rings into droplets *via* pulsed-laser-induced dewetting: Competing liquid-phase instability and transport mechanisms. *Langmuir* **26**, 11972–11979 (2010).

108. González, A. G., Diez, J. A., Gratton, R. & Gomba, J. M. Rupture of a fluid strip under partial wetting conditions. *Europhys. Lett.* **77**, 44001 (2007).

109. Habenicht, A. Jumping Nanodroplets. *Science* **309**, 2043–2045 (2005).

110. Qi, D. *et al.* Time-resolved analysis of thickness-dependent dewetting and ablation of silver films upon nanosecond laser irradiation. *Appl. Phys. Lett.* **108**, 211602 (2016).

111. Kelley, J. D. & Hovis, F. E. A thermal detachment mechanism for particle removal from surfaces by pulsed laser irradiation. *Microelectron. Eng.* **20**, 159–170 (1993).

112. Selvaraja, S. K. *et al.* Low-loss amorphous silicon-on-insulator technology for photonic integrated circuitry. *Opt. Commun.* **282**, 1767–1770 (2009).

113. Conde, J. P., Gaspar, J. & Chu, V. Low-temperature thin-film silicon MEMS. *Thin Solid Films* **427**, 181–186 (2003).

114. Bachman, D., Chen, Z., Fedosejevs, R., Tsui, Y. Y. & Van, V. Permanent fine tuning of silicon microring devices by femtosecond laser surface amorphization and ablation. *Opt. Express* **21**, 11048 (2013).

115. Hatano, M., Moon, S., Lee, M., Suzuki, K. & Grigoropoulos, C. P. Excimer laser-induced temperature field in melting and resolidification of silicon thin films. *J. Appl. Phys.* **87**, 36 (2000).

116. Thompson, M. O. *et al.* Silicon melt, regrowth, and amorphization velocities during pulsed laser irradiation. *Phys. Rev. Lett.* **50**, 896–899 (1983).

117. Eiumchotchawalit, T. & Im, J. S. The Mechanism of Excimer Laser-Induced Amorphization of Ultra-Thin Si Films. *MRS Proc.* **321**, 725 (1993).

118. Im, J. S. & Kim, H. J. On the super lateral growth phenomenon observed in excimer laser-induced crystallization of thin Si films. *Appl. Phys. Lett.* **64**, 2303–2305 (1994).

119. Lee, M., Moon, S., Hatano, M., Suzuki, K. & Grigoropoulos, C. P. Relationship between fluence gradient and lateral grain growth in spatially controlled excimer laser crystallization of amorphous silicon films. *J. Appl. Phys.* **88**, 4994 (2000).

120. Liu, P. L., Yen, R., Bloembergen, N. & Hodgson, R. T. Picosecond laser-induced melting and resolidification morphology on Si. *Appl. Phys. Lett.* **34**, 864–866

(1979).

121. Izawa, Y. *et al.* Ultrathin amorphization of single-crystal silicon by ultraviolet femtosecond laser pulse irradiation. *J. Appl. Phys.* **105**, (2009).

122. Jin, S. *et al.* Lateral grain growth of amorphous silicon films with wide thickness range by blue laser annealing and application to high performance poly-Si TFTs. *IEEE Electron Device Lett.* **37**, 291–294 (2016).

123. Im, J. S., Kim, H. J. & Thompson, M. O. Phase transformation mechanisms involved in excimer laser crystallization of amorphous silicon films. *Appl. Phys. Lett.* **63**, 1969–1971 (1993).

124. Flauraud, V., Reyes, M., Paniagua-Dominguez, R., Kuznetsov, A. I. & Brugger, J. Silicon nanostructures for bright field full color prints. *ACS Photonics* **4**, 1913–1919 (2017).

125. Aspnes, D. E. & Studna, A. A. Dielectric functions and optical parameters of Si, Ge, GaP, GaAs, GaSb, InP, InAs, and InSb from 1.5 to 6.0 eV. *Phys. Rev. B* **27**, 985–1009 (1983).

126. Pierce, D. T. & Spicer, W. E. Electronic Structure of Amorphous Si from Photoemission and Optical Studies. *Phys. Rev. B* **5**, 3017–3029 (1972).

127. Chen, X. *et al.* Ordered Au nanocrystals on a substrate formed by light-induced rapid annealing. *Nanoscale* **6**, 1756–1762 (2014).

128. Sangiorgi, R., Muolo, M. L., Chatain, D. & Eustathopoulos, N. Wettability and Work of Adhesion of Nonreactive Liquid Metals on Silica. *J. Am. Ceram. Soc.* **71**, 742–748 (1988).

129. Yavas, O. *et al.* Temperature dependence of optical properties for amorphous silicon at wavelengths of 632.8 and 752 nm. *Opt. Lett.* **18**, 540–542 (1993).

130. Liao, B., Najafi, E., Li, H., Minnich, A. J. & Zewail, A. H. Photo-excited hot carrier dynamics in hydrogenated amorphous silicon imaged by 4D electron microscopy. *Nat. Nanotechnol.* **12**, 871–876 (2017).

131. Ghosh, G. Temperature dispersion of refractive indices in crystalline and amorphous silicon. *Appl. Phys. Lett.* **3570**, 3570 (1995).

132. Beye, M., Sorgenfrei, F., Schlotter, W. F., Wurth, W. & Fohlisch, A. The liquid-liquid phase transition in silicon revealed by snapshots of valence electrons. *Proc. Natl. Acad. Sci.* **107**, 16772–16776 (2010).

133. Thompson, M., Galvin, G. & Mayer, J. Melting temperature and explosive crystallization of amorphous silicon during pulsed laser irradiation. *Phys. Rev. …* **52**, 2360–2364 (1984).

134. McMillan, P. F. Amorphous Materials: Relaxing times for silicon. *Nat. Mater.* **3**, 755–756 (2004).

135. Subramanian, V. Control of nucleation and grain growth in solid-phase crystallized silicon for high-performance thin film transistors. (1998).

136. AGILTRON. High Speed Optical Switches - NanoSpeed. Available at: https://agiltron.com/category/fiber-optic-switches/nanospeed-fiber-optical-switches/.

137. Zhu, X., Yan, W., Levy, U., Mortensen, N. A. & Kristensen, A. Resonant laser printing of structural colors on high-index dielectric metasurfaces. *Sci. Adv.* **3**, (2017).

138. Carstensen, M. S. *et al.* Holographic Resonant Laser Printing of Metasurfaces

Using Plasmonic Template. *ACS Photonics* **5**, 1665–1670 (2018).

139. Li, J. *et al.* Addressable metasurfaces for dynamic holography and optical information encryption. *Sci. Adv.* **4**, eaar6768–eaar6768 (2018).

140. Makarov, S., Kolotova, L., Starikov, S., Zywietz, U. & Chichkov, B. Resonant silicon nanoparticles with controllable crystalline states and nonlinear optical responses. *Nanoscale* **10**, 11403–11409 (2018).

141. Cullis, A. G., Webber, H. C. & Chew, N. G. Amorphization of germanium, gallium phosphide, and gallium arsenide by laser quenching from the melt. *Appl. Phys. Lett.* **42**, 875–877 (1983).

142. Sabbah, A. J. & Riffe, D. M. Femtosecond pump-probe reflectivity study of silicon carrier dynamics. *Phys. Rev. B - Condens. Matter Mater. Phys.* **66**, 1–11 (2002).

143. Siders, C. W. *et al.* Detection of nonthermal melting by ultrafast X-ray diffraction. *Science* **286**, 1340–1342 (1999).

144. Choi, T. Y. & Grigoropoulos, C. P. Observation of Femtosecond Laser-Induced Ablation in Crystalline Silicon. *J. Heat Transfer* **126**, 723 (2004).

145. Bonse, J., Baudach, S., Krüger, J., Kautek, W. & Lenzner, M. Femtosecond laser ablation of silicon–modification thresholds and morphology. *Appl. Phys. A* **74**, 19–25 (2002).

146. Sokolowski-Tinten, K., Schulz, H., Bialkowski, J. & von der Linde, D. Two distinct transitions in ultrafast solid-liquid phase transformations of GaAs. *Appl. Phys. A Solids Surfaces* **53**, 227–234 (1991).

147. Rousse, A. *et al.* Non-thermal melting in semiconductors measured at femtosecond resolution. *Nature* **410**, 65–68 (2001).

148. Shumay, I. & Höfer, U. Phase transformations of an InSb surface induced by strong femtosecond laser pulses. *Phys. Rev. B - Condens. Matter Mater. Phys.* **53**, 15878–15884 (1996).

149. Bonse, J., Wiggins, S. M. & Solis, J. Dynamics of femtosecond laser-induced melting and amorphization of indium phosphide. *J. Appl. Phys.* **96**, 2352–2358 (2004).

150. Hada, M. *et al.* Cold ablation driven by localized forces in alkali halides. *Nat. Commun.* **5**, 1–8 (2014).

151. Roeterdink, W. G. *et al.* Coulomb explosion in femtosecond laser ablation of Si(111). *Appl. Phys. Lett.* **82**, 4190–4192 (2003).

152. Choi, T. Y. & Grigoropoulos, C. P. Plasma and ablation dynamics in ultrafast laser processing of crystalline silicon. *J. Appl. Phys.* **92**, 4918 (2002).

153. Zhao, X. & Shin, Y. C. Coulomb explosion and early plasma generation during femtosecond laser ablation of silicon at high laser fluence. *J. Phys. D. Appl. Phys.* **46**, (2013).

154. Choi, T. Y., Hwang, D. J. & Grigoropoulos, C. P. Ultrafast laser-induced crystallization of amorphous silicon films. *Optical Engineering* **42**, 3383 (2003).

155. Nayak, B. K. & Gupta, M. C. Femtosecond-laser-induced-crystallization and simultaneous formation of light trapping microstructures in thin a-Si:H films. *Appl. Phys. A Mater. Sci. Process.* **89**, 663–666 (2007).

156. Emelyanov, A. V. *et al.* Femtosecond laser induced crystallization of hydrogenated amorphous silicon for photovoltaic applications. *Thin Solid Films* **556**, 410–413 (2014).

157. Unger, C., Koch, J., Overmeyer, L. & Chichkov, B. N. Time-resolved studies of femtosecond-laser induced melt dynamics. *Opt. Express* **20**, 24864 (2012).
158. Rapp, S., Domke, M., Schmidt, M. & Huber, H. P. Physical mechanisms during fs laser ablation of thin SiO2 films. *Phys. Procedia* **41**, 734–740 (2013).
159. Baranov, D. G. *et al.* Nonlinear Transient Dynamics of Photoexcited Resonant Silicon Nanostructures. *ACS Photonics* **3**, 1546–1551 (2016).
160. Shi, L. *et al.* Resonant-Plasmon-Assisted Subwavelength Ablation by a Femtosecond Oscillator. *Phys. Rev. Appl.* **9**, (2018).
161. Plech, A., Kotaidis, V., Lorenc, M. & Boneberg, J. Femtosecond laser near-field ablation from gold nanoparticles. *Nat. Phys.* **2**, 44–47 (2006).
162. Wang, X., Kuchmizhak, A., Storozhenko, D., Makarov, S. & Juodkazis, S. Single-Step Laser Plasmonic Coloration of Metal Films. *ACS Appl. Mater. Interfaces* **10**, 1422–1427 (2018).
163. Zuev, D. A. *et al.* Fabrication of Hybrid Nanostructures via Nanoscale Laser-Induced Reshaping for Advanced Light Manipulation. *Adv. Mater.* **28**, 3087–3093 (2016).
164. Caldarola, M. *et al.* Non-plasmonic nanoantennas for surface enhanced spectroscopies with ultra-low heat conversion. *Nat. Commun.* **6**, 7915 (2015).
165. Downer, M. C., Fork, R. L. & Shank, C. V. Femtosecond imaging of melting and evaporation at a photoexcited silicon surface. *J. Opt. Soc. Am. B* **2**, 595 (1985).
166. Jia, J., Li, M. & Thompson, C. V. Amorphization of silicon by femtosecond laser pulses. *Appl. Phys. Lett.* **84**, 3205–3207 (2004).
167. Shank, C. V., Yen, R. & Hirlimann, C. Femtosecond-time-resolved surface structural dynamics of optically excited silicon. *Phys. Rev. Lett.* **51**, 900–902 (1983).
168. Tom, H. W. K., Aumiller, G. D. & Brito-Cruz, C. H. Time-resolved study of laser-induced disorder of Si surfaces. *Phys. Rev. Lett.* **60**, 1438–1441 (1988).
169. Lund, J., Mehta, R. & Parviz, B. A. Label-free direct electronic detection of biomolecules with amorphous silicon nanostructures. *Nanomedicine Nanotechnology, Biol. Med.* **2**, 230–238 (2006).
170. Yu, N. *et al.* Bowtie plasmonic quantum cascade laser antenna. *Opt. Express* **15**, 13272 (2007).
171. Yee, K. Numerical solution of initial boundary value problems involving Maxwell's equations in isotropic media. *IEEE Trans. Antennas Propag.* **14**, 302–307 (1966).

Appendix

A1. Optical simulation with Lumerical FDTD

The finite difference time-domain(FDTD) is developed by the seminal work of Yee at 1966[171]. Besides the well-known finite difference time stepping. Yee applied centered finite difference operators on staggered grids in space and time for each electric and magnetic vector field component in Maxwell's curl equations.

There are multiple advantages of FDTD compared to the Finite Element Method(FEM). Firstly, FDTD scales linearly with the problem and therefore can be easily parallelized. From the definition, it's excellent for the simulating transient response. Additionally, it is a time-domain method that uses Fourier transformation to deconvolute the response with regard to the different wavelengths, making broadband simulation very efficient. The broadband wavelength capabilities make FDTD stand out as compared to FEM or rigorous coupled-wave analysis (RCWA) method. Additionally, due to the time-domain stepping nature, the method easily accounts the non-linear behavior of the photonics naturally. The advantage of the RCWA method lies in the efficiency of arbitrary geometries but limited to a single frequency and periodic structure. FEM simulations like COMSOL multiphysics, feature capability of integrating multiphysics into the photonics simulation, including thermal effects. Recently with the development of commercial software Lumerical FDTD, the integration of the electrical modules makes FDTD the top candidate for simulating integrated photonics. Detailed operations of the Lumerical FDTD can be found over the tutorials online.
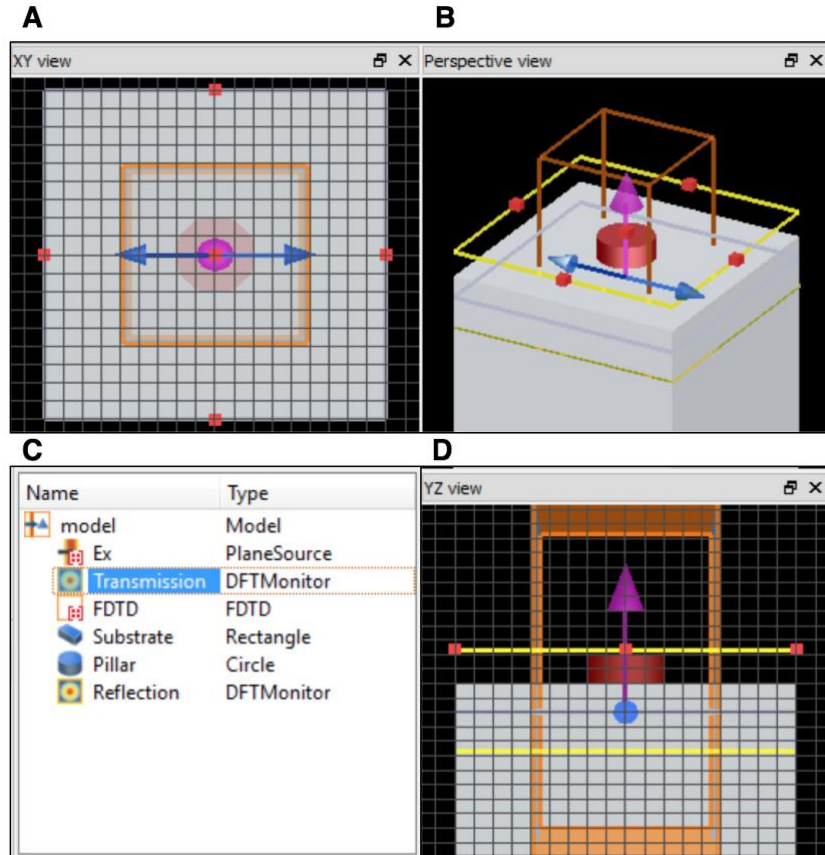
A1.1 Simulation setup

Figure A1.1 FDTD simulation setup and interfaces. (**A**) top view (**B**) perspective View, (**C**) the list of components. (**D**) the side view.

A typical FDTD simulation in Lumerical is setup based on four major components: FDTD domain, object, source, monitors. Scripts can be written for setting up the components, batch running and post-processing. Geometries and settings are shown in Figure A4.1.

FDTD domain is the simulation domain, where the simulation domain size, boundary conditions, mesh and simulation time will be set. For the direction of the light propagation, the domain should be at least 2 times the maximum wavelength. For the lateral direction, the domain size will be decided by the periodicity for periodic structures. As for non-periodic structure, it will be defined by the requirement of generating a far-field plot.

For boundary conditions on light propagation direction, perfectly matched layer (PML) will be used. PML layer is an artificial absorbing layer that no incident wave from non-PML layer will be reflected. For lateral directions, symmetric and periodic boundary conditions can greatly reduce the simulation time. The simulation time is set to be 100fs as it requires a time-domain pulse signal with different frequency components from the setting. Based on the principle of FDTD, the results will be deconvoluted to identify the responses for the different wavelengths. The wavelength information will be set at the source and the monitor.

The object contains both the resonator and the substrate. The successful simulation requires clear identification of the complex refractive index of the materials. The dispersion correlation can be imported as the sample points. For spheres on substrate, proper overlapping of the resonator and the substrate is desired to prevent the infinite sharpness of the simulated structure. Special attention should be paid to the sequence of material construction.

The source is the input of the EM field. Two special sources are used for the simulation in the current work, plane wave and total field scatter field (TFSF). Both cases the light is considered irradiating like a plane wave, where the incident light is from the focused laser and at the focal plane the light field can be considered as a plane wave. Different from the plane wave, the TFSF helps to solve the dark-field reflection measurement, where only the scattering field will escape the source defined "box".

Monitors can be 2D or 3D. For 2D monitors, the transmission is used to record the spectral transmission or reflection based on the positions relative to the object and sources. Monitors between beyond object in the direction of the light propagation is defined as transmission. The monitor behind the source, but within the FDTD domain captures the reflection. The domain named "DFTMonitor" means the frequency domain monitor, where the results at different frequency points can be visualized.

A1.2 Power, transmission and absorption

Poynting vector defines the energy flux of electromagnetic field, which is the cross-product of electric and magnetic field vector:

$$\vec{S} = \vec{E} \times \vec{H}$$

The definition of the power in FDTD is defined as the integral of the energy flux through that surface. The transmission in FDTD is defined as the transmitted power through monitor over the total power from the source.

$$Power = \frac{1}{2} \int_A real(\vec{S}) \cdot d\vec{A}$$

Note that the propagating power is proportional to the real part of the Poynting vector only, which is related to the conservation of energy for the time-averaged quantities. The imaginary part of the Poynting vector relates to the non-propagating reactive or stored energy, such as one might find in the evanescent tail of light being reflected by total internal reflection (TIR). The factor of 1/2 is related to the time averaging of the CW fields.

Therefore it is natural to obtain the absorption from the divergence of the Poynting vector, where absorption can be thought as a sink of the electromagnetic field energy flux.

$$P_{abs} = -\frac{1}{2} * real(\nabla \cdot \vec{S})$$

Unfortunately, the divergence calculation is very sensitive to the numerical scheme. Through the Maxwell equation and the definition of the Poynting vector, the above formula can reach a numerically more stable form.

$$P_{abs} = -\frac{1}{2} * real(i\omega\vec{E} \cdot \vec{D})$$

With simple displacement and permittivity equation, we obtained absorption's correlation to the electric field and the imaginary part of the permittivity:

$$P_{abs} = -\frac{1}{2} * \omega|\vec{E}|^2 img(\varepsilon)$$

These quantities are easily calculated in the FDTD. The square of the E field is intensity, the imaginary part of the permittivity is related to the resistivity of the material.

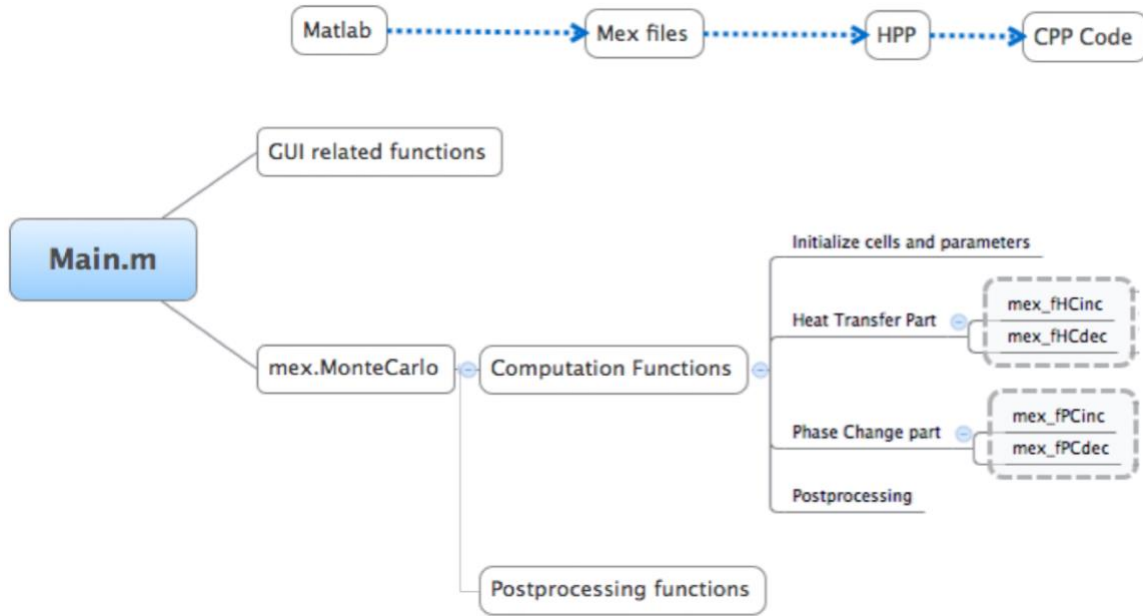## A2. Software architecture of the comprehensive simulation

Figure A2.1 Simulation suroutines mapped into different functionalities

Detailed functions and subroutines are described in the Figure A2.1. The main program (main.m) is hosted in MATLAB to provide easy to access of data analysis and visualization. You can access the simulator with either a graphic user interface (GUI) or a command line interface (CLI). With CLI and scripts, batch run of simulations can be done. For the computations, the time stepping of heat transfer and phase transformation is implemented with C++, together with all the low-level models, including the temperature-dependent thermal properties, optical absorption, and Monte Carlo nucleation etc. C++ is used for speed and memory considerations. A specific mex function is written for the purpose linking C++ to MATLAB. Matlab will compile this mex function and related C++ routines into mex file. The correlations between the data files are listed in the following figure. A detailed operation manual can be obtained upon request.

The pseudo-code for the main simulation program mex_MonteCarlo is described below. The mex_fHCinc, mex_fHCdec, mex_fPCinc and mex_fPCdec are all cpp functions and compiled to Matlab functions. These subroutines execute the time stepping function of the heat transfer and phase transformation.

```
1    % mex_MonteCarlo
2
3        take inputs
4        initialize:
5            1. geometry
6            2. crystalinity
7            3. initial condition
8            4. monitor/save settings
9
10
11   for t=t0:dt:tf
12
13       % the period of t -> t+dt/2
14       laser_energy(t);
15
16       for k=1:1:nz
17           for j=1:1:ny
18               for i=1:1:nx
19                   mex_fPCinc (i,j,k,t, phase transformation );
20                   mex_fHCinc (i,j,k,t, heat transfer);
21               end;
22           end;
23       end
24
25       % the period of t+dt/2 -> t+dt
26       laser_energy(t+dt/2);
27
28       for k=nz:1:1
29           for j=ny:1:1
30               for i=nx:1:1
31                   mex_fPCdec (i,j,k,t+dt/2, phase transformation );
32                   mex_fHCdec (i,j,k,t+dt/2, heat transfer);
33               end;
34           end;
35       end
36
37       data_monitor;
38
39       data_export ;
40
41
42   end
```

Figure A2.2 Pseudo code for the main simulation program

For real-time monitor and post processing purpose, a group of 1D plots is generated and refreshed with the time stepping(Fig. A2.3). Temperature against axial location is also plotted as 1D line curves, which gives a clear view of the heat-affected zone propagation. Real-time point monitors are also placed on the top and bottom of the silicon domain. It helps to monitor the melting and recalescence effect.

A group of 2D plots is also included in the right part of Fig. A2.3. It starts with the fraction of the crystalline and amorphous silicon ratio. As you can see, at the top of the tip, the crystalline silicon ratio becomes zero due to the existence of the liquid silicon. And then the label of crystals including the initial condition and the output real-time results. Melting will be noted as the red color. Once nucleation is initiated, the nuclei will be assigned one random identifier to indicate their identity. With the crystal growth, this label will also be propagated to the regions surrounding it to present the overall size of the grown crystals. During real-time visualization, the crystals can then be visualized with the different colors to present to the outcome of the crystallization. Similarly, we can

also allocate nanocrystals in our initial condition which represent the polycrystalline silicon sample.

In the console of the MATLAB, a log of initial input will be recorded. Then there will be a log record for each event of nucleation, including the location, the temperature and ID will be displayed. It helps to analyze the nucleation events later on.
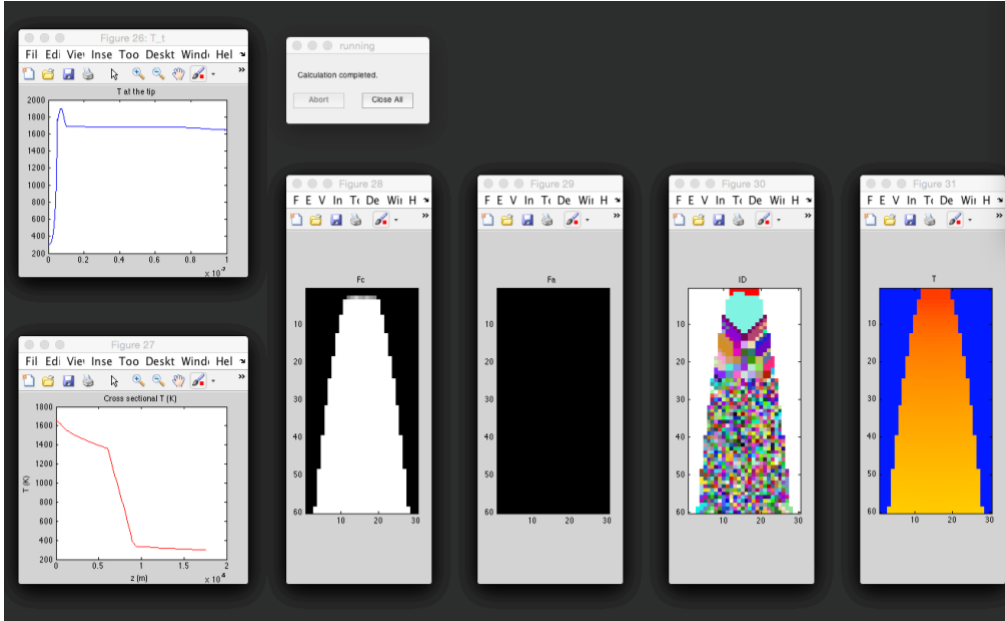

Figure A2.3 Realtime monitoring of the comprehensive simulation

The analytical prediction is compared to the stochastic simulation to offer a perspective how effective of the simulation. To obtain an analytical evaluation of the realistic nucleation history, we extracted the temperature evolution as T=1680-60t (ns) based on the typical cooling process of laser-heated nanodisks. Therefore the nucleation probability for an entire domain is calculated using equation 10 and 11, and the results are plotted in Fig. A2.4-A. The overall probability of having at least one nucleation in the entire domain is plotted in marked lines and the probability of nucleation happens at the (t, t+dt) period is plotted in shaded lines. During the cooling process, the probability of heterogeneous nucleation is larger than that of homogenous nucleation. The figures indicated that over the entire domain the 1_{st} heterogeneous nucleation is bound to happen at 1300-1250K (P_{Het})and the homogenous one is 1100-1050K(P_{Hom}).

Similarly, we also plotted the analytical results for a single node(10nm) inside the domain (Fig. A2.4-B). As we can see from the curve, the probability of nucleation shifted towards lower temperature as the domain size is 400 times smaller. The 1_{st} nucleation only started to pick up significant probability at 1300-1250K(P_{iHet}) and 1100-1050K(P_{iHom}), which is however same as the predicted temperature range of 1_{st} nucleation over the entire domain. It indicates the collective emergence of nucleation probability in each node sums up as a significant increase of the nucleation probability over the entire domain.

In the simulation, the 1_{st} nucleus of the whole domain is captured at around 1200-1250K(Nu_{het}) and 1100K(Nu_{hom}) which is very close to the prediction of 1_{st} nucleation

over entire domain (Fig. A2.4-A P_{Het} and P_{Hom}). Additionally, the distribution of the nucleation event resembles the predicted distribution of single node nucleation (Fig. A2.4-B's P_{iHom} and P_{iHom}), especially the high-temperature part. When the temperature keep dropping, we see the spectra center of both homogenous and heterogeneous nucleation shifted towards the 950K. This is mainly because of the high recalescence effect from large amount of nucleation arrested the cooling curve at around 950K, deviating significantly from the input parameter in the analytical analysis.
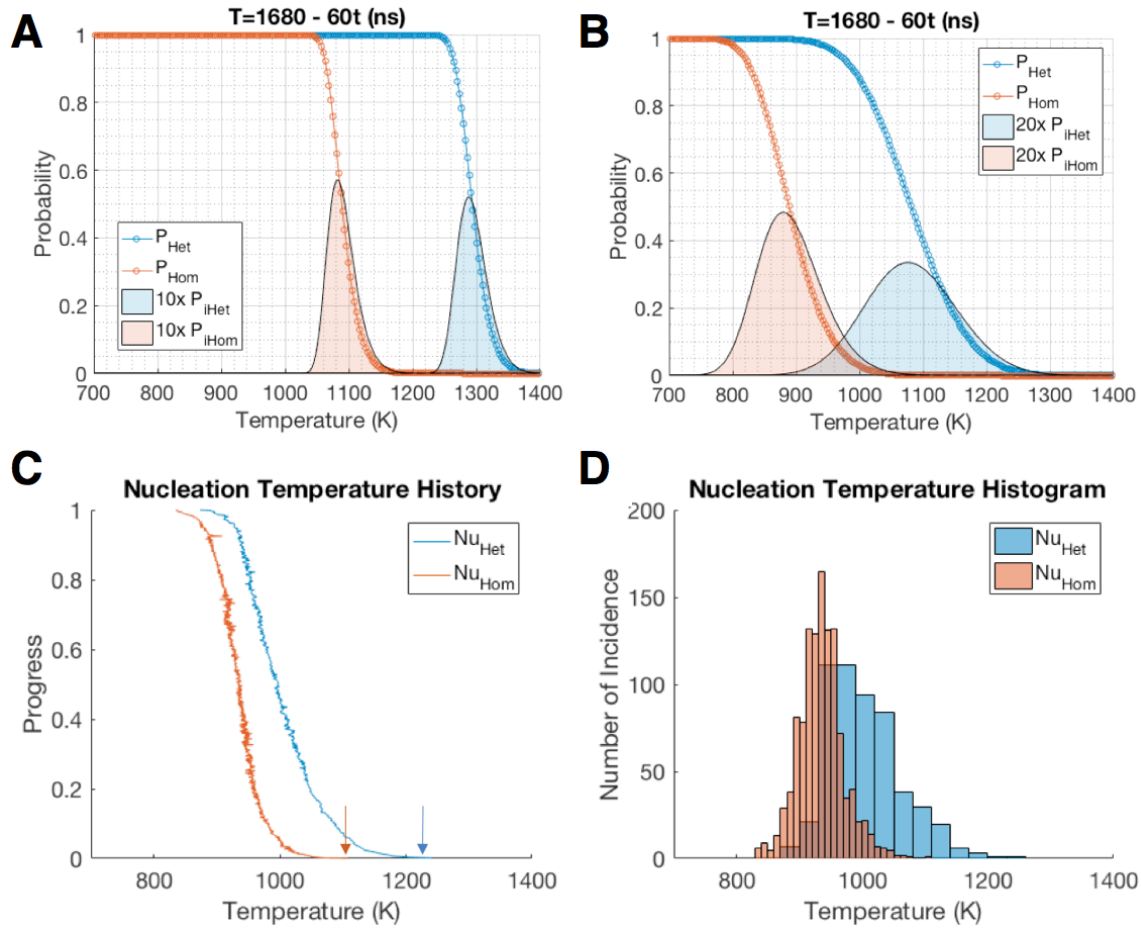

Figure A2.4 Temperature-dependent probability of the heterogeneous and homogenous nucleation. (**A**) Probability analysis through the entire volume using with Area=(200nm)$_2$, V=(200nm)$_2$*30nm, dt=0.05ns. P_{het} and P_{hom} lines are the probability of nucleation happen in the elapsed time t, predicted with Eqn.10. The shaded curves P_{ihet} and P_{ihom} are the probability of nucleation predicted with Eqn.11. (**B**) Probability analysis of an individual node using the same equations as (B) with Area=(10nm)$_2$, V=(10nm)$_3$, dt=0.05ns. (**C**) The temperature history of the nucleation progress, which is the event's time sequence normalized with a total event number. The 1$_{st}$ nucleation is indicated with arrows. (**D**) The temperature distribution histogram of the nucleation event. Both (C-D) are captured from our simulator

Lastly, the high supercooling degree observed at the amorphization process is considered from the high quench rate. Though nucleation starts from 1200K, the limited

numbers of nuclei are not sufficient to release enough latent heat to stop the cooling. As the volume continues cooling, it reaches a degree of supercooling where exponentially increased nucleation sites finally managed to arrest the cooling. Then the lowest supercooling is considered as the onset of amorphization.

A3. Fabrication process of silicon nanoresonators

The silicon nanoresonators went through thin film deposition, lithography, and etching steps. The details are described below.

A3.1. Substrate and thin film deposition

Fused silica wafers from HOYA and University Wafers are used to provide an inert and thermal stable amorphous substrate hosting amorphous silicon precursor. The amorphous silicon will experience melting, nucleation and solidification. Amorphous substrate ensures, no seeds or preferable orientation will affect the nucleation and crystal growth, which ensures our simulation conditions are valid. On the other hand, for optical applications, silica substrate provides high optical transmittance and minimum effect on resonance and field enhancement of the silicon resonator.

The deposition of the amorphous silicon film is carried out via Low-Pressure Chemical Vapor Deposition (LPCVD) at 550$_\circ$C. 550$_\circ$C is below the normal polysilicon growth temperature (600-650$_\circ$C)which ensures there is no growth of the deposited microcrystals. Before sending into the furnace, the silica wafers are all cleaned with Piranha, BHF and dried with quick-dump-rinse(QDR). This MOS-clean process ensures no impurity serve as the heterogeneous nucleation site between molten silicon and oxide substrates. After the MOS clean, it is recommended to use MOS-Clean Furnace (tystar10) instead of NON-MOS furnace(tystar 15). 50nm thick a-Si film is deposited through the standard recipe(10vdasia) through 15min. The growth rate will vary based on the tool condition, details can be obtained from the Staff. Thin-film thickness is confirmed with SEM cross-sectional imaging as the conventional film metrology does not apply transparent substrates. Note that the deposition of LPCVD is not directional, so both sides of the wafer will be deposited, which requires the handling of the wafer to be carefully carried out without contamination on either side.

A3.2 Mask design and lithography

4 layers chrome photomask is designed based on the specifications of ASML 300/5500 stepper in Berkeley Marvell Nanolab. Due to the 4X reduction feature of this stepper, each mask has 4 quadrants to contain one layer of images. Later in the dissertation the layers will be called quadrants to distinguish from the actual layers required for electrical circuit fabrication. The ASML 5500/300 stepper is capable to resolving 250nm resolution, thus 1um resolution on the mask should be developed. The mask cost is a function of the minimum resolution, and a loosely correlation function of the total write time. Hence, four quadrants are fully utilized to provide utilities of patterning positive(#1), negative resonator array(#2), marker(#3) and gradient periodic array(#4). The positive and negative resonator array is designed to provide various nanostructures for the laser processing study. The (#3) marker quadrant is used for

patterning a large array of markers for the 2D material studies for the colleague(Yoonsoo Rho). The (#4) gradient periodic array is for the study of liquid phase transformation and especially Leidenfrost phenomena(Meng Shi).
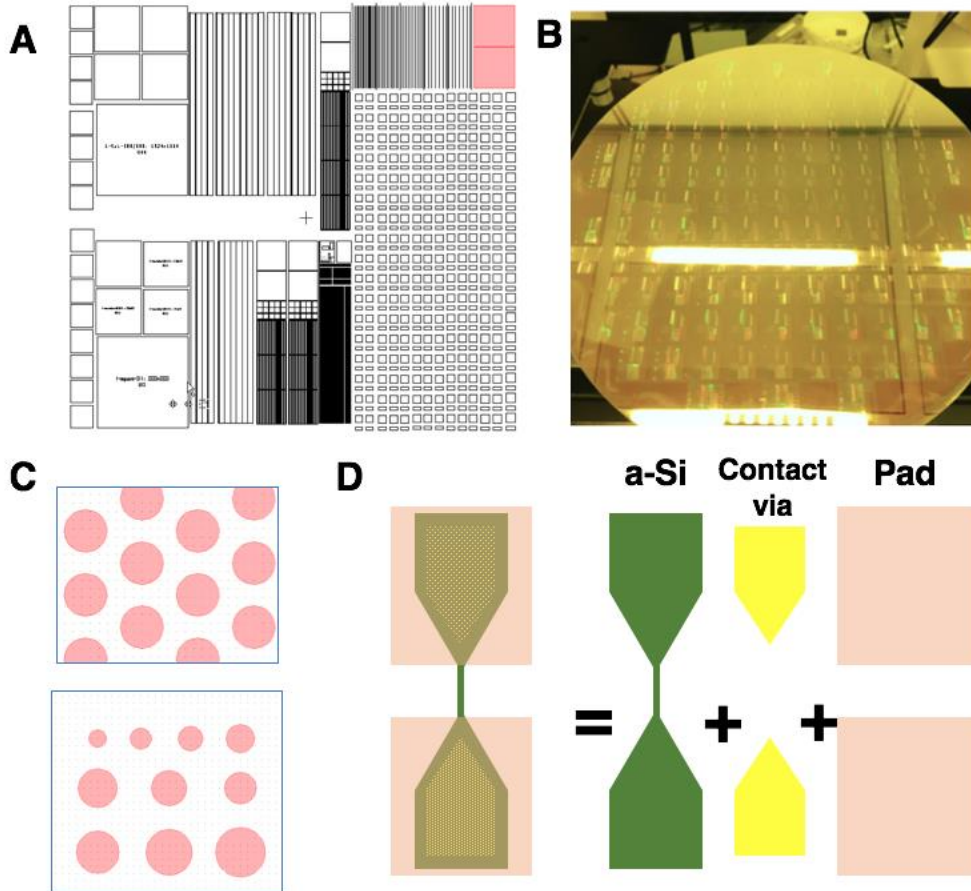

Figure A3.1 The mask design and lithography results of the "nanoplatform". (**A**) mask layout for different regions to be patterned. (**B**) image of fabricated amorphous silicon on silica wafer. (**C**) characteristic designed silicon nanodisk pattern. (**D**) the designed electrical layout pattern employing three quadrants on the mask.

One typical quadrant for positive resonator array is shown in Fig. 3.1-B. The typical periodic array is described below in Fig. 3.1-C. As you can tell from Fig. 3.1-B, long stripes of arrays are employed to maximize the efficiency of the processing and characterization, accounting for the translational movement of the motion stage. Besides the dense silicon resonator array, electrical *in-situ* probing circuits are designed on the mask. Three layers of mask are used for the development simple structure of the circuit (Fig. 3.1-D), which have been allocated into the 1, 2, 3 quadrants of the mask. Note that the third layer will coexist with the marker mask, but not interfere with the mask.

Due to the silica transparent substrate, special permission is obtained before sensing the wafer into the stepper. To avoid failure of the chuck, the backside of the silica wafer should be free of protrusions, which indicates the amorphous silicon thin film deposition from LPCVD should be uniform. DUV resist compatible with ASML stepper

has been applied. It is critical to deposit backside antireflection coating(BARC) before the resist. Automatic prebake, BARC, resist dispensing, edge bead removal and after bake is completed.

A new imaging job is created from the staff named as "LTL_nanoplatform" containing the number of dies and the dimension(10mm*10mm). Then the wafer is fed into ASML tool and the focus-exposure matrix is selected as the mode of exposure. On one 6 inch wafer, over 100 dies can be patterned and processed at same time. In only one-time exposure, a matrix of focus and exposure can be applied, yielding at least 10-15 dies with optimal exposure. These distributed exposure condition is also beneficial in smoothing out the variation from etching. The advantage of using photolithography is that it provides large scale and uniform samples which eliminated the repeated writing and etching time required for Ebeam-lithography.

After exposure, automatic resist development and post-bake are applied using standard DUV recipes provided in Nanolab. It is important to apply the additional baking process to improve the mechanical strength of the resist, which will prevent scratch from handling as well as ensure the proper selective ratio during etching.

A3.3 Etching for pattern transfer

Dry etch and wet etch are both valid methods for transferring patterns from the resist to the amorphous Si thin film. However, reactive ion etching (RIE) provides better process control as the time of processing can be precisely determined. Polysilicon etch recipe with Cl_2, HBr and O_2 gases are used for etching amorphous silicon. As the thickness of our sample is below 50nm, the etch profile is not critical while the etch stop is critical. Standard polysilicon etching recipe in Lam 7 tool inside Berkeley Nanolab is selected as there is an etch stop step can help to determine the end of etching. However, slight over-etch during RIE process still exist, partially because the fast etching rate compared to the standard polysilicon. The slight over-etch leaves silicon sitting on a 50nm thick oxide mesa. Further process improvement can be pursued. Due to the transparent nature of the silica wafer, special care is required when loading the wafer into Lam 7.

A4. Optical setups for the optical characterization

A4.1 Static reflection and transmission spectroscopy

The reflection spectrum measurement is obtained by integrating a commercial reflection probe (Thorlabs RP28) with 100X objective lens (Olympus MS Plan) and measured with a spectrometer (Acton SpectraPro 2300i). The spectrometer is illuminated with the stabilized light source (Thorlabs SLS201) and the reflection spectra is obtained by normalizing reflected signal over the illuminating signal.
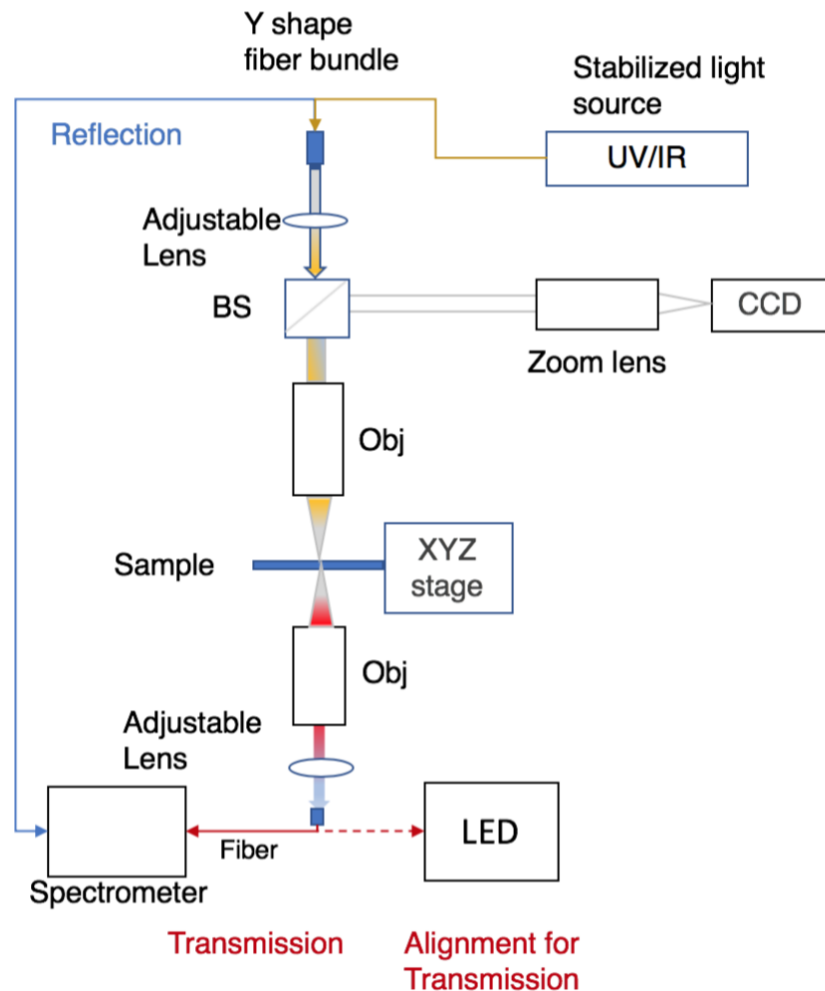
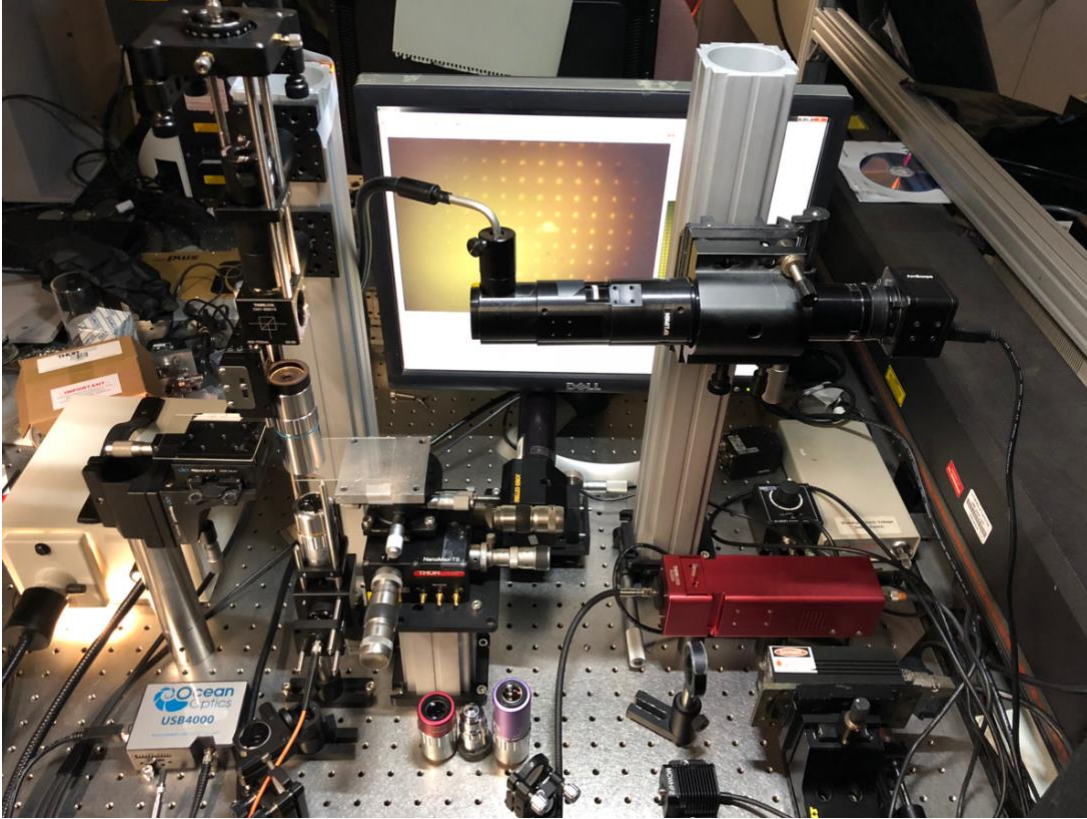Figure A4.1 Schematics of reflection and transmission setup for the nanoresonator's optical responses

Figure A4.2 Photograph of the reflection and transmission setup

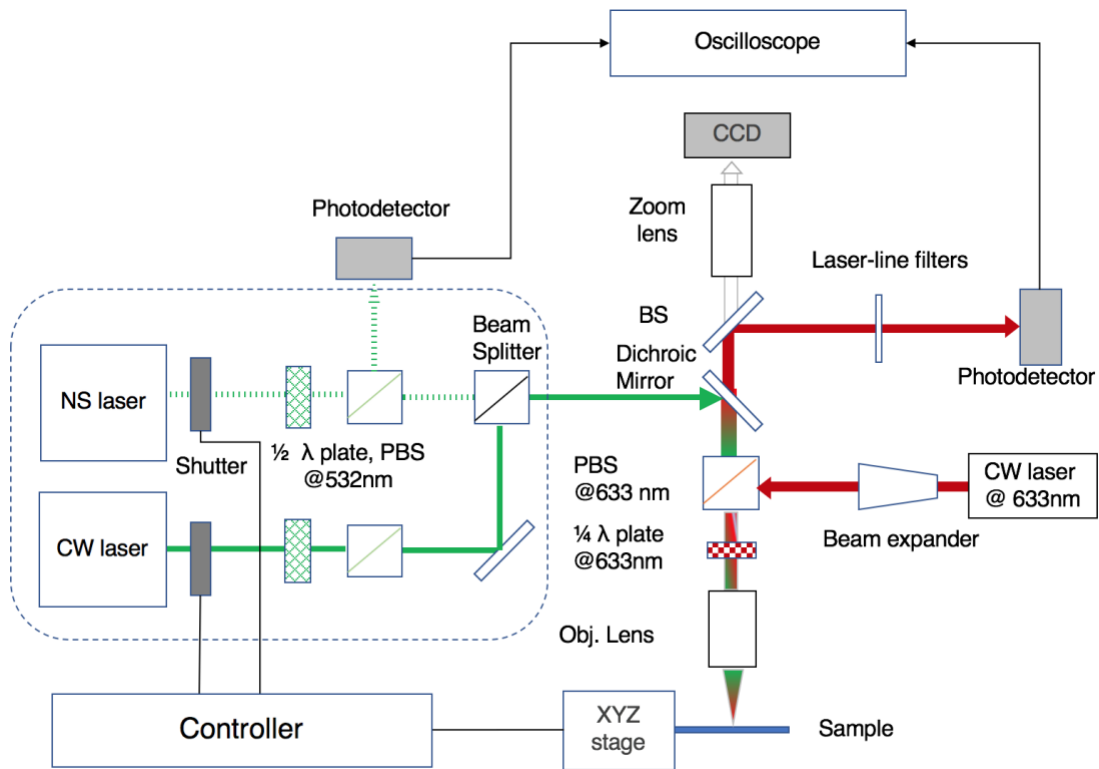## A4.2 Transient reflection probing

Figure A4.3 The schematics of the experimental setup for the reflection probing
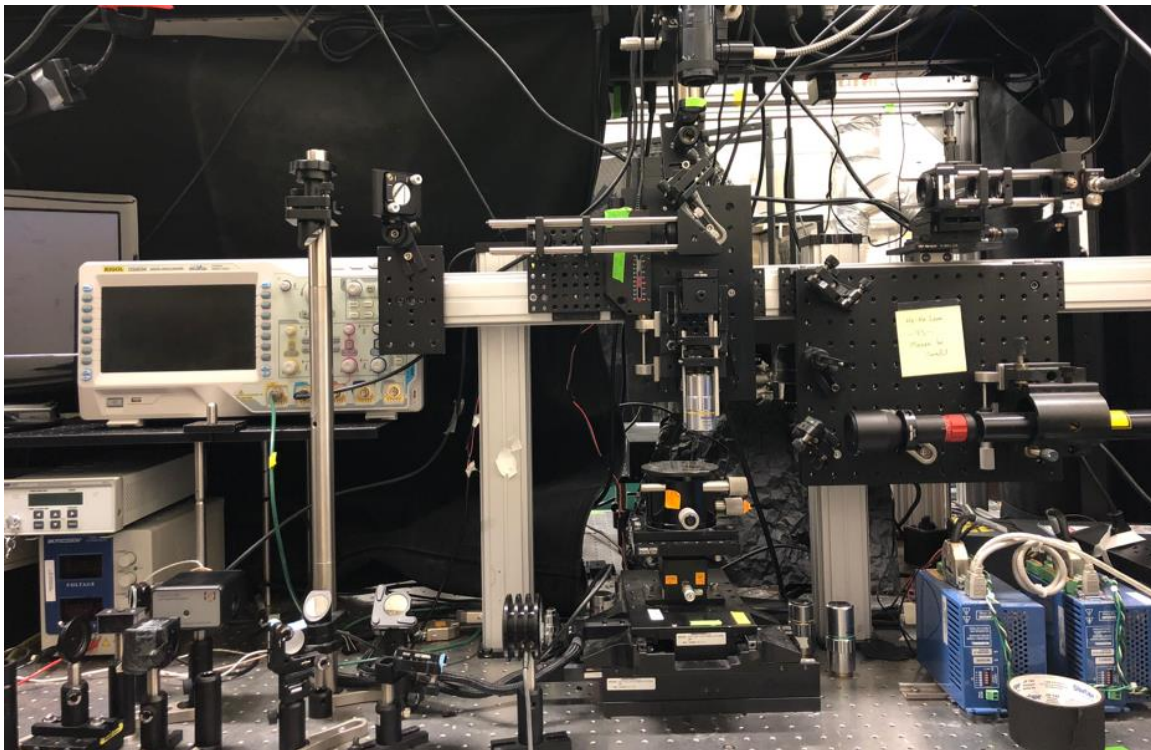

Figure A4.3 Photographs of the schematics for transient reflection probing

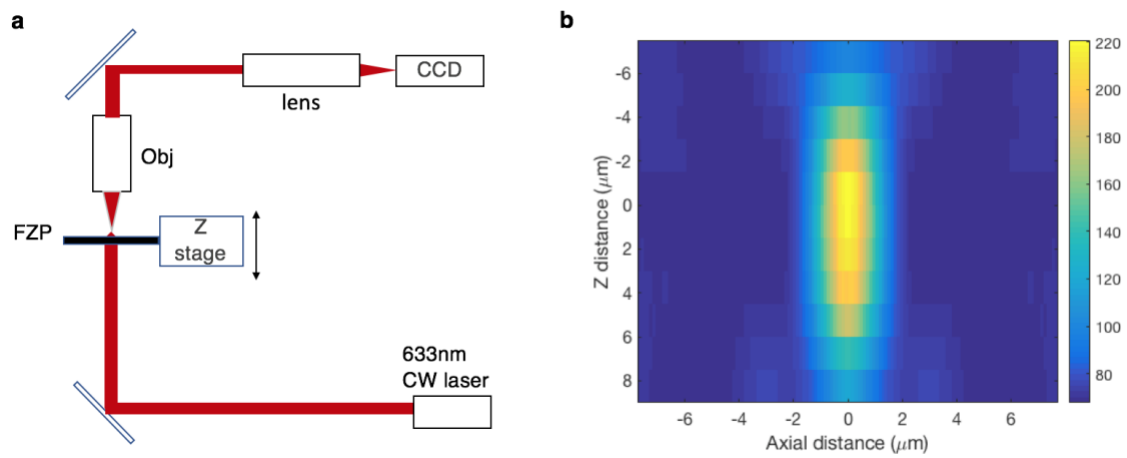## A4.3 Characterization of optical metasurfaces (Fresnel Zone Plate)

Figure A4.4 FZP characterization setup and intensity distribution at the focal plane. (**A**) The FZP focal plane characterization setup. (**B**) The axial-vertical intensity plot near the focal plane.